THE UNIVERSITY OF LEEDS

THE SUPRAMOLECULAR STRUCTURE OF SURFACTANT FORMULATIONS

by

MARIAM HUSSAIN

A thesis submitted in fulfillment for the

degree of Doctor of Philosophy

in the

SCHOOL OF CHEMICAL AND PROCESS ENGINEERING

May 2020

Declaration of Authorship

I, MARIAM HUSSAIN, declare that this thesis titled, 'THE SUPRAMOLECULAR STRUCTURE OF SURFACTANT FORMULATIONS' and the work presented in it are my own. I confirm that:

- This work was done wholly or mainly while in candidature for a research degree at this University.
- Where any part of this thesis has previously been submitted for a degree or any other qualification at this University or any other institution, this has been clearly stated.
- Where the thesis is based on work done by myself jointly with others, I have made clear exactly what was done by others and what I have contributed myself.
- The candidate confirms that the work submitted is his own and that appropriate credit has been given where reference has been made to the work of others.
- This copy has been supplied on the understanding that it is copyright material and that no quotation from the thesis may be published without proper acknowledgement.
- The right of Mariam Hussain to be identified as Author of this work has been asserted by her in accordance with the Copyright, Designs and Patents Act 1988.

Signed: _____

Date: _____

"No work so great, but what admits decay.
No act so glorious, but must fade away,
Old things must yield to New, Common to Strange,
Perpetual motion brings perpetual change."

James Miller, 1731

Abstract

Powdered detergent products are formulated with various components, such as aqueous polymers and surfactant solutions, to which powdered components such as salts and zeolites are added and these are mixed at a high shear rate for a few hours. The interactions between the surfactant and polymer directly influences the supramolecular structure (particularly the phase and colloidal structure) of the formulation. This in turn influences the final detergent powder structure, properties and performance. Therefore, a thorough understanding of the structural changes resulting from the addition of polymer to aqueous NaLAS dispersions, as well as the structural changes arising from shearing the formula is vital when considering cost effective formulation decisions, but the effect of both of these factors are poorly-explored. This PhD is designed to understand the influence of the addition of polycarboxylate polymer on the phase and colloidal structure of linear akylbenzene sulphonate (NaLAS) surfactant dispersions in aqueous conditions and saturated sodium sulphate solution conditions. For the aqueous system, a phase diagram was constructed using centrifugation and optical polarised microscopy. Following this, a more in-depth understanding of the phase behaviour was realised using Small Angle X-Ray scattering (SAXS), as well as the influence of polymer on the colloidal structures using ^{2}H nuclear magnetic resonance NMR. The combination of these studies led to the conclusion that the polymer behaves as a flocculant in the system, causing phase separation in the micellar regime. Additionally, a decrease in the bilayer spacing in the lamellar phase was observed due to the addition of the polymer compressing the bilayers. Also, the the osmotic effects resulting from the polymer addition caused multilamellar vesicle fusion, which then subsequently increased the average multilamellar vesicle size. This change in vesicle size was measured using ^{2}H (NMR).

Following this, the influence of the addition of the polymer on microstructure of NaLAS in saturated sodium sulphate solution were explored. Firstly, by constructing a phase diagram and then followed by pulsed-gradient simulated train echo (PGSTE) diffusion experiments to characterise the microgeometry of the system. How this microstructure changed with polymer concentration was also explored. A phase diagram of the system which was constructed using centrifugation, showed that the addition of the polymer increased the ratio of the lamellar phase to the isotropic phase until there was just a single lamellar phase remaining. Surface area to volume ratio, pore size and tortuosity measurements using NMR,

as well as SAXS experiments helped show that this change in ratio was not due to microgeometry changes. Hence, it was likely that the ratio change observed was a result of the polymer sterically stabilising the vesicles.

Finally, the structural changes over time resulting from the application of a high constant shear rate on a model formulation system were explored. Upon the application of high constant shear rates (above 1800 s^{-1}), an irreversible increase in the viscosity was observed. In-situ cryo-SEM experiments were carried out to conclude that in this system prior to the high shear mixing, kinetically stable vesicles were present due to the low bubble rise velocity resulting from the high viscosity of the system without the bubbles. The application of high shear rates for extended periods of time increased the Reynolds number of the system, which promoted bubble coalescence, and this consequently significantly increased the bubble rise velocity. This bubble rise velocity increase in time reduced the bubble fraction in the system, and hence the measured viscosity. This is because the high shear rates significantly increases the Reynolds number within the system to a turbulent regime, promoting the creaming of the bubbles to the surface and subsequently bubble breakdown. The addition of the polycarboxylate polymer prevented all the time dependent viscosity changes as inhibited the formation of kinetically stable bubbles in the system.

...

Acknowledgements

There are many people who have led me to where I am today, and for each and everyone of them I am so grateful. Firstly, and most importantly, I would like to thank my family - everything I am and everything I will ever be is down to you, always. Emily Guthrie and Amina Sattar: well you basically are family, aren't you? Andrew Bayly, my supervisor, who despite initially (probably) having a difficult time supervising me, put up with me and helped my writing skills develop from atrocious to, well, just about acceptable. You also pushed me to develop a level of independence that I have grown to admire about myself. I thank you Andrew for everything that you have done for me. Also Mamatha Nagaraj, who supported me when I needed it the most, for this I will be forever grateful. You always supported my decisions and always wanted the best for me, you are a fantastic supervisor for all your students, someone everyone looks up to. Next I would like to thank Cliff Jones; you have been an exceptional mentor who inspired self-confidence in me. I also thank Olivier Cayre for his supervision.

I would like to thank Nina for being there for me for all these years - you are an absolute diamond. I also thank Nikita for his support and help over the years. Finally, I thank Wael for the continued support he has provided. I thank the whole Soft Matter Physics group for being a fantastic support group .

Also Dan Baker, well the saying goes, 'Jack of all trades, master of none.' However, with you, you are the Jack of all trades and master of all, too. Thanks for all your help (particularly with NMR)!

Ben Douglas and Susanne Patel; you must have spent many hours of your lives training me on just about every piece of equipment possible in the analytical and colloid labs, as well as dealing with multiple enquiries from me over the years, yet you have always been very helpful - thank you!

Finally Eric Robles, Hossam Tantawy and everyone else at P&G Newcastle Innovation Centre; your support was an absolute delight, I am so glad that I have had the opportunity to work with you.

I thank P&G and EPSRC for funding my CASE award PhD.

Contents

List of Figures

List of Tables

Nomenclature

χ	Quadrupolar splitting constant, dimensionless
Δ	NMR observation time, ms
δ	NMR pluse duration, ms
$\Delta(phase)$	Phase difference in lanbda
$\Delta\nu_Q$	Quadrupolar splitting, Hz
$\Delta\nu_{1/2}$	Half width at half maximum, Hz
$\dot{\gamma}$	Shear rate, s^{-1}
η	Viscosity, Pa.s
ν_0	Larmor frequency, Hz
σ	Gyromagnetic ratio, Hz/T
σ	Shear stress, Pa
τ	Tortuosity, dimensionless
τ_c	Correlation time, s
θ_{CD}	Angle between Carbon and Hydrogen atom in a molecule
θ_{HH}	Angle between two Hydrogen atoms in a molecule
θ_{ml}	angle between the main and laboratory axis
a_s	Optimum head group cross-sectional area. $\mathring{A}^2$
ADC_0	Time-dependent diffusion coefficient, mm^2/s

B_0 Magnetic field strength, T

CMC Critical micelle concentration, mol.dm^{-3}

CPP Critical packing parameter,dimensionless

D Diffusion coefficient, mm^2/s

d_{Bragg} Bragg spacing, $\mathring{A}$

$I(0)$ SAXS radiation intensity at a scatter angle of zero, absolute units

$I(q)$ SAXS radiation intensity detected by detector, absolute units

K Consistency index, dimensionless

l_c Hydrophobic tail length, $\mathring{A}$

M Magnetization, A/m

MLV Multilamellar vesicle

n Flow index, dimensionless

q Momentum transfer, nm−1

q_{peak} Bragg peak angle, degrees

R Multilamellar vesicle (MLV) radius

R_G Radius of gyration, $\mathring{A}$

r_{HH} Vector between two hydrogen atoms, dimensionless

S NMR signal intensity, absolute units

S Orientational order parameter, dimensionless

s Surface area, m^2

T_1 Longitudinal relaxation time, ms

T_2 Transverse relaxation time, ms

v Volume, m^3

v_s Hydrophobic tail volume, $\mathring{A}^3$

H Hamiltonian, J

Chapter 1

Introduction

1.1 Overview

This project is a collaboration between The University of Leeds and Procter and Gamble. The project is designed to understand the phase and colloidal structure of surfactant formulations, with an emphasis on the influence of the addition of polymer and processing on the structure. This understanding can help influence business decisions with respect to formulation decisions, as well as decisions on the processing conditions of powdered detergent manufacture. Various studies, beginning with the work from Sein et al (3), and more recently the work by Stewart et al (5), have described the phase behaviour of the surfactant NaLAS in water and how it changes with the addition of various salts. This surfactant is the main component in the formulation of detergent powders, and the studies of the the phase behaviours by Sein and Stewart have been highly influential in business decisions for the detergent powder manufacture process.

The formulation of detergent powders follows a multi-stage process. Firstly, the liquid components composing surfactants and polymers are added in a large scale mixer where they are mixed for extended periods of times at high rates. Then, this mixture is pumped to the top of a spray drying tower, where the mixture is atomised into droplets and dried into a powder. The performance of the powder depends upon the structure of the powder and the structure of the formulation which depends on how the components interact with one another. This structure change as both as a result of composition changes, as well as processing. So,

this PhD will focus on understanding the structural changes resulting from the addition of polymer, and as a result of processing.

1.2 Context of the thesis

This thesis will focus on the surfactant Linear alkylbenzene sulphonate (NaLAS), which is the most widely used surfactant in the world, mainly used in detergent formulation. The structures of detergent formulas directly influence the physical properties of the final detergent product, so it is important to understand structure and how various components interact, particularly with the surfactant, in order to understand the impact on this on the performance of the detergent product. The phase behaviour of NaLAS is well studied, most recently in a thesis published by James Stewart, who probed the phase behaviour of NaLAS in water, as well as the influence of the addition of salt on this. The influence of polymer on the phase and colloidal structure of NaLAS in water is still unknown, and this thesis will hence explore this for systems formulated with and without salt. Furthermore, there are limited studies on the influence of shear on the structure of NaLAS formulations. Stewart, in his thesis carried out some shear sweeps, however he did not explore the viscosity changes over time at constant shear rates. This is important because in powdered detergent productions, the formulations are mixed at high constant shear rates for extended periods of time, often for hours. So understanding the changes that occur over time, as well as the structural changes causing these can help influence formulation decisions. This thesis will explore both the influence of the addition of polycarboxylate polymers and processing in great detail which has not previously been explored.

Additionally, despite the phase behaviour of NaLAS in water and the ternary NaLAS-water-salt systems has been explored in detail, however, the interaction of polymers with NaLAS has, to our knowledge, not been explored - this work will explore the phase and colloidal structure of NaLAS in water and how the addition of polymer influences this in order to obtain an understanding of the interactions. Futhermore, the colloidal structure of NaLAS dispersions have not been characterised with respect to their sizes as none of the conventional sizing techniques such SAXS, DLS and laser scattering are unsuitable because the systems cannot be diluted making laser scattering unsuitable. Multiple scattering makes DLS unsuitable and the high ionic strengths makes SAXS suitable. This work will adapt

an existing nuclear magnetic resonance (NMR) method to size the colloidal structures of this system for the first time. Moreover, the influence of polymer on the surfactant structures in high ionic strengths will be explored.

1.3 Aims and Objectives

There is a list of systematic objectives in this thesis to eludicate the structure of an industrial surfactant-polymer system. These include:

- To understand the interaction of polycarboxylate polymer with NaLAS surfactant, by understanding the phase behaviour changes resulting from polymer addition. Therefore, phase diagrams will be constructed using various techniques such as SAXS and centrifugation. Furthermore, the influence of polymer on the surfactant colloidal structure will also be probed, determining suitable existing techniques achieve this aim. Alternatively, suitable techniques will be developed.
- Building upon this, the influence of the addition of polymer on surfactant structures in saturated sodium sulphate solution will be probed. This is important because in industrial detergent formulations, the salt concentrations are high.
- Finally, a model surfactant-sodium sulphate system which shows interesting behaviour during processing during the powdered detergent manufacture process will be analysed; this will be explored using rheology, and complimentary in-situ structural analysis techniques such as cryo-SEM.

1.4 Structure of the thesis

This thesis will begin with a comprehensive literature review of surfactant self-assembly, describing the phase and structure of aqueous surfactant dispersions in general, in addition to overviewing the existing literature of NaLAS and anionic surfactants used in detergent formulations. Building upon this, it will describe some of the existing literature on the influence of the addition of polymer on the phase and colloidal structure of surfactant formulations. Then, a methods and materials chapter will overline the main

techniques used in this thesis, including: NMR, rheology, cryo-SEM, optical microscopy, centrifugation and SAXS. The chapter will consider the theory behind the techniques and their significance for the understanding of the structure of surfactant formulations, as well as an overview of the equipment used in subsequent results chapters.

The first results chapter will describe the influence of polycarboxylate polymers on the phase and colloidal behaviour of NaLAS in water. NaLAS-water-polymer phase diagrams will be constructed using microscopy and centrifugation, and NMR will be used to determine the influence of the addition of polymer on the surfactant colloidal structure. These observed changes in phase and colloidal structure will be related to the the surfactant-polymer interactions.

The following results chapter takes a model NaLAS-sodium sulphate-water system and probes the structural changes that cause viscosity changes as this model system is mixed at high shear rates. SAXS and cryo-SEM are the main techniques used to relate the changes in viscosity to the changes in structure.

In the final results chapter, NMR will be used to analyse the diffusion of water within the pores in a matrix of a surfactant-polymer-sodium sulphate solution model system. These diffusion experiments will be carried out to determine the sizes of the pores. Changes in the pore size as a function of polymer concentration will be determined in order to gain some understanding of the interaction between the polycarboxylate polymer and the NaLAS surfactant in high ionic strength conditions.

Throughout this thesis, unless stated, the experiments will be carried out at 50°C because industrially, the surfactant systems will not be processed at a temperature below 45°C. This is because the salt will form a hydrate at the lower temperatures which is undesirable in the detergent manufacture process.

Chapter 2

Literature review

2.1 Surfactant phase and colloidal behaviour, and the influence of polymer

Surfactants are amphiphilic molecules, generally comprising of a lyophobic (solvent-hating) region and a lyophilic (solvent-loving) region. The lyophobic region is described as hydrophobic when the molecule is in an aqueous environment and the lyophilic region is described as the hydrophilic region. The opposing hydrophobic and hydrophilic forces allows two main phenomena to arise: aggregation and adsorption.

Adsorption describes the process in which the surfactant molecules migrates to the air-water, solid-water or liquid-liquid interface to minimise the contact between the hydrophobic region and the water, and hence reducing the free energy of the system (14).

Aggregation results when the interface has been saturated with the surfactant molecules and the free energy of the system needs to be reduced. This occurs by the self-assembly of the surfactant molecules into various structures to ensure that

TABLE 2.1: The critical packing parameter corresponding to different aggregates formed (11).

Aggregate formed	**Critical packing parameter**
Cylindrical micelles	1/3 - 1/2
Reverse micelles	>1
Planar bilayers	1
Vesicles and flexible bilayers	1/2 - 1

the hydrophilic head groups orient towards the aqueous phase. The shape and size of the structures formed vary depending on multiple parameters, including: surfactant concentration, surfactant temperature, hydrophobic chain volume and hydrophobic head group cross-sectional area. Israelchivilli (15) presented a model known as the molecular packing parameter model, which can predict the structure of the aggregates formed (examples are displayed in Table 2.1).

This critical packing parameter is defined as:

$$cpp = \frac{v_s}{a_s l_c}, \tag{2.1}$$

where v_s is the hydrophobic tail volume, a_s is the optimum head group cross-sectional area, l_c is the hydrophobic tail length.

The optimal area of the head group can be influenced by the pH, electrolyte concentration and the presence of any additives, such as co-surfactants and alcohol.

Surfactants are usually characterised in reference to their head group type. The main groups of surfactants are as follows:

- Anionic surfactants: the head group is negatively charged; most anionic surfactants have one or more sulphate or sulphonate groups. These are the most commonly used group of surfactants and contribute to 60 % of the

surfactants used worldwide. They are incompatible with cationic surfactants, so they an anionic surfactant usually connot be formulated with a cationic surfactant.

- Cationic surfactants: these have a positively charged head group. They are frequently used in fabric softeners as it fulfills one of the main utilities of fabric softeners: to reduce static cling by neutralising the negatively charged fabric fibres. The most common types of cationic surfactants are quaternary ammonium compounds and amine-based compounds.

- Non-ionic surfactants: these consist of either polyether or polyhydroxyl groups in the polar head of the surfactant, however, the vast majority are polyether compounds consing of 5 to 10 repeating oxyethylene units. They are most commonly used to stabilise water-oil emulsions (16).

- Zwitterionic surfactants: these contain two oppositely charged groups. The most common types of zwitterion surfactants have the N-alkyl derivatives of amino acids and imidazoline. This group of surfactants tends to have very suitable dermatological properties, therefore they are frequently used in cosmetic products and function effectively in electrolyte formulations. As these surfactants are usually very expensive, they are less commonly used compared to anionic, cationic or non-ionic surfactants (16).

2.1.1 Surfactant self assembly at low concentrations

Initially, when a surfactant is added to a system such as a basic air/water system, the surfactant concentration is very low and increasing the concentration of surfactant has no noticeable effect on the surface tension of the water as the surfactant is present as monomers in the bulk system. Further, as the concentration increases, there is a proportional relationship between the surfactant concentration and surface tension. As the surfactant concentration is increased, the surface

tension also increases. At the surface, there are attractive cohesive forces between water molecules and the presence of surfactants reduce these attractive forces. Hence, surface tension reduces as the amphiphile arranges itself on the surface as such that the hydrophilic end of the tail interacts with the water phase and the hydrophobic end interact with the phase surrounding the water surface in order to minimize the free energy of the system. The ability of surfactants to accumulate at interfaces is a key property of surfactants. Surfactants with a higher tendency to accumulate on a boundary are usually 'better' surfactants. However, one surfactant may accumulate very well at one interface, but poorly at the other interface, therefore careful consideration of the properties of surfactants is key when considering which surfactant is used for a particular application (4).

As the surfactant concentration is further increased, the surface is saturated with surfactant, so additional added surfactant begins to self-assemble into micelles, which are spherical aggregates where the hydrophobic tail faces the centre of the sphere to minimise disruption of the water structure and to minimise the free energy of the system. The surfactant concentration at which micelles begins to form is the critical micelle concentration. Spherical micelles tend to form initially, but as surfactant concentration continues to increase the spherical micelles tend to transition into globular and rod-like micelles. In water-oil systems where there are lower water concentrations compared, reverse micelles can form where the hydrophilic head faces the centre. As the concentration of surfactant increases, various different types of self-assembling structures can form (4).

The self assembly of surfactants in water can be described in terms of the free energy of the system. The Gibbs free energy of the system is the sum of the the interaction energy due to the surfactant tail, the interaction energy due to the aggregate core-water interactions and the interaction energy due to the repulsion between the head groups. The first interaction due to the surfactant tail arises from the transfer of the surfactant tail from its unfavorable contact with water to

the favorable hydrocarbon-like environment of the aggregate core. This is a negative term and this free energy contribution depends on the surfactant tail but not on the aggregate shape or size. The second term interfacial term is a positive free energy contribution that accounts for the residual contact between the surfactant tails and water at the aggregate core-water interface. This is represented as the product of a contact free energy per unit area (or an interfacial free energy per unit area, self-Assembly or interfacial tension) and the surface area per molecule of the aggregate core (4). The third term due to the head groups is another positive free energy contribution that accounts for the repulsive interactions between the headgroups because they crowd at the aggregate surface. The repulsions may be due to steric interactions (for any type of headgroup) and also electrostatic interactions (dipole–dipole interactions for zwitterionic headgroups and ion–ion repulsions for ionic headgroups). Since the repulsions would increase if the headgroups come close to one another, Tanford proposed an expression for this free energy contribution with an inverse dependence on the surface area per molecule of the aggregate core.

The formation of micelles in water results from the 'hydrophobic effect (17)'; the dissolution of the micelle into water is resisted due to the strong repulsive forces between the water molecules and the hydrocarbon chains of surfactants, so this hydrophobic effect results from two contributions. Firstly, there is a negative entropy resulting from water coming to close contact with the non-polar hydrocarbon chain of the surfactant molecule. The surfactant molecules have fewer possible conformations in water in comparison to free water, so an entropy decrease results. Also, the water close to the surfactant forms stronger hydrogen bonds, which results in a further decrease in entropy. The second contribution factor to the hydrophobic effect results from the high energy necessary to form a cavity within the water to allow the surfactant to fit into. This results from

strong cohesive forces arising from the small size of water molecules in comparison to the surfactant molecules. Also, the hydrogen bond density in water is very high, which also makes the disruption of these to form the cavities energy intensive. From this, one can conclude that the magnitude of the hydrophobic effect is proportional to the cavity surface area required for the surfactant to fit into. This hydrophobic effect is fundamental in understanding the self-assembly of surfactants at all concentrations (17).

The micelles formed resulting from ionic surfactants differ from the micelles formed from non-ionic surfactants. Micelles formed resulting from ionic surfactants consist of the following (also described further in Figure 2.1) (18):

- A hydrophobic core: the centre of the micelle consisting of the hydrocarbon chains;
- A Stern layer: this surrounds the core consisting of the hydrophilic head groups;
- A Gouy-Chapman electrical double layer which surrounds the core; this is a diffuse layer which consists of counter-ions that neutralise the ions in the Stern layer.

Micelles formed by non-ionic surfactants have the following composition:

- A Hydrophobic core; the centre of the micelle consisting of the hydrocarbon chains;
- A Palisade layer; which consists of the surfactant tails and polar molecules (18);

At higher surfactant concentrations, lyotropic liquid crystal structure can form. Micelles begin to transition into hexagonal arrays, a phase known as the hexagonal

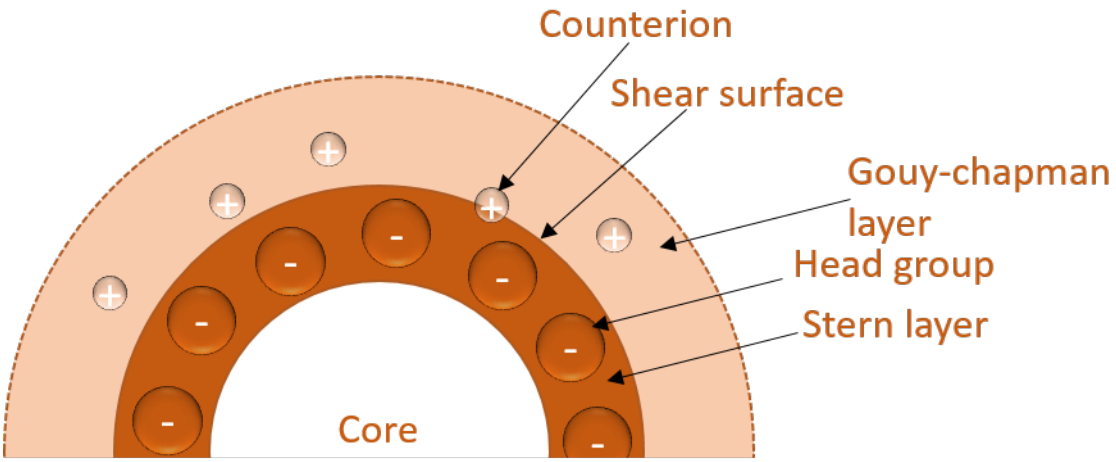

FIGURE 2.1: Labelled structure of the components of a micelle

(middle) phase where surfactants form groups of rod-like clusters and are packed hexagonally. There are 2 types of hexagonal phases which can form; the normal hexagonal phase (H1) and the reverse hexagonal phase (H2). The H1 phase consists of normal micelles arranged in a cylindrical fashion, whereas the H2 phase consists of reverse micelles packed in a hexagonal manner. The H1 has a positive surface curvature whereas the H2 phase has a negative surface curvature (19).

As the concentration of surfactant further increases, a transition to a cubic structure occurs. There are three types of cubic structures surfactants can assemble into. Firstly, there is the viscous normal isotropic phase (V1) and viscous reverse isotropic phase (V2). The V1 has a positive surface curvature but the V2 has a negative surface curvature. As the concentration is once again increased, the structure transitions into a neat, lamellar (Lα) phase where the surfactant molecules are arranged in layers,and the amphiphilic nature of surfactants results in a bilayer arrangement where two amphiphiles face opposite each other, and the hydrophobic tails face toward each other, as shown in Figure 3.5 (19).

Although the neat phase has a high surfactant concentration, it has a relatively low viscosity due to the fact that they bilayers can easily slide over each

other on the application of shear. The layers slide over each other easily and maintain their periodic arrangement which results in the fluid nature of the structure. The introduction of a methyl group in the hydrocarbon chain often reduces the critical micelle concentration, so can the introduction of double bonds into the structure along with the introduction of a polar segment (20).

The self-assembling structure depends on the critical packing parameter and the interfacial surface curvature as shown in Figure 3.5. The head group of the amphiphile that faces the water interface and the tail on the other side of the surface interface determine the curvature, and the surface curvature can be used to define what self-assembling structure is present (1).

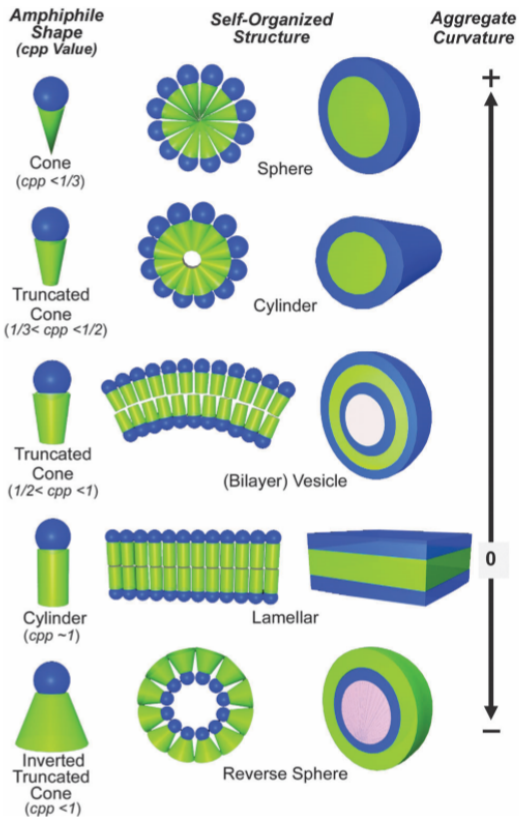

FIGURE 2.2: Figure shpwing the shapes of the self-assembling surfactant structures and the critical-packing parameters at which they form (1).

There are various factors that help determine which liquid crystal phase can form. These include:

- The strength of repulsion between head groups arranged at the water-surfactant interface. This repulsive force is directly influenced by how strongly the head groups are hydrated, the charge of adjacent surfactant molecules as well as alkyl chain steric requirements (21).
- The degree of conformation of the alkyl chains, which is directly influenced by the chain length and saturation extent (21).
- Presence of an electrolyte salt, which can have a significant effect of the ionic strength of the solution and the repulsive forces between head groups (21).

The hydrophobic tail generally consists of fatty acids and traditionally, ethoxylates and sorbitan esters of fatty acids have been used. The selected hydrocarbon chain has significant impacts on the surfactant properties. For example the presence of double bonds can influence critical micelle concentration as the bulkiness of the surfactants increases, meaning the packing of the chains is more difficult and increases the hydrophobicity of the surfactant. The hydrophobic chain length also significantly affects the critical micelle concentration. Generally, as the hydrocarbon chain length increases, the CMC decreases. In the presence of a salt, this change in CMC with increasing chain length is more profound. Also the Krafft point (the minimum temperature at which micelles can form) is also highly dependent upon chain length (22).

2.1.2 Liquid crystals

Liquid crystals are a phase of matter which has properties between those of conventional liquids and solid crystals. Like solids, they have orientational order and possess symmetrical properties but, like liquids they can flow (23).

At high surfactant concentrations, typically at concentrations greater than 100 times the CMC, anisotropic liquid crystal structures form. This is because

initially, at lower surfactant concentrations, the surfactant molecules aggregate to form micelles and at higher concentrations these aggregate to form larger 'ordered' solutions (24).

In 'ordered' solutions the size of the head group, number of alkyl chains and polarity of the solvent are important and packing constraints must therefore be considered. Interactions between micellar surfaces are repulsive (from electrostatic or hydration forces), so that as the number of aggregates increases the micelles get closer to one another, the only way to maximise separation is to change the aggregate shape and size(25).

The addition of more surfactant in a micellar solution will result in a movement to a shape with a higher packing limit and therefore lower aggregate curvature. It should be noted that as the polar head group size increases the curvature also increases so liquid crystal formation depends on the type of micelle at the lowest concentration.

There are many different lyotropic liquid crystal mesophases that exist. Of these, there are six phases with well characterised structures. These are lamellar, hexagonal, cubic, gel, nematic and intermediate phases. Each structure can exist in oil continuous or water continuous media in either a 'normal' or 'reverse' configuration often denoted by subscripts 1 and 2 respectively. Lyotropic liquid crystal phases are usually distinctly different topologically from thermotropic phases and examples include: the cubic, hexagonal, lamellar and intermediate phases (26).

The most important technique to identify the mesophase type is polarising optical microscopy. All the phases are birefringent and display a unique texture when viewed under crossed polarisers, while cubic phases have none. The cubic phases are isotropic and therefore appear black under crossed polarisers however, are very viscous. This technique is discussed further in Chapter 3 (23).

2.1.3 The Order Parameter

The simplest way to describe the anisotropy of a lyotropic system is using the order parameter, *S*. The order parameter describes a function of the angle between the molecular axis of a molecule and the average direction at which an ensemble of molecules face, this is shown schematically in Figure 2.3 (27). This is often referred to as the laboratory axis. In the case of surfactants, the order parameter is dictated by the flexible hydrophobic chains. The order parameter can be described for each individual segment of the chain, or more commonly as an average of the chain. In practice, multiple order parameters exist for the different vectors of the methylene groups. r_{HH} describes the vector between the two hydrogen atoms, and the S_{HH} order parameter characterises the ensemble average angle between the laboratory axis and r_{HH}. A final order parameter considers the surfactant dispersed in D_2O, and describes the ensemble average angle between the laboratory axis and the bond vector between the carbon atom of the chain and the deuterium atoms of the solvent. Equations 2.2 and 2.3 and show the relationship between the two order parameters and the angles between the corresponding vector and the laboratory axis (28).

$$S_{CD} = \frac{1}{2}(< 3cos^2\theta_{CD} > -1), \tag{2.2}$$

$$S_{HH} = \frac{1}{2}(< 3cos^2\theta_{HH} > -1). \tag{2.3}$$

Where S_{CD} is the average segmental order parameter between the deuterium in the water and the carbon in the methylene group, S_{HH} is the average segmental order parameter for the Hydrogen-Hydrogen atom interactions in the methylene groups. The segmental order parameter values can range from -0.5 to 1 (29). The determination of these segmental order parameters is highly useful in characterising the local conformational properties of the surfactant bilayers which can be useful in understanding the self-assembling structure of the surfactant in water. This is useful for the NaLAS-water system because the vesicles should display an

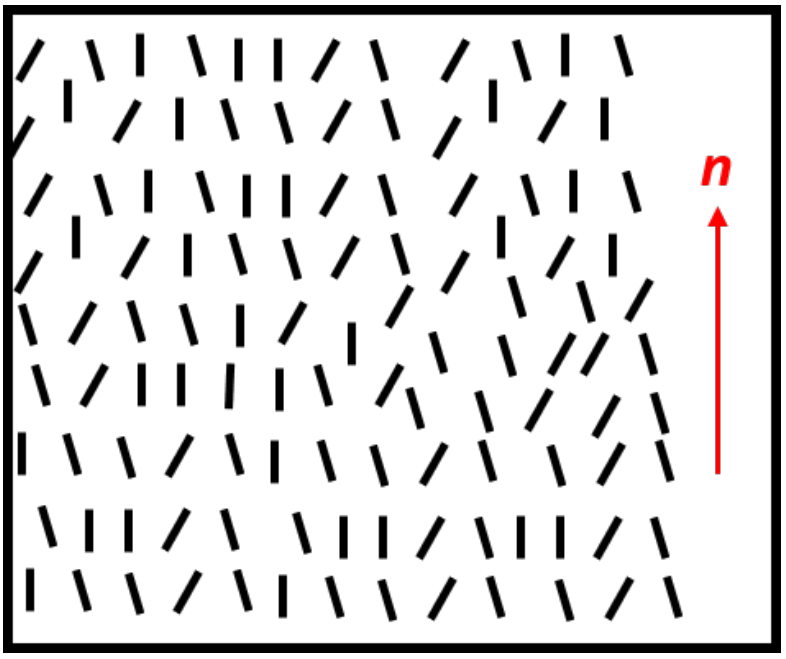

FIGURE 2.3: Schematic showing an ensemble of molecules with orientational order, where the order is parallel to the director, **n**.

average order parameter of zero. In the case of a perfect bilayer, the order parameter will also be zero, when the average angle between the director and the direction the molecules face is zero. However, in practice this is almost never zero due to bilayer undulations and these undulations result from the configurational entropy of the bilayer. Blayers are extremely fluid and dynamic and move as a response to environmental stimuli such as changes in temperature. So, changes in these properties results in changes in the order parameter.

An understanding of the segmental order parameter can prove useful in understanding the conformations of in lyotropic surfactant structures can be useful to determine molecular orientatation and motion within the surfactant chains of the supramolecular stuctures(27). Nuclear mangetic resonance (NMR) can be used to directly measure the orientational order parameters.

2.1.4 Lamellar, Lα phase

The lyotropic liquid crystal phase most commonly exhibited in surfactants is the Lamellar (Lα) phase, which is also known as the 'neat' phase. In this phase, the surfactant molecules assemble into ordered bilayers and these bilayers are extensive, continuing over at least 1 μm. These bilayers are separated by water. The lamellar phase is distinctive in the fact that it has characteristic rheological and optical properties (discussed further in section 4.2) (30). These bilayers have a fatty structure which means that when the mesophase experiences shear forces, the parallel bilayers can slide easily over each other. Therefore, the viscosity of lamellar structures is rather low (31). This phase can also be identified using small angle X-ray scattering. The physical properties of bilayers include low viscosity and high pourability which makes the structure very suitable for use in detergents.

Planar sheets are just one morphology form the Lα phase can exhibit. These layers can also fold into vesicles. Unilamellar vesicles form as a result of the bilayer trapping the aqueous phase, and multi-lamellar vesicles result from multiple concentric layers entrapping the aqueous phase. Vesicles have the applications in pharmaceuticals and in the detergency industry to encapsulate drugs, perfumes and enzymes. Furthermore, they have interesting applications in academia acting as models for cells and cell membranes. The use of unilamellar vesicles in drug delivery applications arises from their biocompatability; they can fuse with human cells and release their contents into cells. Research is being carried out to manipluate the structure of these vesicles to help increase bioavailability of the drugs contained within the vesicles (32). Controlling surface charge, and surface hydration has been shown to be critical in influencing the drug bioavailability. The structure of the vesicle needed depends directly upon the part of the body being targeted. For example, vesicles inhaled into the lungs need to not irritate the lungs, whereas vesicles that are swallowed need to be able to withhold the

alakaline conditions of the stomach (33). Vesicles have been successfully used as vectors for genetic transfections in the eyes (32). They have also been used to successfully encapsulate vaccines. Another revolutionary use of vesicles in medicine is their use in tumour treatment. They have been shown to passively target small tumours because they can circulate for longer time periods in the tumour cells compared to healthy cells. The vesicles for each different application require distinctly different compositions to result in the different sizes, surface charges and surface hydration needed for the application (34). These vesicles can also result from the aggregation of micelles resulting from the addition of various salts, this is explained later in this chapter.

2.1.5 Spontaneous formation of vesicles

Unilamellar and multilamellar vesicles are not thermodynamically stable structures, and usually require the input of energy to stimulate their formation. However, their formation has been reported multiple times in various systems including:

- Double-chain dialkyldimethylammonium surfactant in combination with counterions including bromide, chloride and hydroxide counterions;
- Vesicles formed from oppositely charged surfactants, known as catanionic vesicles;
- Vesicles formed in multi-component systems, such as anionic surfactant/ cosurfactant/ water/ non-ionic surfactant (35).

There are 2 approaches which can be used to model self-assembly of vesicles: the molecular approach and the more common curvature-elasticity approach. The curvature-elasticity approach models the surfactant bilayer of a vesicle as a continuous bilayer. The bilayer is a characteristic of the spontaneous curvature

and elastic bending modulus. These 2 characteristics both contribute to the self-assembly of surfactants and this approach can be used to describe the spontaneous formation of vesicles (36). However, this approach is limited as it does not accurately model very small vesicles as the surface area is very large hence the free energy of the membrane and membrane curvature is high. The two characteristics are phenomenological parameters, so the model is limited in its ability to quantitively model a system. An increase in the elasticity of the membrane can stimulate the formation of vesicles, and various conditions can result on a low membrane elasticity, such as the addition of a long chain alcohol.

The molecular approach was first proposed by Israelachvili et al (15), who developed the geometric packing arrangement shown in Equation 2.1, allowing the prediction of the shape of packing parameter as the function of the molecular volume, head group area and hydrocarbon chain length. The packing parameter required to form vesicles is 0.5-1. Single chain surfactants usually are unable to spontaneously assemble into vesicular structures when alone in solution as the packing parameter is usually around 1/3. This packing parameter is usually higher in double chain surfactant mixtures, often reaching 0.5.

As single chain surfactants are usually unable to spontaneously self-assemble into unilamellar vesicles alone, they require the presence of a co-surfactant so the system can behave like a pseudo double chain surfactant system, or the addition of a cationic surfactant which also allows the effective packing parameter to increase as the anionic and cationic surfactants can associate as a result of hydrogen bonding (37).

Surfactant counterions can promote the formation of vesicles, this is because the oppositely charged ion can screen the charged hydrophilic head of the surfactant, decreasing the effective headgroup area, a, hence increasing the effective packing parameter of the surfactant, promoting the self-assembly of the surfactant

into vesicular structures. The ionic strength of the solution in which the surfactant is dispersed within is increased, and this results in an increase in attractive forces between the surfactant head groups and dehydrates the head groups (38).

2.2 Structure of NaLAS

Commercial linear alkylbenzene sulphonic acid (HLAS) is generally composed of anumber of different alkyl chain lengths and positional isomers (the benzene ring is substituted on any carbon other than the terminal carbons, see Figure 2.4). It is manufactured using the Hydrogen Fluoride (HF) process, where n-Paraffins are broken down into n-mono-olefins and the n-mono-olefins are reacted with benzene in the presence of a HF catalyst to produce a linear alkylbenzene (LAB) and subsequently the LAB is sulphonated to leave HLAS. HLAS is neutralised with NaOH to give sodium linear alkylbenzene sulphonate (NaLAS). It can be netralised to give LAS which is associatied with a different cation, for example HLAS neutralised with KOH will give KLAS.

2.3 Phase behaviour of LAS-water systems

2.3.1 Phase behaviour of LAS-water systems

Many studies have been carried out to analyse the phase behaviour in detail at a variety of LAS and water concentrations, which will be discussed in detail in this section.

The understanding of this phase behaviour is critical in the formualation of detergent products. The main surfactant that comprises powdered detergent products is NaLAS(39). These detergent products are manufactured by spray

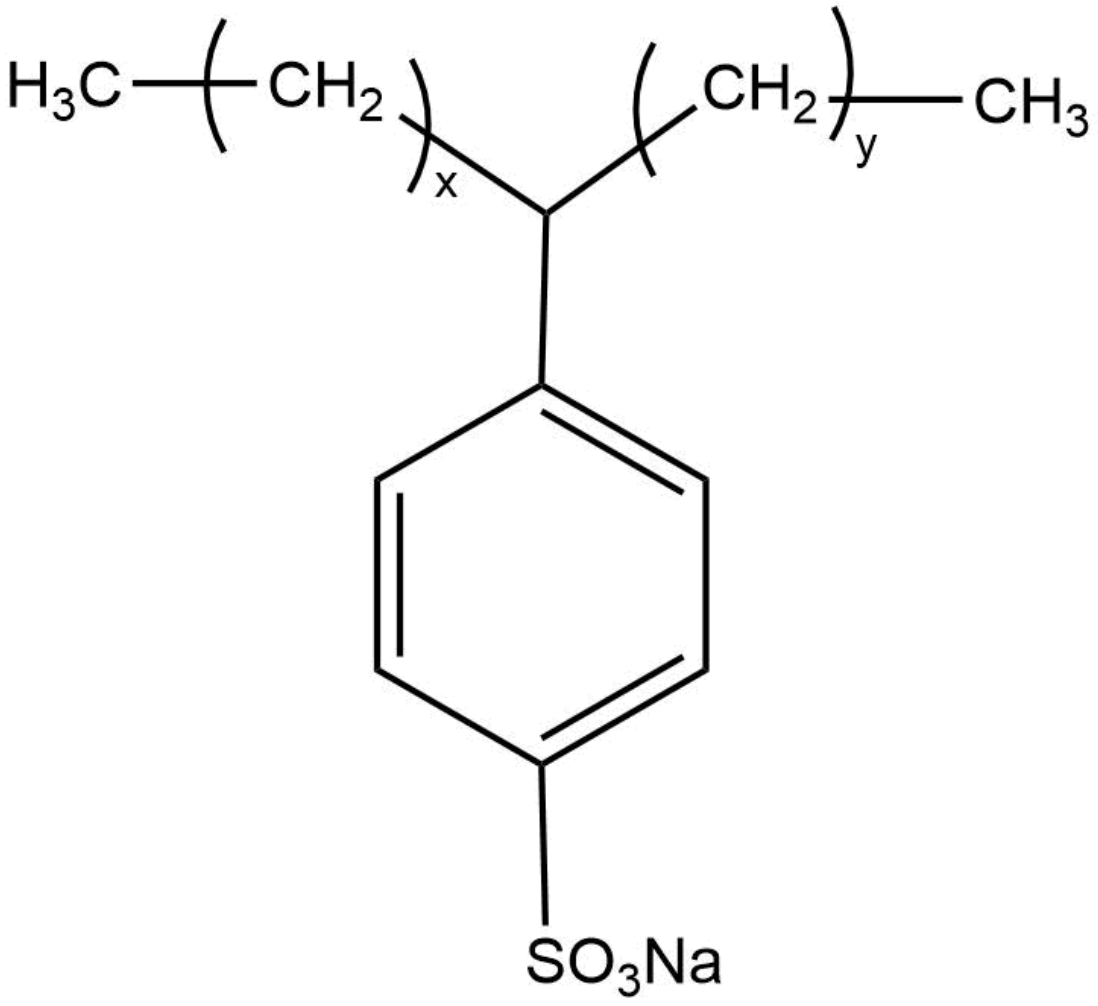

FIGURE 2.4: Structure of the commercially available NaLAS surfactant

drying NaLAS slurry formulations (these slurries also contain other components such as salts, polymers and silicates). The structure of the slurry formulation from which washing and hence the structure of the spray dried particles influence the storage properties, dissolution characteristics and how effectively the product cleans (39).

The structure of the slurry and consequently the spray dried particles depends highly upon the concentrations of ingredients within the slurry. This shows the significance of understanding the phase behaviour of slurries at various concentrations of LAS and water.

Various analytical techniques including light polarising optical microscopy,

differential scanning calorimetry, nuclear magnetic resonance and small angle X-ray diffraction have been used to analyse physical properties of the system and determine phase behaviour. The first study on the phase behaviour of LAS in water was carried out by Sein et al., (3) who explored the phase behaviour of LAS associated with a variety of counterions, namely: Li^+, Ca^2+, Cs^+, Na^+ and H^+ in water. It was observed that LAS associated with all counterions exhibits large areas of lamellar phases. NaLAS (the counterion of interest in this thesis) was shown to exhibit a micellar phase behaviour up to 24 wt%, at which point a phase transition to a coexisting region of micellar-lamellar phase area was observed. The next phase transition was observed at 64 wt% NaLAS where the 2 phase region transformed into a single phase lamellar region. The final phase transition was observed at 82 wt% NaLAS in water where a final 2 phase region of the coexisting micellar/lamellar phase area was observed. These phase transitions were determined by cross-polarised microscopy. These transition points refer to a temperature at 25°C, and there were variations when the temperature was changed. Sein et a; published the first data presenting the SAXS d-spacings for the lamellar phases of NaLAS in water. They observed a decrease in d-spacing as a function of NaLAS concentration in water from approximately 5.8 nm at 30 wt% NaLAS in water to 3.5nm at 90 wt% NaLAS in water. Sein et al proposed that this decrease in d-spacing was a result of dehydration of the NaLAS head groups as the concentration was increased.

The type of counterion that LAS is associated with has a profound influence of the phase behaviour; of all systems studied, only one showed a distinct hexagonal phase, the concentration at which phase transitions occurred was highly influenced by counterion type as the number of water molecules per molecule of amphiphile necessary to induce the lamellar phase is highly counterion dependent.

11 years later, Richards et al., (2) published a more comprehensive phase

behaviour study on NaLAS. One of the marked difference between the phase diagram published by Sein et al., (3) and Richards et al., (2) was that Richards et al observed that although at ambient temperatures a single lamellar phase is observed, as the temperature is increased, there is a wide region in which multiple Bragg peaks are observed, showing that infact there are 2 lamellar phases present. The 2 lamellar phases can be characterised in terms of their different d-spacings.

Following this, Stewart et al., (40) published another NaLAS-water phase diagram, but remarkably, he observed not 2 lamellar phases at high temeperatures, but many lamellar phases. This is a remarkable result as it shows that the system doesn't obey Gibbs phase rule, also a strange result because although both Stewart and Richards were characterising NaLAS, Stewart et al only observed 2 lamellar phases, whereas Richards et al observed multiple phases. The possible reason behind this difference proposed by Stuart was that neither the system observed by Stuart nor the system observed by Richards was isomerically pure; there were multiple positional isomers and also the chain lengths varied too for both systems. However, the isomer compositions of the samples analysed in both studies were not the same, so as the different isomers may behave as different components, both studies were inherently looking at different systems. Both Richards (2) and Stewart (40) used crossed polarised microscopy for phase identification (the textures observed can be used to characterise the microsctructure), SAXS to observe the number of SAXS phases present and to characterise their Bragg spacing - how it changes with temperature and concentration. ^{2}H NMR was also used to confirm the phases present and finally DSC to determine transition temperatures.

Ockelford et al., (41) published a study which observed an equilibrium between two lamellar phases. This upper-consolute region (the region in which 2 lamellar phases co-exist) between about 25 and 68 wt% NaLAS is characterised by an upper critical temperature of 39°C. The upper critical temperature is the maximum temperature at which the 2 lamellar phases can exist. The 2 co-existing

lamellar phases were characterised by ^2H NMR as when there were 2 co-existing lamellar phases, they could be described by the presence of 2 pairs of quadrupolar splitting in the spectra. The 2-phase lamellar region can be described by long-range repulsive electrostatic forces, along with hydration repulsion when there is a relatively low concentration of free water.

There are attractive forces between bilayers arising from the counterion binding mechanism where the concentration of counterions changes as a function of surfactant concentration and temperature hence there are correlations between ion positions on opposing layers give rise to attractive forces between bilayers which changes as a function of temperature and surfactant concentration.

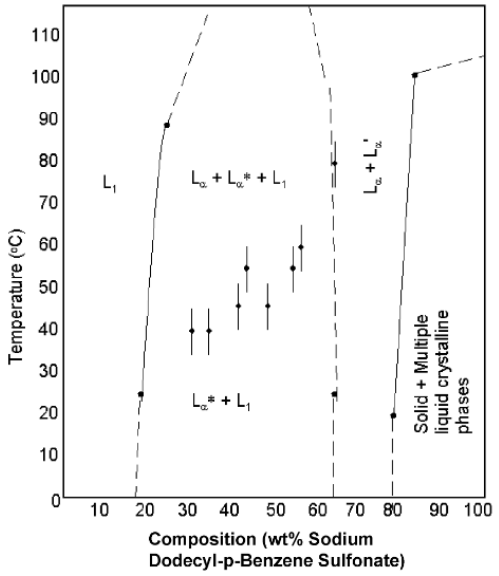

FIGURE 2.5: Phase diagram of NaLAS in water as studied by Richards et al (2).

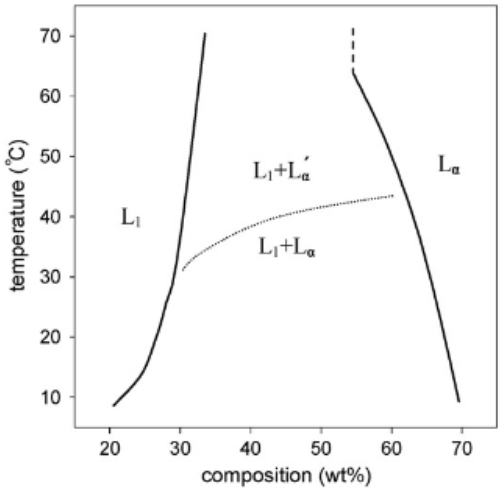

FIGURE 2.6: Phase diagram of NaLAS in water as studied by Stewart et al (3).

This interaction is perhaps responsible for the existance of an upper-critical loop because the free counterion concentration increases with temeperature. The counterion mechanism is proposed in order to justify the absence of a 2-phase region in the HLAS-H_2O system. This counterion mechanism has also been observed in a didodecyl-dimethylammonium bromide (DDABr)/water system (42), where a 2-phase region exists in the presence of the bromine ions, but not when the bromine ions are replaced by iodine or chlorine ions. This is because as previously stated, the 2 co-existing phases are in equilibrium, so the chemical potential of water in both phases must be equal. In this case, the 2 lamellar phases have a different bilayer thickness which can only occur in the presence of 2 repulsive forces over different decay lengths compete with an attractive force (42).

2.4 The formation of the lamellar phase

NaLAS is formed upon the neutralisation of HLAS with NaOH and although HLAS is an isotropic surfactant, NaLAS can form lyotropic liquid crystal phases in solution, perhaps the most important of these phases is the lamellar phase.

This phase results from the diffusion of water over the bulk HLAS surfactant. This diffusion can be described by Fick's law (43):

$$J_{AZ} = \frac{-D_{AB}}{kT} c_A \frac{d\mu_A}{dz}, \tag{2.4}$$

where D_{AB} is the diffusion coefficient, k and T are the Boltzmann constant and temperature respectively, c_A is the concentration of species A, J_{AZ} is the flux of substance A in the z direction and μ_A is the chemical potential of substance A.

Where the bulk surfactant is an isotropic liquid as in linear alkylbenzene sulphonic acid (HLAS) there will be an enthalpy driven processes (-ΔH), because the water will be able to hydrate the surfactant head groups and the counterion, which also contributes to the lamellar formation. If NaOH is present in the system, as is the case in an acid/base neutralisation, which is important in understanding the behaviour of the linear alkyl benzene sulphonate system, this will also be dragged into the bulk as the neutralisation has a favourable enthalpy, and the Na+ and its hydration shell will follow to meet the electro-neutrality requirement. However, where there are the requisite water molecules for the formation of the mesophase this process is rapidly overtaken (40). As the water diffuses into the bulk solution there are sufficient water molecules to satisfy the surfactants hydration requirement and (probably) to allow the counterion to dissociate. This induces the formation of a liquid crystalline arrangement, which in turn allows the water to diffuse more rapidly into the bulk solution along the inter lamellae (or other) channels. Equally other liquid crystal structures will open these channels. As more water penetrates the bilayers will swell allowing further penetration. This will include the hydroxide groups and its ion (Na+), again in the case of neutralisation.

Where the surfactant is a crystalline solid, in addition to the enthalpy of hydration, there will also be a thermodynamic contribution from the dissolution of the crystal. The increased configurational freedom will lead an increase in the

entropy of the system which is of course favourable. On the other hand there will be an unfavourable enthalpic requirement associated with the break-up of the lattice (40).

The formation of the lamellar phase can be described by the Gibbs equation:

$$\Delta G = \Delta H - T\Delta S, \tag{2.5}$$

where G is the Gibbs free energy, H is the enthalpy, T is the temperature and S is the entropy of the system. A process will occur spontaneously as long as the change in Gibbs free energy of the system as a result of the process decreases. As previously stated, the addition of an amphiphile in water is energetically unfavourable when considering the non-polar tail as it increases entropy and hence decreases the Gibbs free energy. Therefore, there is a rearrangement of the amphiphiles into different structures to minimise the gibbs free energy. This describes why it is energetically desirable to form the lamellar microstructures (40).

2.5 The salting-out phenomena

The salting-out phenomena is defined as the decrease in solubility of a non-electrolyte in an aqueous solution. The addition of salt to a simple 2-component surfactant-water systems can significantly alter the phase behaviour of the system, a particularly interesting effect this addition can be responsible for is the formation of liquid crystal phases at much lower surfactant concentrations than would be possible without the presence of salt. This occurs because the surfactant precipitates out of solution upon the addition of the salt- the precipitate being liquid crystalline (44).

The addition of salt firstly results in a significant decrease in the CMC, and subsequently the addition of salt to the surfactant micelles results in changes in the aggregate morphology of a molecular scale, facilitated by an increase in counterion binding and dehydration of the surfactant headgroups. The mechanism behind the salting-out effect is rather complex and different forms of intermolecular interactions between the ion and solvent, ion and non-electrolyte and non-electrolyte and solvent need to be considered, and the extent of these interactions are heavily influences by the types of ions, non-electrolytes and solvents that are present (45).

There are multiple ways to describe the causes of the salting-out effect. The five main ones include: the hydration theories, water-dipole theories, electrostatic theories, internal pressure theories and van der-waals theories. These theories have limited applications in practice (46).

The simplest way to describe the causes of salting-out is by considering the chemical potentials of the system. Salting-out requires the chemical potentials of water and surfactant to be higher in the phase separated region than the two separate regions. Therefore, the chemical potential of water is higher than expected, resulting from an attractive interaction between micelles. Salting out electrolytes desorb from the surface of a micelle, increasing the surfactant chemical potential which results in the aggregation of the micelles and ultimately results in phase separation (46).

2.6 Lateral phase separation

In the study published by Richards et al (2), lateral phase separation was observed upon heating the coexisting micellar/lamellar region. This is an interesting phenomenon which results in the microscopic separation of different LAS isomers within lamellar bilayers. The mechanism behind this separation is as follows:

- Recall that for the 5-phenyl isomer of NaLAS exhibits an upper-consolute loop. Below this, 2 different lamellar phases with different concentrations coexist. This two-phase region can only exist because net attractive interactions between bilayers at separations of about 10-20A. This attraction strengthens as the temperature is decreased (47).

- These attractive forces are perhaps likely a result of a specific counterion binding mechanism, i.e. the concentration of counterions changes as a function of surfactant concentration and temperature hence there are correlations between ion positions on opposing layers give rise to attractive forces between bilayers which changes as a function of temperature and surfactant concentration (47).

- There is a 2-D lattice formed from the headgroups and counterions. As this lattice is formed in one layer, a similar lattice is formed on the adjacent layer, resulting in attractive forces.

- The presence of an isomer distribution may present a disruption in the lattice which can result in a reduction of the attractive forces.

- Therefore, there is a thermodynamic benefit lateral separation of the different isomers which can work to increase the attractive forces between bilayers.

- This behaviour is significant at 25°C, but as the temperature is increased, specific attractive forces responsible for the strong counterion binding fade, as does the isomer segregation.

The proposed schematic for lateral phase separation is shown in Figure 2.7.

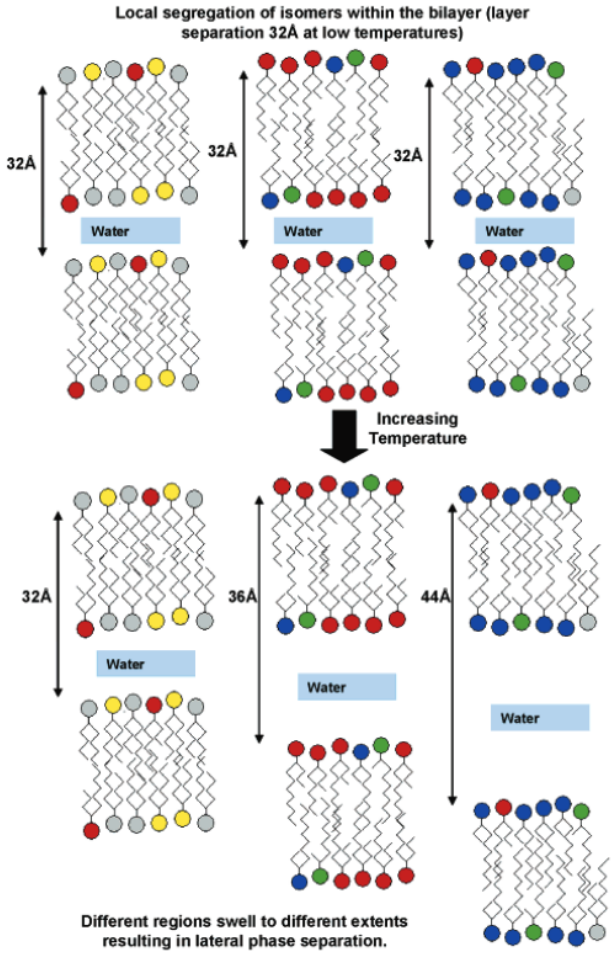

FIGURE 2.7: Schematic proposed by Richards *et al* (4) showing the mechanism of lateral phase separation of NaLAS in water.

2.7 Lamellar colloidal structures

Along with the phase structure, the colloidal structure of the lamellar phase is the other supramolecular structural consideration which is based more on the nano/micrometre scale, where as the phase structure is on the angstrom scale. The two main morphologies that the lamellar phase exhibits is the planar sheet morphology and the multi-lamellar vesicle morphology. The planar sheets consider the stacking of the bilayers perpendicular to one another and for all intents and purposes, they are generally treated as having unlimited dimensions. Multilamellar vescicles, which are often described as 'onions' exist when planar sheets fold

and close, forming the MLV structures which are concentric bilayers (48). An interesting property of multilamellar vesicles is that when they are formed as a result of their presence in a 2-phase pure amphiphile-water system, they are metastable, and over time they transition back into planar sheets (49).

2.8 The role of polymer in surfactant formulations

The solubility of polymer in water is highly dependent upon the interactions of the hydrophobic and hydrophilic segments of a polymer between themselves and with the water, just like the aggregation of surfactants. Therefore, when polymers are combined with surfactants in water, there is a wide array of interactions of behaviour patterns that can be observed. Quantitative studies of these interactions directly measures properties such as viscosity, conductance, volumetric and thermochemical properties. Again, these interactions are frequently illustrated by constructing phase diagrams. The main property to consider when considering the behaviour resulting from the interactions between surfactants and polymers is the charge of both the polymer and surfactant as well as the concentration of both species. For example, anionic surfactants are well known to interact strongly with polyethylene oxide (PEO) and polyvinylpyrrolidone (PVP) polymers, however cationic surfactants do not (12). When the surfactant and polymer are oppositely charged, phase separation is very common, in fact true solutions generally only exist at low polymer and surfactant concentrations.

In the detergent industry, polymers are usually combined with surfactants to behave as anti-redeposition agents, i.e. they prevent particles of dirt from redepositing onto the cleaned fabric during the cleaning cycle. The polymer adsorbs onto both the particles and the fabric and it reduces hetero- and homo-flocculation

Table 2.2: Different types of polymer and their roles in detergent products (12).

Type	**Molecular Weight**	**Effect**
Acrylic acid/maleic acid	High	Encrustation inhibitor, reduction of slurry viscosity, anti-redeposition agent
Acrylic acid/maleic acid	Low	Reduction of slurry viscosity, dispersing agent
Acrylic acid	High	Dispersing agent
Acrylic acid	Low	Anti-redeposition agent, dispersing agent
Graft polymers on polyalkylene glycol		Anti-redeposition agent Soil shield agent
Polyvinylpyrrolidone		Dye transfer inhibitor
Amphiphilic terephthalic acid polyester		Soil release agent

in the particle/fabric system. Table 2.2 shows various polymers that are commonly added to detergent product formulations and their function in the detergent product.

Polymers in detergent formulations generally behave as builders and anti-redeposition agents. Builders have the following roles in detergent formulations: to (i) disperse sparingly soluble salts, and prevent them from growing into larger crystals which deposit on fabric surfaces, (ii) to suspend colloidal soil in the wash liquor, preventing it from redepositing and graying the fabric, (iii) to buffer the pH of the wash liquor and maintain its alkalinity and, overall, (iv) to boost the performance of the surfactants and thus help to improve soil removal. The role of polymer on the structure of aniostropic lyotropic surfactant structures is currently poorly-explored.

2.8.1 Surfactant-polymer interactions

Ionic surfactants generally associate with polymers, and nonionics show weak interactions with most homopolymers. The association of an ionic surfactant to a hydrophilic homopolymer is strongly cooperative and starts at a quite well defined' surfactant concentration, the 'critical association concentration' (cac)(50). The association is best viewed as a polymer-induced micellization: in the presence of a polymer, micelles form at a lower concentration than the regular cmc. For ionic surfactants, micelle formation is strongly influenced by the unfavorable electrostatic interactions which lead to cmc values which are orders of magnitude higher than those of nonionics. Most cosolutes, such as weakly amphiphilic uncharged cosolutes and electrolytes, can reduce the electrostatic penalty and lower the cmc. Polymer molecules are especially effective in lowering the cmc because of the additive effects of several groups. This lowering is moderate for nonionic polymers but, typically, amounts to orders of magnitudes for oppositely charged polyelectrolytes. For non ionic surfacrants, the stabilization of the micelles by a homopolymer is small or insignificant, explaining why, generally, no association or lowering of the cmc is seen (51).

Phase diagrams of ternary systems of polymer, surfactant and water can be complex for several reasons. One reason is that there may be different types of phase separation phenomena depending on the molecular interactions, another that surfactant self-assembly can lead to several different structures and phases. A further aspect is that for mixtures of an ionic polymer with an oppositely charged surfactant, it is because of the different ways of pairing the ions, not possible to treat it as a ternary system. On mixing two homogeneous solutions, one of a polymer, and one of a surfactant, one can encounter three types of behaviour. In the first, there is a homogeneous solution. In the second, when there is an effective repulsion between the two cosolutes, there will be a segregative phase separation,

i.e. there is one phase enriched in polymer and one in (aggregated) surfactant(52). This will be expected for all cases without an attractive polymer–surfactant interaction Phase separation will be dictated by the weak entropic driving force of mixing for polymer and surfactant self-assemblies, phase separation increasing with increasing polymer molecular weight and micelle size.

In the case of a net attractive interaction, an associative phase separation, giving one concentrated phase enriched in both cosolutes coexisting with a water-rich phase, is expected. Associative phase separation could arise mainly because of electrostatic interactions between oppositely charged species or hydrophobic interactions. The simplest situation is to consider a nonionic polymer mixed with a nonionic surfactant (53). For less polar polymers and surfactants an associative phase separation will occur; for clouding polymers and surfactants, the phase separation can become much more accentuated at higher temperature. When considering polymer-vesicle interactions, we consider another situation of associative phase separation, i.e. that between oppositely charged species. The nature of the concentrated phase for such associative systems can vary depending on surfactant and on polymer–surfactant interactions; cases include a concentrated solution, a liquid crystalline phase and a solid precipitate. Since the aggregation number of a vesicle is much larger than for a micelle, phase separation phenomena are expected to be more pronounced with vesicles (53).

2.8.2 Interaction of polymer with the lamellar phase

Brookes and Coates (54) studied theoretically the role of polymer in dilute lamellar phases. The nature of the interaction of the polymer with the lamellar structures depends upon whether the polymer is adsorbing or non-adsorbing. For a lamellar phase which is bound (i.e., which cannot be indefinitely diluted) as a result of

van der Waals forces, the non-adsorbing polymer is completely expelled as a semi-dilute solution, leading to a compression of the lamellar stack. Adsorbing polymer can enter the phase, causing a slight reduction in the maximum layer spacing. For an unbound lamellar phase controlled by Helfrich forces, non-adsorbing polymer is expelled if the bilayers are stiff, but for flexible enough layers, a significant amount of polymer can be solubilised. At too high a volume fraction of polymer, part of the polymer is expelled as a solution, whereas at high surfactant fractions, a phase separation arises between two lamellar phases (one containing polymer, the other not). For the case of adsorbing chains, small amounts of added polymer cause the system to become bound with expulsion of excess solvent. For large amounts of added polymer, the unbound behaviour is recovered, whereas for intermediate polymer content, phase equilibria involve either two lamellar phases (each containing polymer), or one such phase coexisting with a polymer solution (54).

2.9 Time dependent structural changes of surfactant systems resulting from the application of shear

2.9.1 Overview

In the washing powder production process, the various formulation components such as liquid surfactant and polymer solutions as well as solid salts and zeolites are mixed in an industrial scale mixer for a few hours. As a result, the mixture experiences a high shear over an extended period of time. P&G have observed that in the formulating process, the measured torque increases in the mixture over time. This change in torque is likely result of structural changes occurring

due to the application of shear. Ultimately, the changes in structure that take place throughout the whole formulation process directly influences the structure of the final powder and the structure of the final powder directly influences the powder performance. An understanding of the structural changes that occur can help influence formulation decisions, as the cost-efficiency of the washing powder can potentially be improved by formulating in such a manner which can include a lower portion of the costlier components and a higher portion of the cheaper components, as well as help improve the performance of the washing powder. This chapter will explore how the structure of a model surfactant slurry system changes as it is sheared (5).

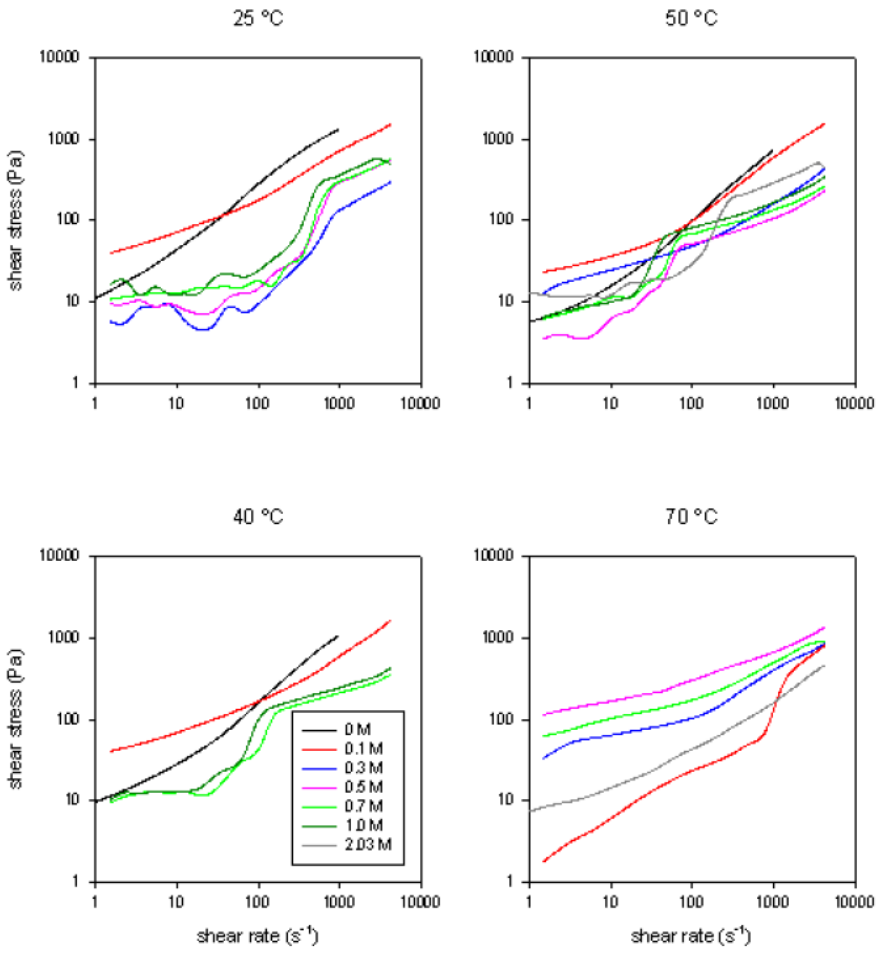

FIGURE 2.8: Flow curves showing the change in shear stress as a function of shear rate for 45 wt% NaLAS in water with increasing concentration of sodium sulphate (5).

It is difficult to achieve a perfect lamellar structure in any system. The lamellar phase usually contains many defects in the form of dislocation loops or thermodynamically stable defects where the lamellar bilayer is highly curved. Previous rheology studies on surfactant lamellar structures have shown that shear can induce the formation of MLVs in lamellar phases that contain defects (55), on the other hand, other studies, such as the work by Gustaffson (56) have shown that the presence of defects may in fact inhibit the formation of MLVs. A transition from parallel to perpendicular orientation was found in a broad range of shear rates, therefore the co-existence of two different lamellar orientations was concluded. In some cases it was found that a parallel orientation exists at low and high shear rates (57; 58).

The undulation stability of lamellar phase and it's contribution to structural changes as the sample is sheared have been the topic of various studies (57), (59). The mechanism proposed is that a layered system under shear leads to alignment of the layers parallel to the plates but they have a tilt that causes the layers to change their thickness. Above a critical shear rate, the lamyers develop undulations63. Zilman et al (57) proposed a mechanism for vesicle formation by considering instabilities in the undulations. Vesicles can only form above a critical shear rate, below which the shear stresses induced in the structure is balanced by the elastic restoring forces of the lamellar phase. Above the critical shear rate, the lamellae are curved into vesicles.

Chapter 3

Methods and materials

3.1 Outline of this section

This chapter will overview the main experimental techniques that will be utilised for the next 3 chapters. It will begin with an overview of NMR as a technique, providing some of the theory behind the fundamentals of the use of NMR in structural characterisation for anisotropic lyotropic systems by explaining the use of quadrupolar splitting, particularly for deuterium NMR. Following this, a theory of standard NMR measurements including T_1, T_2 and diffusion coefficients, all of which are useful for understanding the dynamics of the NaLAS-polymer-water and NaLAS-polymer-sodium sulphate solution systems. Following this, other techniques including cryo-SEM, centrifugation, SAXS and rheology are described.

3.2 NMR for structural analysis

Nuclear Magnetic Resonance (NMR) has long been established as a standard technique for phase behaviour analysis of surfactant systems. ^2H NMR quadrupolar

splitting can be used to study phase behaviour, ^{1}H NMR can be used to characterise micelles and ^{13}C NMR can be used for dynamics. This non-perturbing method uses nuclei already present in the molecules of interest or the labelling of these molecules by isotopic probes. First, it is a relatively insensitive method, although the development of high-field spectrometers and improved radio-frequency (RF) electronics as well as modem probe design has improved the sensitivity dramatically (the sensitivity is normally less of a problem when it comes to NMR investigations of surfactant systems as these usually deal with concentrated samples), however the sensitivity rarely a problem in the case of the analysis of lyotropic surfactant phase structure as the systems of interest usually are concentrated. Second, NMR spectrometers are costly, although in comparison with the scattering method, the other main technique for studying supramolecular assemblies, the cost is not prohibitive. Also, NMR spectrometers, and their associated probes are usually expensive (60).

3.2.1 Theory behind NMR

NMR results when the nuclei of specific atoms entering a strong magnetic field are perturbed by a weaker oscillating field. This results in the nuclei producing an electromagnetic signal with a characteristic frequency corresponding to the frequency at the nuclei, the frequency is known as the larmor frequency, Ω_L. This behaviour arises from the characteristic spin property that nuclei possess. This spin number is characterised by the spin quantum number, I and is possessed by protons, neutrons and electrons in atomic nuclei. I is used to describe the magnetic properties of nuclei which is expressed in multiples of 0.5 (52). Nuclei with I greater than 0.5 such as ^{2}H, ^{14}N, ^{23}Na and ^{35}Cl spin have a non-spherical body and an electric field gradient, *eq*, is induced when a probing charge approaches as this will experience different electrostatic fields in different approaching directions. All nuclei with a spin greater than 0.5 are therefore termed electric quadrupoles.

Deuterium (^{2}H) therefore has a quadrupole moment, Q, which is 0.0028x10^{-28}m^2. Deuterium (^{2}H) has a spin quantum number I=1, and has 3 potential alignments in a magnetic field. However, interaction between the nuclear quadrupoles and electric field gradient leads to rapid changes of the spin states of the nuclei, which further leads to an additional splitting of the energy level when m=0(61). The energy levels are shown in Figure 3.3 where eQ is the angular term relating the different angles between the principal coupling tensor, V, and the applied magnetic field. An NMR experiment involves studying a collection of interacting nuclear spins. In the simplest cases, these are the spins of nuclei in one molecule, or in a portion of one molecule; this group of spins is called the spin system. The entire (bulk) sample consists of a (statistical) ensemble of spin systems. Understanding the theory either of a single spin system or of a multiple spin systems starts with considering the Hamiltonians of the system. The total Hamiltonian, H, for any particular spin system is the summation of individual Hamiltonians that describe all the interactions of the system.

The Hamiltonian of a single atomic nuclei of spin operator I_i and gyromagnetic ratio, γ, immersed in an external magnetic field, B_0 is expressed as follows (60):

$$H_i = H_Z + H_{CS} + H_J + H_D + H_Q \tag{3.1}$$

Where the H represents the Hamiltonian and subscripts Z, CS, J, D and Q correspond to Zeeman, Chemical shift, internuclear scalar coupling, internuclear dipolar coupling and the quadrupolar splitting. Each respective hamiltionian term is responsible for a wide array of information for multiple systems including structure, dynamics, orientation and the position of which the nuclei of interest is located (62) (63).

TABLE 3.1: Hamiltonians corresponding to the energy of a single nuclei immersed in an external magnetic field.

Hamiltonian type	**Definition**
H_Z, Zeeman	The magnetic interaction between the nuclear spin and the sprectrometer's external magnetic field, B_0.
H_{CS}, Chemical shift	The effect of the electron cloud surrounding the nuclear spins.
H_J, Scalar coupling	Interaction of pairs of nuclear spins through bonding electrons.
H_D, Dipolar coupling	Dipolar coupling interactions of nuclear spin pairs through space, H_D.
H_Q, Quadrupolar splitting	For nuclei of spin greater than or equal to 1. This describes the interactions of the quadrupolar dipolar moment with the electric field gradient at the site of the nucleus.

As the Zeeman interaction is much larger than the other Hamiltonian terms, the non-Zeeman terms are often expressed as a first-order perturbation relative to the Zeeman Hamiltonian, this is known as the Zeeman approximation. In cases where molecular movement is fast, the Hamiltonians are expressed as a sum of time averaged terms, this is known as the motional approximation. These 2 approximations consequently enables an analysis of molecular structural properties of aggregates (i.e. allows the analysis of transition frequencies and splitting, but it does not allow the analysis of any molecular dynamics because it removes any sources of relaxation from the system). When considering a ^{2}H spectra, for which the motional and secular approximation has been applied, the spin Hamiltonian can be equated to the quadrupolar Hamiltonian, as follows (60)

$$H_i = H_Q = \frac{3}{2}\chi(P_2 cos\theta_{ml})[3[I_z]^2 - I(I+1)] \tag{3.2}$$

Where the subscript m and l represent the molecular (bond vector direction) and laboratory (magnetic field direction) axis respectively, $P_2 cos(\theta)$ is the second Legendre polynomial, where χ is the quadrupolar coupling constant, which can be defined as:

$$\chi = (e^2 qQ)/h \tag{3.3}$$

Where e is the unit charge, eq is electric field gradient, and Q is the nuclear quadrupole moment, but more importantly χ is characteristic for each bond and for C-D it is equal to 176 kHz. As the secular approximation can be applied, $(P_2 cos\theta_{ml})$approximates to 0 in isotropic liquids. However, in anisotropic liquid crystal systems a quadrupolar splitting pattern arises (60):

$$\Delta\nu_Q = \frac{3}{2}\chi(P_2 cos\theta_{ml}) \tag{3.4}$$

Equation 3.4 shows the quadrupolar splitting parameter is directly proportional to the orientational order parameter, s which is described further in Chapter 3, so it is an suitable technique for the characterisation or order in a lyotropic system.

3.2.2 The vector model

It is difficult to understand how NMR works effectively without having an understanding of the vector model (64).

In NMR, we can consider a spin system to behave like a magnet, as in they possess a magnetic dipole moment (the magnetic moment is the magnetic strength and orientation of a magnet or other object that produces a magnetic field). In a standard sample of any material, the spins are aligned in random directions, and therefore cancel out, so there is no net magnetic moment. However, if a sample is placed in a magnetic field, the spins align with the direction of the magnetic field they are placed in, B_0, and there is a net magnetic field along that direction. This is known as the bulk magnetization of the sample along the direction of the field. This is shown in Figure 3.2.

Say that the magnetization vector was shifted by an angle β from the z-axis. The magnetic field vector will end up moving around the z-axis angle along the x-y

plane, maintain an angle β from the z-axis. It can be said that the magnetization is precessing at a frequency which is known as the Larmor frequency. This is defined in Equation 3.5, where B_0 is the magnetic field strength (6).

$$\nu_0 = \frac{\gamma B_0}{2\pi} \tag{3.5}$$

The frequency, ν_0 is the frequency observed in an NMR spectrum. The detector of an NMR machine detects the Larmor frequency. The Larmor frequency is detected by a detector along the x-y plane. Whenever a magnetic vector passes through the x-y plane, an electric current is detected by the detector(65).

If the system is at equilibrium, the magnetization vector is at B_0 and no electric current is detected by the detector. The vector can be moved if the transmitter of an NMR machine transmits a radiofrequency (RF) signal along the x-y plane. The frequency of the signal must be resonant with the Larmor frequency. The coil that transmits the RF wave is the same as the one that detects the magnetization. Following the application of the RF wave, an oscillating current is detected. If the applied RF wave is 90° to the equilibrium magnetization detector, it is referred to as a 90° wave which moves the magnetization vector from the z to the x-y plane. Following the application of the pulse, the detected current is not there infinitely. The magnetization vector begins to relax back to equilibrium, and the detected oscillating field decays, this is free induction decay(6).

Figure 3.1 shows a schematic block diagram of a standard NMR set-up.

3.2.3 Relaxation

The chemical shift, dipolar and quadrupolar shift Hamiltonians depend upon the ensemble averaged orientation angle of the spin system relative to the magnetic

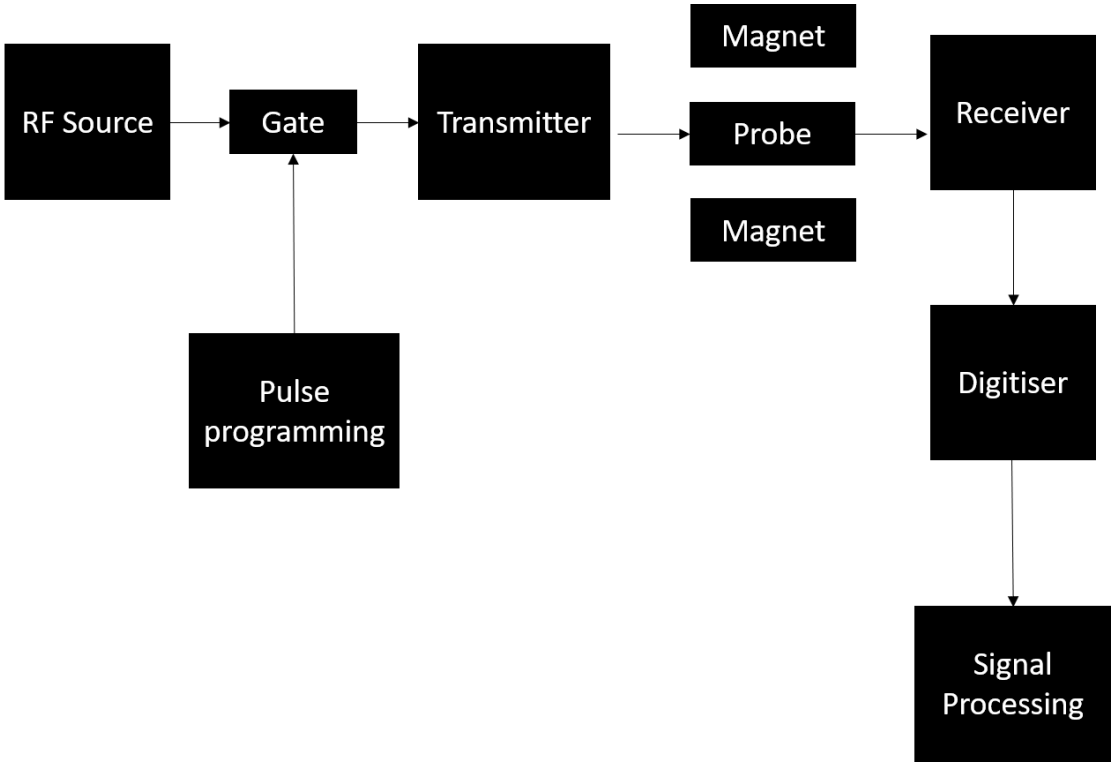

FIGURE 3.1: A simple block diagram of the main components of an NMR set-up. The probe is arguably the most important part of the set-up, as it is responsible for exciting nuclear spins and detecting NMR signals. Recreated from (6).

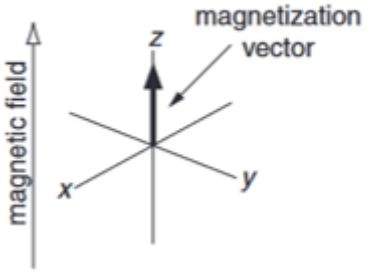

FIGURE 3.2: At equilibrium when place in a magnetix field, a sample has a net magnetization along the magnetic field direction (the z-axis) which can be represented by a magnetization vector. The axis set in this diagram is a right-handed one (6)

field B_0. Any changes in these orientation angles causes the Hamiltonians to fluctuate, and this hence results in nuclear relaxation. The longitudinal and transverse relaxation rates, $1/T_1$ and $1/T_2$ respectively is an effective way to characterise these fluctuations. They describe the spectral density of these fluctuations at a defined frequency - one that corresponds directly to the transition energies between the eigenstates of the Hamiltonians. $1/T_1$ is also known as the spin-lattice relaxation time (the interaction of the nuclear spin within a system with the surrounding medium or 'lattice') and $1/T_2$ is the spin-spin relaxation time (the interaction of the nuclear spin with the surrounding spins). The T_1 relaxation time is defined as a rate constant describing the decay of the longitudinal magnetization of a spin system to the thermal equilibrium following magnetization resulting from the application of an electric field, where as the T_2 relaxation time is the decay constant showing the decay of the transverse magnetization, as follows (66), (67):

$$M_z = M_0(1 - e^{\frac{-T_1}{\tau_c}}), \tag{3.6}$$

$$M_{xy} = M_0(1 - e^{\frac{-T_2}{\tau_c}}). \tag{3.7}$$

M_z is the magnetization (the vector field that expresses the density of permanent or induced magnetic dipole moments in a magnetic material) in the direction parallel to the magnetic field time t after the application of an electric field, M_{xy} is the magnetization in the transverse direction time t after the application of an electric field, M_0 is the magnetization at thermal equilibrium and τ_c is the correlation time. When considering the relaxation of a spin system, the correlation function, $G(\tau)$ describes the isotropic diffusion of a rigid rotor (in this case the rigid rotor is the spin). This function is dependent upon the correlation time, τ_c, is the time constant for the time decay of the correlation function. This correlation time is defined as the time taken for a molecule to spin one radian and this correlation time is influenced by properties such as molecular size, shape, solvent viscosity

and temperature. The correlation function is equated as follows:

$$G(t) = \frac{1}{5} e^{\frac{-t}{\tau_c}}. \tag{3.8}$$

The fourier transform of the correlation function is known as the spectrum density function, J(ω). Systems that relax rapidly and have a low value of τ_c results in broad lines in NMR spectra, they also result in a broad spectral density function. This is because fast tumbling molecules (molecules with a high τ_c) can sample a wide range of frequencies and slower tumbling molecules sample less. The spectral density function is as follows: (68; 69):

$$J(\omega) = \frac{2}{5}(\tau_c/(1 + \omega^2[\tau_c]^2)), \tag{3.9}$$

From the cross-correlation function, the T_1 and T_2 rates can be described specifically for the C-^{2}H bonds as follows (68) (69):

$$1/T_1 = (\pi^2[d_{CH}]^2)/5[J(\omega_h - \omega_c) + 3J(\omega_c) + 6J(\omega_h + \omega_c)], \tag{3.10}$$

$$\frac{1}{T_2} = \frac{(\pi^2[d_{CH}]^2)}{10[4J(0) + J(\omega_h - \omega_c) + 3J(\omega_c) + 6J(\omega_h) + 6J(\omega_h + \omega_c)}, \tag{3.11}$$

where ω_h and ω_c are the Larmor frequencies of ^1H and ^13C respectively, $J(\omega)$ represents the spectral frequency and frequency ω.

3.3 NMR acquisition

. These equations show that both T_1 and T_2 relaxation times are directly related to the correlation time. Larger molecules have a larger correlation time and this results in the T_2 value decreasing with increasing correlation time. So in general, solids have a lower T_2 value than liquids which have lower T_2 values than gases. For T_1, the relationship between correlation time (and hence molecular size) initially

shows a decrease in T1 as the correlation time increases until a value of $1/\nu_0$ is reached, when the T1 increases as the correlation time increases. This can be related to the sizes of a dispersed phase in a colloid. Generally, when the sizes of the droplets of a dispersed phase are larger, the T2 value is lower (70).

For the most basic NMR acquisition, a pulse sequence can involve a 90° radiofrequency (RF) pulse (which is a radiofrequency wave that is 90° to the direction of the net magnetization of the spins in the magnet) this 90° pulse rotates the magnetization vector to the y axis. This followed by a acquisition of the free induction decay (FID) of emitted RF radiation, which results as the magnetization return to an equilibrium. The pulse sequence can be very simple for a simple spectrum acqusition or be more complex with multiple pulses applied in different directions, especially ion experiments with different nuclei applied, various waiting times and acquisition times (70).

The fourier transform of the FID transforms the time-domain signal to the frequency-domain signal. It is the frequency domain data that gives the standard NMR spectra which contains the interesting information regarding chemical shifts, dipolar and quadrupolar splitting. Due to this fourier relationship between the time and frequency domain, the half width at half maximum of the peaks ($\Delta\nu_{1/2}$) in the NMR spectrum can be related to the T_2 decay time as follows (70):

$$\frac{1}{T_2} = \pi\Delta\nu_{1/2}. \tag{3.12}$$

3.3.1 Quadrupolar splitting in NMR spectra

When considering deuterium NMR in anisotropic liquid crystal systems, quadrupolar splittings (with magnitudes usually on the scale of kHz) are exhibited as a result of the alignment of the liquid crystal molecules relative to the magnetic field and this splitting is directly related to the ensemble average angle to which an ensemble

of molecules align relative to the magnetic field direction, B_0. As deuterium has a spin of I=1 so therefore there are 3 energy states corresponding to the nuclear spin angular momentum. Transfer between adjacent energy levels are allowed, so there are 2 energy spin transitions. the degeneracy of the transitions is removed by the quadrupolar coupling. The perturbation of the energy level states results from this quadrupolar coupling as the quadrupole moment of the ^{2}H nucleus with the electric field gradient of the ^{2}H bond. In determining the ^{2}H NMR line shapes, you begin with the perturbing Hamiltonian, then determine the energy level shifts are calculated and finally the frequencies of the spectral lines are calculated: (71) (7).

$$\nu_Q^{\pm} = \mp\frac{3}{4}\chi_Q D_{00}^{(2)}(\Omega_{PL}) - \frac{\nu_Q}{\sqrt{6}} D_{-20}^{(2)}(\Omega_{PL}) D_{20}^{(2)}(\Omega_{PL}). \tag{3.13}$$

χ_Q is the static quadrupolar coupling constant, ν_Q is the corresponding asymmetry parameter of the electric field gradient tensor, Ω_{PL}=$(\alpha_{PL}, \beta_{PL}, \gamma_{PL})$ are the Euler angles of the EFG principal axis system. So, the quadrupolar splitting that can be observed in ^{2}H NMR spectra is defined as the difference in frequencies between the spectral lines, as shown in Figure 3.3.

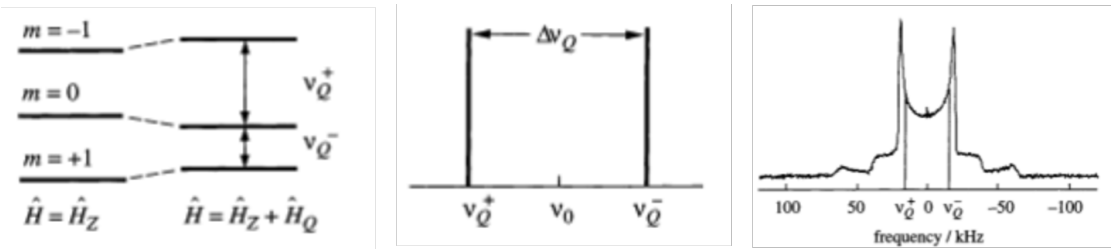

FIGURE 3.3: The difference in frequency levels for the quadrupolar splitting spectral lines are schematically shown, along with an exemplar spectra. Recreated from (7)

.

Figure 3.4 shows how orientational order can influence the quadrupolar splitting (distance between 2 shoulders) in deuterium NMR, it is hence incredibly useful for the characterisation of orientational order.

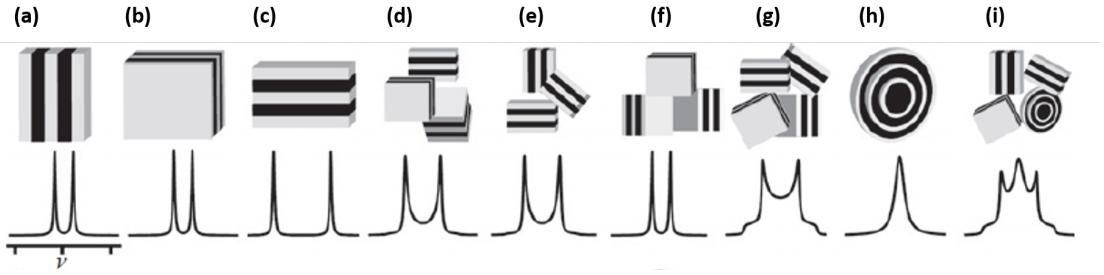

FIGURE 3.4: A figure showing exemplar ^2H NMR spectra for various lamellar surfactant structures and how their orientation affects the spectra observed. The spectra can be characterised in terms of the quadrupolar splitting, which shows the distance between 2 peaks. Vesicles have no average orientational order so they have a broad central peak at 0Hz (7).

.

3.3.2 Causes of relaxation

Relaxation in NMR is a result of the interaction of spins with magnetic fields that result from magnetic dipoles fluctuating as a result of random and translational molecular motion. The nature and the rate of the molecular motions affect the T_1 and T_2 relaxation times. Molecular motions that occur at a frequency similar to the nuclear resonance frequency, ν_0 result in the lowest T_1 values. Equations 3.14 and 3.15 are another way to define the spin-spin and spin-lattice relaxations (64; 72):

$$\frac{1}{T_1} = \gamma^2 \overline{H^2} \frac{\tau_c}{1 + (2\pi\nu_0^2\tau_c)^2} \tag{3.14}$$

$$\frac{1}{T_2} = \gamma^2 \overline{H^2} \left(\tau_c + \frac{\tau_c}{1 + (2\pi\nu_0^2\tau_c)^2} \right) \tag{3.15}$$

$\overline{H}^2$ is the mean-square average of the local magnetic fields, i.e. a measure of the strength of the interaction between the nuclear spin and the fluctuating magnetic fields, and τ_c is the correlation time. The correlation time is a quantitative measure of the rate of a molecular motion. For rotational motion it is essentially the average length of time required to rotate through an angle of 33°. For translational motion, the correlation time is the average time required for a molecule to move through a distance equal to its diameter.

From Equation 3.14, it can be seen that the T_1 value is lowest when correlation time is equal to $\frac{1}{2\pi\nu_0^2}$. It's clear from Equations 3.14 and 3.15, increasing the correlation time has different effects on both T_1 and T_2.The correlation time can be directly related to the molecular weight of the molecules, and hence it can be seen that different sized molecules have different T_1 and T_2 rates. Another deduction that can be made from Equation 3.14 and 3.15 is that the T_1 and T_2 is depended upon ν_0, so the T_1 value can change, depending on the magnet the nuclei spin are interacting with; a different magnet which has a different magnetic field strength will show a different T_1 value when $2\pi\nu_0\tau_c$ is close to or greater than 1. For T_2, there is also a dependence of the frequency on T_2, so the magnetic field strength of the magnetic field interacting with the nuclear spins can influence the T_2 values (64). The value of T_2 may also depend on frequency (and therefore magnetic field strength), but for values of correlation time which are really short, $2\pi\nu_0$ is very small with respect to 2 in the denominator of Equation 3.15. When the correlation time is high in the case of larger molecular weight molecules, the T_2 values are independent of the frequency and the magnetic field strength.

For extremely small molecules moving freely in solution, and consequently with short τ_c, $2\pi\nu_0$ will be negligible compared with 1 in the denominator of Equation 3.15. For large macromolecules or complexes, τ_c will be large compared to $\tau_c[1 + (2\pi\nu_0\tau_c)^2]$, and T_2 will be independent of ν_0 (and B_0) (64; 72).

3.3.3 Equipment

A Bruker Ultra-shield plus 400-MHz-NMR was used with a deuterium probe. Each sample that was analysed was individually shimmed and each sample was left to equilibrate at the analysis temperature with the magnetic field for 40 minutes at $50°C$. Shimming is carried out by a device called the shim and is necessary for high resolution data. It corrects any inhomogeneities in the applied magnetic field

resulting from variations due to any imperfections in in the main magnet or any deviations in the main magnetic field as a reults of the presence of the sample and probe in the field.

The samples were frequently prone to phase separation, so for this reason, it was important that samples were prepared well in advance of analysis. The samples were analysed 5 days after sample preparation and 32 scans were carried out on each sample in order to minimise the signal to noise ratio. Each NMR tube was filled 3 days before sample analysis (and the tubes were kept at $50°C$) The positioning on the sample within the NMR tube was important, as only a small part of the tube was contained within the NMR coil. Therefore, great care was taken to position the tube to ensure that just the lamellar phase was analysed during all the experiments in all experiments (in the cases where the structure of the vesicles or pores were being explored). In the case of the analysis of micelle system, as the system was always one phase, the position of the tube was not important.

Temperature control was achieved using a combination of a water bath and a peltier heater. The Tospin software used to control the machine has a variety of NMR pulse programs and the ability to run custom-written pulse programs. Depending on the experiment of interest either a ^1H or a ^2H probe was used.

3.4 Diffusion NMR

3.4.1 Pulsed field gradient NMR

Pulsed field gradient (PFG) NMR is based on the dependence of the Larmor frequency, Ω_L, on the amplitude of the applied magnetic field. By adding magnetic

field gradient pulses, one can label the positions of the spins by the Larmor frequency and by the phases accumulated due to the rotation with Ω_L, in the local field. If the molecules where the spins are located do not change their positions during the time of diffusion measurements, the PFG NMR signal is refocused and can retain the maximum intensity. But, if there is a displacement of the molecules during this time interval, the measured spin-echo signal some of its intensity. The resulting signal attenuation, S gives a measure of the movement of the molecules.

A more complex experiment can be carried out using either the ^{2}H probe or ^{1}H probe to determine the rates of molecular diffusion. This is known as a Pulsed Field Gradient experiment. Pulsed field gradient (PFG) NMR can be used to determine the diffusion coefficient of the water associated with an NMR spectra peak. This method employs two magnetic field gradient pulses of strength G and duration δ which are separated by an observation time Δ. In the case of diffusion, where molecular motion is incoherent, molecular displacements over the time scale Δ produce a distribution of phase shifts in the magnetic resonance (MR) signal, resulting in an attenuation of the MR signal. The NMR signal is acquired over a range of G values and a diffusion coefficient can be calculated by a least-square fitting of the Stejskal-Tanner equation (73):

$$S = S_0 e^{-bD}, \tag{3.16}$$

where

$$b = \gamma^2 G^2 \delta^2 \tau. \tag{3.17}$$

The symbol γ is defined as the gyromagnetic ratio of the nucleus, δ is the duration of the gradient pulse, τ is the separation time between pulses, D is the self-diffusion coefficient of the molecule of interest (in this case D_2O), S is the peak intensity at a given value of G and S_0 is the intensity when G=0.

3.4.2 Pulsed-gradient stimulated train echo NMR

Diffusion experiments benefit from keeping Δ delay long in order for the so the molecules can travel a longer distance which results in a stronger signal intensity. In the PFG sequence the signal can, however, be lost during the echo time 2τ, because of the transverse spin relaxation which imposes a limitation on the maximum value of Δ. This limitation can be overcome in PGSTE, where two 90° pulses that are separated by a delay time, $\tau 2$, replace the 180° pulse in the PFG sequence. By implementing this change, the relaxation of the magnetization is mainly governed by T_1, which is very useful in those cases where the $T_1$is larger than T_2 (this is a common occurence). The first 90° pulse in the pair turns the transverse magnetization in the direction along the z-axis,and throughout the delay time, $_\tau 2$, the spins thereafter evolve by the longitudinal relaxation. The final 90° pulse functions to transfer the magnetization back to the xy-plane, hence signal can be detected. The intensity in the PGSTE is given by (74):

$$S = 0.5 S_0 e^{-bD}, \tag{3.18}$$

PGSTE experiments were performed on a vertical wide bore 89 Bruker 400 MHz- spectrometer equipped with a 7.0 T superconducting magnet, operating at a frequency of 400 MHz. A 10 mm radiofrequency resonator was used and measurements were performed at 323 K. Typical parameters used in these experiments were $\delta = 1$ ms, $\Delta = 20$ ms (Δ was varied in the experiments carried out in the 3rd results chapter), with a maximum gradient, Gmax, of 12.13 G/cm. There were 16 gradient steps, so the signal was attenuated to ensure $S(G)/S(0)$ at Gmax was $\leq$ 0.01.

3.5 Optical microscopy

Light is an electromagnetic wave, consisting of an oscillating electric field with a magnetic field oscillating perpendicular to this. The electric field is shown by the wave vector at any point along the wave. The magnetic field oscillate is an ellipse in the plane perpendicular to the one the electric field travels along.

Microscopy involves visible radiation incident upon a sample passing through or reflected off the surface of the sample which passes through a single lens to facilitate a magnified view of the sample. The light source can originate from an independent light source in the microscope, or from an external source which is reflected onto the underside of the subject. The light can be attenuated and can be focused so that a high resolution image can be obtained by using a condenser and and iris aperture diaphragm.

Cross-polarised microscopy is useful for identifying anisotropic liquid crystal phases. When light is incident upon liquid crystals, the light is broken into two components, one component which is fast and one that is relatively slow. This difference in velocities results in a phase difference between the light rays. As these 2 light rays recombine after leaving the liquid crystal, this difference in phase means that that the polarisation of the light changes. When these lights recombine after leaving the anisotropic crystal, because of the phase difference, destructive interference occurs (75).

Lamellar structures have the ability to rotate plane polarised light because the molecules exhibit polarisability anisotropy, and are able to transform linearly polarised light into eliptically polarised light. Micelles, however are unable to do so. Therefore, cross-polarised microscopy can effectively be distinguished using by placing a sample between two polarisers placed perpendicular to one another and viewing the sample under a microscope.

Liquid crystalline properties can form for a variety or organic molecules such as surfactants, polymers, various polymer systems and various biological systems. Lamellar structures appear textured on these images as a result of their ability to rotate the light. There are changes in refractive index resulting from light entering the anisotropic lamellar phase. The phase difference that results between the incident light being split into 2 rays is proportional to the change in refractive index as shown in Equation 3.19.

$$\Delta(phase) = \frac{2\pi}{(n_1 - n_2)t} \tag{3.19}$$

Δ(phase) is the phase difference in, lambda is wavelength of the light in m, n1 is the refractive index of the first ray the original ray is split into and n2 is the refractive index of the second (75). A polarizer acts to allow light oscillating in one plane direction to pass through it. When analysing liquid crystals, 2 polarising filters are used to provide a cross-polarising set-up. One filter is placed in a position between the light source and the sample, allowing the light incident upon the sample to be filtered to that light in one direction only is incident upon the sample, but as described, when the light leaves the sample, birefringence results in the incident light splitting and recombining with interference so a second analysing polarising filter is placed after the sample which is perpendicular to the original filter. This means that the light entering through the first filter has all been filtered except light in one plane. The East-West plane and the second filter blocks all light paths except all oriented in the North-South plane. If there is no sample between the polarising filters, nothing can be seen but because of the splitting of the light from the anisotropic liquid crystal, the texture of the liquid crystal can effectively be seen when cross-polarization is used (76).

All non-cubic liquid crystals show distinctive textures under a cross-polarizing microscope. When some of the liquid crystals are contacted with a small amount of

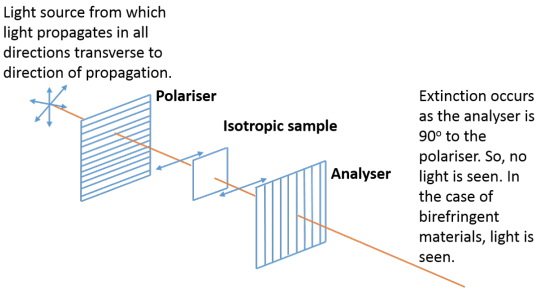

FIGURE 3.5: Cross-polarisation of light.

water, interfacial changes are seen and defined bands characteristic of specific liquid crystal structures are seen. This is a useful tool in characterising the presence of multi-lamellar vesicles as self-assembling surfactant structures exhibit birefringence, and multi-lamellar vesicles appear as maltese crosses on such a microscope. Lamellar structures are uniaxial, meaning that the index of refraction parallel to the optic axis, is larger than that perpendicular to it. Therefore, lamellar sheets can be identified by the presence of oily streak textures. However, lamellar surfactant structures have a tendency to align homotropically over time, i.e. the director aligns parallel to the optic axis. In this case, gently shearing the sample on the microscope, perhaps by poking it with a sharp object, such as a needle, can help determine whether the sample is homeotropically aligned, or isotropic. Multilamellar vesicles appear as maltese crosses between cross-polarisers. The 'arms' of the maltese crosses appear dark, this is because the molecular axis are aligned with either polariser. Examples of liquid crystal phases are shown in Figures 3.6 to 3.10 (10).

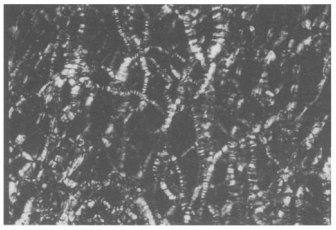

FIGURE 3.6: Birefringent oily streak texture exhibited by lamellar phases (8)

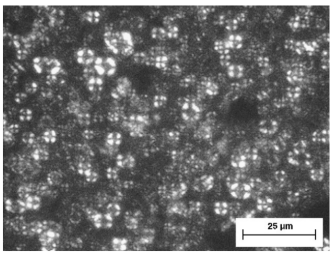

FIGURE 3.7: Birefringent maltese cross strutures exhibited by lamellar phases (9)

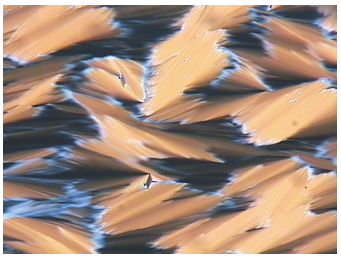

FIGURE 3.8: Birefringent texture of a liquid crystal phase - known as the Smectic A* phase (10)

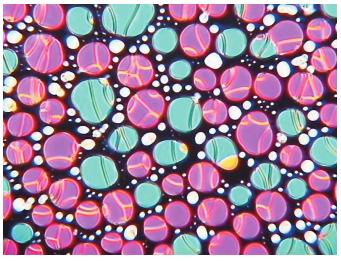

FIGURE 3.9: Birefringent texture of a liquid crystal phase - known as the Cholesteric phase (10)

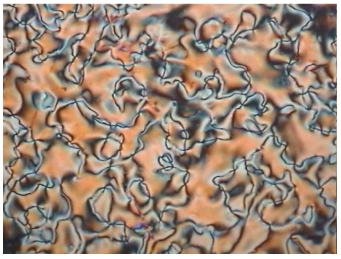

FIGURE 3.10: Birefringent texture of a liquid crystal phase - known as the Nematic phase. This distinct texture is known as the Schlieren textur (10)e.

3.5.1 Equipment used

A Leica DM2700 P polarising microscope was used with a Linkam THMS600 hot stage. In some cases, a full wave plate was placed along the optical path to enhance birefringence. It was equipped with two polarisers 90° to one another.

3.6 Cryo-SEM

SEM, or scanning electron microscopy works by focusing a beam of high energy electrons onto a sample in order to create an image of the sample. It allows visualisation of surface structure and composition. The main appeal of SEM is its ability to achieve extremely high magnifications, of up to 1,000,000. The depth of field of SEM is high which is highly advantageous as it means that the image remains focused regardless of the magnification. This is a problem generally found in light microscopy as light microscopy has a reduced depth of field as the magnification increases. The radiation source for this technique is electron which are extremely small in size, approximately 10-16 metres which contributes to the ability of this technique to achieve such high magnifications (77).

This technique involves a gun bombarding a beam of electrons at a sample which then interact with the sample under vacuum, and as a result of this interaction, electrons are back scattered and secondary electrons are released and these electrons are used to create the image. High atomic mass atoms will scatter more of the electrons than atoms with a lower molecular mass and this difference in scattering is utilised to generate the image. The backscattered electrons usually show the morphology and topography of the sample whereas the secondary electrons are useful in showing contrasts in compositions that consists of multiple phases.

SEM is a non-destructive analysis technique so the sample can be analysed many times (78). The main disadvantage of SEM is that the sample needs to be solid. To overcome this limitation, Cryo-SEM can often be used for hydrated samples, and the sample is frozen. This freezing is facilitated by plunging the sample into liquid nitrogen and keeping the sample at a low temperature as the sample is analysed by SEM (79).

3.6.1 Equipment used

For SEM both a Hitachi SU8230 high performance cold field emission SEM as well as a FEI Quanta 200 FEGESEM. In both systems, samples chambers were frozen, only a small amount of sample was necessary, about a pea sized sample was placed onto the sample holder which was plunged into the liquid nitrogen. fractured with a blade and samples were spluttered with platinum.

3.7 Small angle X-ray Scattering

Small angle X-ray scattering (SAXS) can be used to analyse shapes and structures and sizes of particles. SAXS involves the focusing of X-ray beams in a sample and all the particles within the sample that the beam comes into contact with scatter, absorb or reflect the X-rays. The scattered X-rays that are released can be used to determine the average structure of the particles that were hit by the X-rays the fact that the average structures are determined by SAXS is important as if there are structural details that are not pronounced enough throughout the sample, the SAXS equipment will not pick up on them. The usage of SAXS is well documented throughout literature and has applications in chemicals, metals, materials, food science, polymers and colloids. SAXS is named as such because the angle of incidence of the x-rays is between 0.1 and 10°. SAXS begins with the incident X-rays interacting with the particles within the sample. There must be a difference in electron density between the particles and the solvent in order to establish a contrast. Once the X-rays have been scattered by the particles in the sample, a lens system is used to reconstruct the scattering pattern. The strength of the signal is proportional to the volume of the particles cubed, therefore it's very difficult to detect small particles when large particles are present. The size of particle that can be resolved is dependent upon various variables: a smaller aperture, scattering

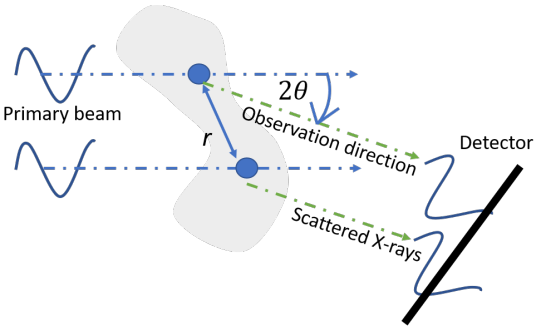

FIGURE 3.11: The configuration of small angle-x-ray experiment

angle and larger distance of the sample from the lens will result in a larger object being visualised. X-rays irradiate the atoms in sample, and this results in the scattering of the radiation in all directions, this results in background radiation which is constant. Particles that are irradiated by the radiation produces extra scattering resulting from density differences within the sample. A measurement of the angle-dependent distribution of the scattered radiation allows understanding of the particle structure of the irradiated sample. X-Rays can be detected by the absorption process; usually one or a combination of the following are used: solid-state detectors, gas-filled detectors and scintillating detectors. When X-rays reach the particles in the sample, they interact with the sample as such each atom releases a spherical wave. There are, however, some beams which are not incident upon the sample and the beams scattered from the particles and atoms interfere with the waves that do not interact with the sample and/or with waves that have been scattered by other atoms in the sample. Interference can be constructive or destructive. When the interference is constructive, detector receives a bright signal but when it is destructive, the sample receives a dark signal. This is represented in Figure 3.12. Therefore, an interference pattern is produced as a result of the different waves received by the detector. When referring to Figure 3.11, it is possible to mathematically model the scattering pattern, using Equation 3.20:

$$q = \frac{2\pi}{\lambda.sin(\theta)} \tag{3.20}$$

Where q is the momentum transfer in nm^{-1}, λ is the wavelength in nm, θ is the scattering angle in radians. The form factor, *p(q)*, shows the scattering from a single particle that is dependent upon the size and shape of the particle. The interference pattern shows the interference resulting from the waves detected from each electron/atom from the particle. The amplitude of each wave received by the detector is subsequently squared and summed to give an interference pattern known as the form factor, this is then scaled with a constant value which allows the pattern to match the units of the experimental intensity. This factor is generally used for dilute systems (80). The structure factor is used when the system is concentrated, so the distances between the particles are in the same magnitude of the distances between variations of electron density between the particles. Therefore, the scatter pattern will show the electron density distributions within a particle and between particles. This contribution from the neighboring particles can be multiplied by the form factor to give the structure factor. This wave can be produce a very pronounce peak, known as the Bragg peak. The momentum transfer at this peak can be related to the distance between different particles as shown in Equation 3.21.

$$d_{bragg} = \frac{2\pi}{q_{peak}}. \tag{3.21}$$

A typical SAXS set-up is shown in Figure 3.12. The X-ray source in desktop SAXS is usually a rotating anode or a micro-source, Synchotron sources have the ability to produce X-rays of all wavelengths and allows a high flux to be achieved. The collimation system is used to separate the incoming beam from the scattered X-rays which is simply a set of narrow splits through which the beams must pass. The sample holder must be under vacuum to minimise background scattering and should allow the control of temperature. The beam stop prevents high intensity direct beams from hitting the detector when the signals of interest are the weaker scattered beams. The detector, as previously mentioned, acts to absorb the X-ray for analysis. The types of detectors available include: wire detectors, CCD and

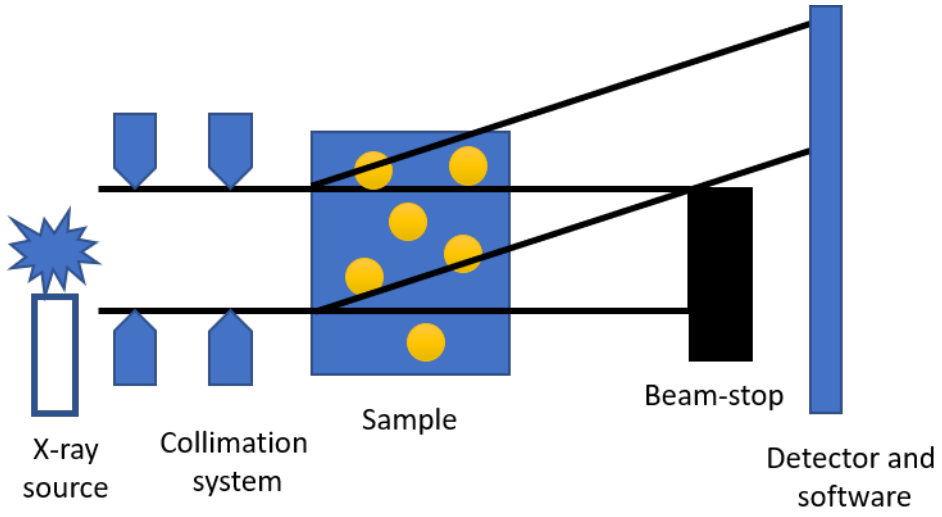

FIGURE 3.12: Standard set-up of X-ray equipment

solid state detectors (80).

SAXS analysis is usually the most fruitful when carried out at a synchrotron source, as the analysis of each sample is usually really quick (often from micro-seconds to 1 or 2 minutes), also, the q range that can be reached by SAXS synchrotron sources can be very low, therefore the shape and structure of larger particles can be analysed, which is not possible using laboratory SAXS (80).

Fitting SAXS data to determine the shape and size of populations of species present in a sample is not a trivial task; various analyses are often applied to the data. One such analysis the guinier fit which is based on the guinier Equation (3.22):

$$lnI(q) = lnI(0) - \frac{R_g^2 q^2}{3}, \tag{3.22}$$

where *I(q)* is the intensity of radiation detected by the detector, *I(0)* is the intensity when the value of q is zero (this is obtained by extrapolation), R_g is the radius of gyration, i.e. the distribution of components around the centre of gravity, essentially providing the size of the component in a sample.

Many other analyses, such as Porod, Zimm and Kratky can be carried out on the data to effectively characterize a sample. Note, Guinier analysis is only applicable when the system under analysis is such that the dispersed phase has minimum interactions between particles and there is minimal aggregation. The Guinier model assumes that the dispersed phase is spherical (81).

The broad distance range available in X-ray scattering also makes it an ideal tool for determining the specific liquid crystal structure. Due to their periodicity (liquid) crystalline structures show higher order Bragg peaks. The lamellar phase is expected to show peak ratios of 1: 1/2: 1/3: 1/4... whereas a hexagonal phase would show peak ratios of 1: $1/\sqrt{3}$: $1/\sqrt{4}$: $1/\sqrt{7}$: $1/\sqrt{9}$... (3).

The distance between alkyl chains (molecular ordering) can often be determined using wide angle X-ray scattering. This is particularly the case in rigid gel-type lamellar structures. In order to identify this peak at very low scattering distances ca. 3 to 6Å, it is essential to have very high resolution due to the low scattering intensity The use of Synchrotron radiation is often used in such experiments. A liquid crystalline system with a fluid alkyl region is characterised by a broad peak with a repeat distance of approximately 4.5 Å, whereas a gel phase type liquid crystal with a rigid alkyl region is characterised by a sharp peak at 4.2Å. A broad peak derived from the water present is also observed at 3.5 Å (82).

3.7.1 Equipment used

The SAXS experiments for this study were carried out in the BM28 beamline at ESRF - The European Synchrotron Radiation Facility. The equipment set-up was such that the sample to detector distance was 1.6 m and the tube was purged with Helium. A MAR CCD detector was used and silver behenate was used to calibrate the equipment as it's d-spacing is well known. All samples were background subtracted using deionised water. The SAXS data was collected over

a range between 0.0184 and 0.454 Å. The d-spacing of the Bragg peak identified by SAXS was analysed using the Bragg equation to determine the repeated d-spacing length. 80mm long Quartz-capillary tubes were used, with a 1.5mm outer diameter and 0.1 mm wall thickness. All samples were filled using a 1 ml syringe and a long needle.

3.8 Centrifugation

Centrifugation is a technique that exploits the difference in the bulk density of two different materials to separate them from one another. This is useful for phase identification in lyotropic systems as the phases present often have different bulk densities. It is, however, not possible to separate all phases, as some highly stable dispersions may remain dispersed despite the application of a centrifugal force.

The equipment used for the centrifugation experiments was the LUMIsizer by LUM. This allowed centrifugation speeds of up to 4000 RPM and temperature control between 4 and 60°C.

3.9 Rheology

Rheology is an experimental technique which exploits the 'internal friction' or viscosity to study the flow of materials. The types of materials generally studied are either liquids or soft solids - solids that respond with plastic flow upon the application of a force. When applying a force to a fluid, the force per unit area (F/a) required to produce a motion (also described by σ) is proportional to the velocity gradient (also known as the shear rate). The constant of proportionality is η (viscosity), so:

$$\sigma = \frac{\eta U}{d} \tag{3.23}$$

In the nineteenth century, Navier and Stokes developed a consistent three-dimensional theory to describe a Newtonian viscous liquid. In the case of a Newtonian fluid, flow continues as long as the stress is applied, so there is direct proportionality between the stress and strain rate. However, in the early twentieth century fluids with non-linear behaviours were discovered and models developed to describe their behaviour. Shear-thinning fluids show a reduction in the viscosity as the shear rate is increased (83). Newtonian behaviour is described by the following characteristics:

- The only stress generated in simple shear flow is the shear stress, σ. There is no difference between the normal stresses;
- The shear viscosity is independent of the shear rate;
- The viscosity is constant with respect to time of shearing and the stress in the liquid falls to zero after shearing is stopped (83).

Shear thinning fluids, also often known as pseudoplastic fluids reduce in viscosity as the shear rate is increased. For such materials, generally when the shear rates are very low, the viscosity remains constant as shear rate is increased. Again at very high shear rates, a similar behaviour is observed (83).

Shear-thickening fluids, also known as dilatant fluids display behaviour which show an increase in viscosity as the shear rate in increased. This usually occurs when the micro-structure of the material rearranges as such to increase the resistance to flow with an increase in shear rate. The shear thickening behaviour of fluids typically only spreads over a range of on decade of the flow rate. Most dilatant materials exhibit shear thinning behaviours at low flow rates (83).

Some Newtonian fluids display interesting time-dependent behaviours. Thixotropic materials show an increase in viscosity and shear stress over time as a constant

Table 3.2: An outline of the main types of geometry systems often equipped in rheoemeters.

Geometry	Details
Cone and plate	Useful for simple, single phase fluids. The angled cone gives an even shear field.
Parallel plate	Allows systems with suspended particles to be measured. The gap between plates can be varied to one most suitable for the size of the suspended particles.
Concentric cylinder	Suitable for low viscosity that cannot be constrained by the cone and plate or parallel plate geometries. There are multiple types, including: conical end geometries which are useful for a high range of shear rates and allows easy temperature control. The vane geometry is particularly useful for dispersions and to minimise wall slip effects.

shear rate is applied. This change may be reversible or irreversible. The opposite behaviour is known as reverse-thixotropy or rheopecty (84).

To observe this behaviour, a rheometer is usually utilised. Different geometeries can be employed on the rheometers, depending upon the system analysed. The main geometries and their applications are summaries in the table 3.2. The rheometer used for this project was the TA Discovery HR 2 rheometer, and a vane geometry was employed. Every experiment was carried out at $50°C$ a solvent trap was also employed to minimise water loss.

3.10 Materials

Commercial linear alkylbenzene sulphonic acid (HLAS) was provided by Procter and Gamble. The HLAS is composed of a number of different alkyl chain lengths and positional isomers (the benzene ring is substituted on any carbon other than the terminal carbons). A typical composition is shown in Table 3.3, which shows

Table 3.3: Exemplar composition of NaLAS isomers.(13)

Chain length	**% Alkyl chains**
C_{10}	14.7
C_{11}	34.2
C_{12}	31.9
C_{13}	19.2

the molar percentage of each alkyl chain length. It is manufactured using the Hydrogen Fluoride (HF) process, where n-Paraffins are broken down into n-mono-olefins and the n-mono-olefins are reacted with benzene in the presence of a HF catalyst to produce a linear alkylbenzene (LAB) and subsequently the LAB is sulphonated to leave HLAS. The main polymer used was a maleic-acrylic statistical co-polymer provided by P&G. It was provided in a 40% solution with a pH of 7.

HLAS was neutralised with analytical grade NaOH and water was added. The pH was measured and additions of NaOH/water/HLAS were made as necessary to leave a 45 wt% in water surfactant solution with a pH of 10.4. The polymer used (Procter and Gamble) was provided as a stock solution of 40 wt% in water with a pH of 7, the polymer structure is depicted in Figure 1. It is a maleic-acrylic poly-carboxylate polymer, where x = 0.7. For the NMR experiments, the neutralised surfactant was oven dried for 23 hours at 90 °C to remove water moisture, yielding a concentration of 97 wt% which was determined from mass loss measurements. This was consequently reconstituted with D_2O and the necessary amount of polymer solution was added to yield the concentrations needed for the samples. The samples were then stirred at 70 $^{\circ}C$ with a magnetic stirrer for one hour and placed in NMR tubes. The samples were analysed three days after initial preparation by NMR. In the case of analysis by centrifugation, SAXS or microscopy, the stock solution was not dried, rather diluted using poylmer solution to obtain the desired sample concentrations.

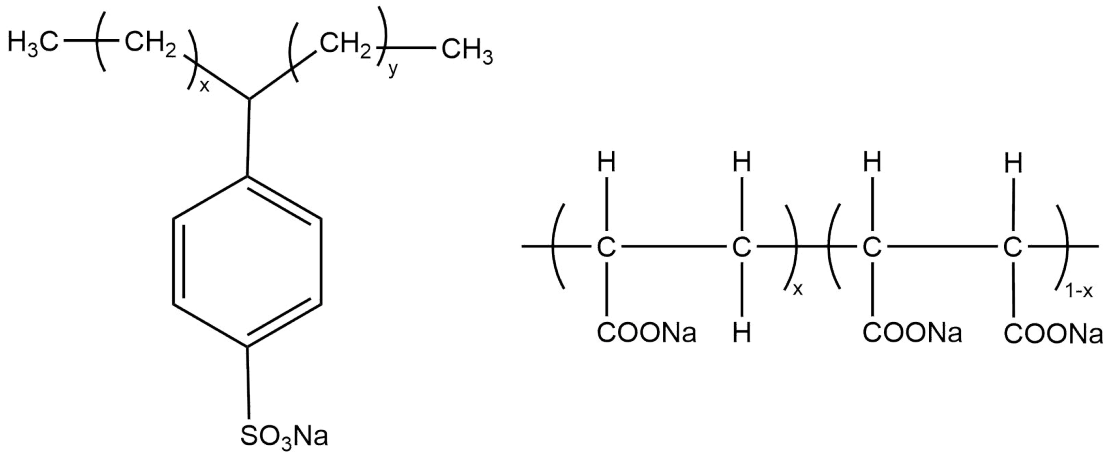

FIGURE 3.13: Structure of the surfactant used (left) and the polymer used (right).

Chapter 4

Phase and colloidal behaviour of NaLAS-polycarboxylate systems

4.1 Introduction and aims

As discussed in Chapter 2, the phase behaviour of NaLAS in water, as well as the influence of the addition of electrolyte has been the subject of various studies in literature. However, equally as important as understanding the phase behaviour is the influence of polymer on this behaviour - the literature of which is lacking. This knowledge is necessary because the surfactant is formulated in combination with polymer for both liquid and powdered detergent products, and an understanding of the interactions can help influence formulation decisions. This chapter will outline the influence of polycarboxylate polymers on surfactant self-assembly with respect to the phase and colloidal structure. A phase diagram will be constructed, from which some deductions of the phase behaviour of the system can be made, and NMR experiments will be carried out to determine the length scales of the self-assembling multilamellar vesicle structures.

4.2 Results

4.2.1 Construction of the phase diagram

The main techniques used in constructing the phase diagrams were cross polarised microscopy and centrifugation. Cross-polarised microscopy proved useful in determining isotropic-anistropic transitions. Centrifugation was also used to determine phase transitions of the surfactant-polymer system as different phases often had different bulk densities which could be differentiated by centrifugation.

4.2.2 Phase transitions determined using cross-polarised microscopy and centrifugation.

This phase transition were determined using centrifugation and cross-polarised microscopy. Each sample was prepared initially by weighing out the required masses of 45 wt% stock solution NaLAS, water and 40 wt% polymer necessary to produce the desired sample concentrations. Each sample was mixed thoroughly and left in a water bath overnight at 50°C.

A variety of samples containing a range of NaLAS and polymer concentrations were formulated. Initially a set of samples that started with 5 wt% NaLAS in water, the concentration of which increased in 5 wt% increments, and 2 wt% increments in polymer concentrations. As the phase transitions became clearer, when necessary extra samples were made at concentrations between 2 points to obtain a clearer idea of the transition point. The transition point represents the 'central' concentration between which 2 different transitions are seen. For example, if a single isotropic phase is is seen at 1 wt% polymer and a 2 phase region is seen at 3 wt% polymer, then the transition would be shown to occur at 2 wt%.

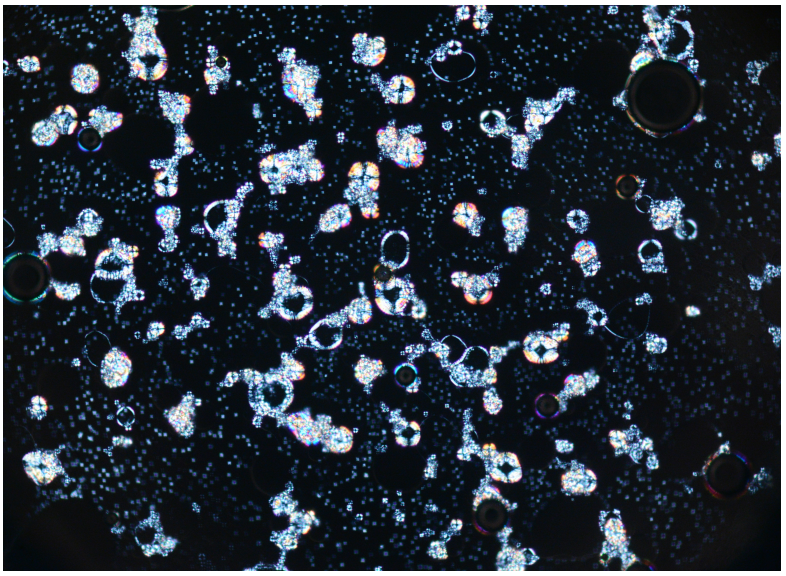

FIGURE 4.1: Microscopy image of 45 wt% NaLAS in water, at 50°C following a hour of centrifugation, showing birefringence dispersed in an optically isotropic background.

Phase identification of lamellar structures using optical polarising microscope is discussed further in Chapter 3. A small amount of sample was placed between 2 cover slips, which was then placed in a sealed hot stage. Each sample was then heated to 50 °C and left there for 10 minutes before analysis. Isotropic phases appear black between cross-polarisers, but upon phase transition from isotropic to isotropic + anisotropic, a small amount of birefringence appears, usually in the form of maltese crosses (these indicate the presence of multilamellar vesicles, as described further in Chapter 3). An exemplar microscopy image showing an isotropic system with an anisotropic dispersed phase is shown in Figure 4.1. Further data showing the phase trasitions is shown in appendix A.

As the concentration of either the surfactant or polymer was increased, the amount of birefringence was usually increased. In the case of the polymer addition, this is likely due polymer inducing surfactant head group aggregation, increasing the critical packing parameter. The polymer is charged, so the addition of this polymer increases the ionic strength of the system. This subsequently dehydrated the surfactant head-groups as a result of the decrease in the Debye length. This

reduces repulsive forces between micelles and they subsequently aggregate, and lamellar structures are induced. For NaLAS in water, micellar and lamellar structures are known to coexist for a wide concentration range(3). The lamellar phase has a different bulk density to the micellar phase, so both phases can be differentiated by centrifugation.

Each centrifuge tube was filled with 8 ml of sample. They samples in the centrifuge tubes were well mixed and heated to 50°C for 20 mins in a water bath. The LUMisizer centrifuge was heated for 50°C for 30 minutes. Following this, the samples were placed in the centrifuge for 2 hours 17 minutes at 4000 RPM. Then, each sample was photographed and the phases present were identified.

An example of the identification of 2-coexisting phases (one isotropic and one lamellar) is shown in Figure 4.2:

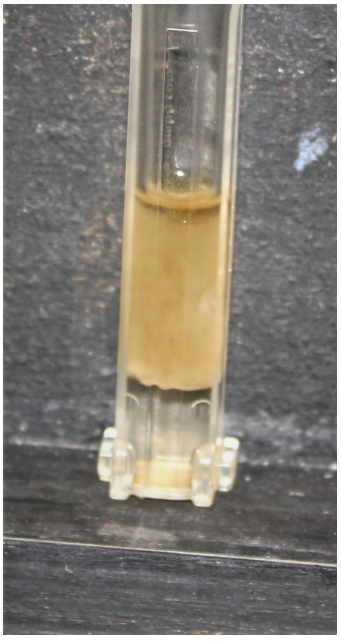

FIGURE 4.2: 45 wt% NaLAS and 2 wt% polymer in water, at 50°C following a hour of centrifugation, showing 2 different phases. A transparent high density phase which is the isotropic phase and a less dense, transluscent straw-coloured phase which is the lamellar phase.

An important thing to note is that phase identification by centrifugation is only effective in the case where the bulk density of 2 co-existing phases are different.

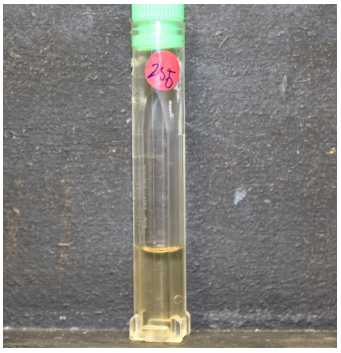

FIGURE 4.3: 25 wt% NaLAS water, at 50°C following a hour of centrifugation, showing 1 single isotropic phase.

FIGURE 4.4: Microscopy image of 20 wt% NaLAS water, at 50°C between cross polarisers.

There were many phases observed for the NaLAS-polycarboxylate polymer system. The first phase observed was a single isotropic phase. This showed no sedimentation/creaming during centrifugation, and was optically isotropic when observed between cross-polarisers. Figure 4.3 and 4.3 show how this appeared following centrifugation and between polarisers, respectively.

The second phase region observed was again optically isotropic when viewed between cross-polarisers. However, when centrifugation was carried out, there were 2 separate phases observed. An example of this 2-phase region following centrifugation is shown in Figure 4.6.

Following this, at higher surfactant concentrations, a second two-phase region was observed. There were two lamellar phases and one isotropic phase which

could be separated by centrifugation, and an example of this 2-phase region after centrifugation is shown in Figure 4.2.

FIGURE 4.5: 35 wt% NaLAS water and 8 wt% polymer at 50°C following a hour of centrifugation, showing 2 lamellar phases and an isotropic phase.

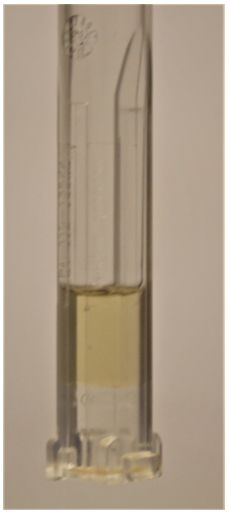

FIGURE 4.6: 25 wt% NaLAS water and 2 wt% polymer at 50°C following a hour of centrifugation, showing the 2 isotropic phases.

Finally, a region in which 2 observed lamellar phases of different bulk densities which co-existed with the micellar region was also observed. An example of this 2-phase region after centrifugation is shown in Figure 4.5. This transition from isotropic to lamellar could also be observed using polarised optical microscopy.

So, a phase diagram can be constructed by compiling the centrifugation data and microscopy data. This is shown in Figure 4.7.

The phase diagram presented in Figure 4.7 shows that in the absence of polymer, a single isotropic micellar phase, L_1, is present at concentrations lower than 35 wt% NaLAS, which is shown in Figure 2 as the L_1 region and the phase optically looks either like a transparent clear or straw coloured transluscent fluid/gel. At 35 wt% NaLAS and higher, a two-phase region of coexisting micellar and lamellar phases is present, the L_1 + L_α region; this is in agreement with reports by Richards(2) and Stewart(13).

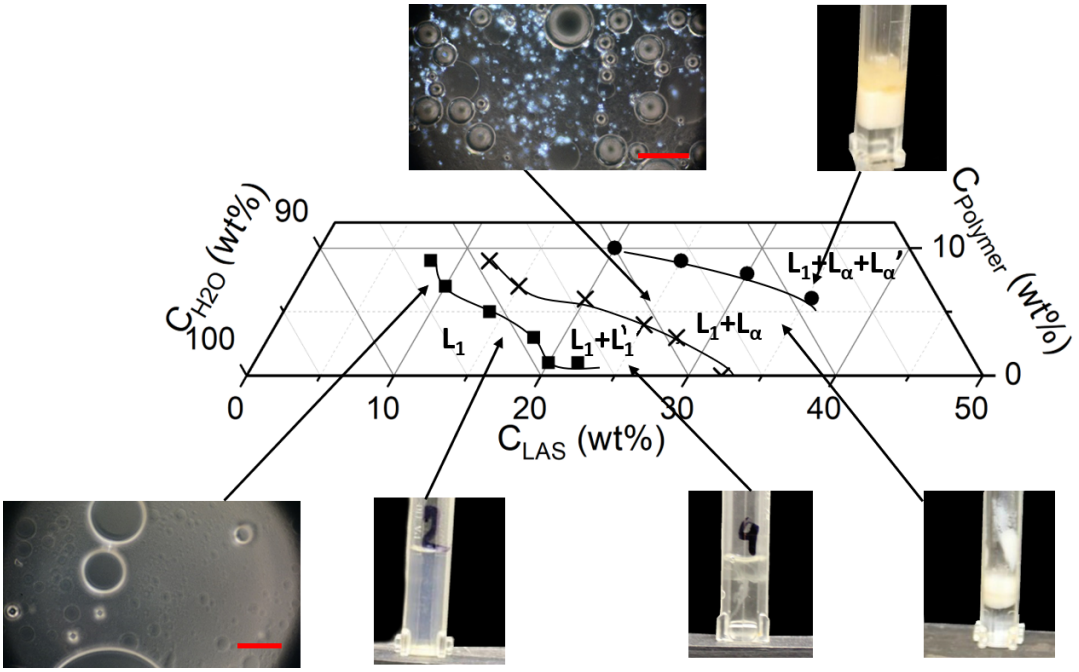

FIGURE 4.7: Ternary phase diagram of the NaLAS-polycarboxylate polymer-water system at 50 °C; the phase transitions were determined by centrifugation and cross-polarised microscopy. L_1 represents the low density lamellar phase, L_1' is the high density isotropic phase, L_α is the high density lamellar phase and L_α' is the low density lamellar phase.

In the micellar regime, as the concentration of polymer s increased, a two-phase regime is eventually observed, the L_1+ L_1' region, neither phase is birefringent. This implies that the addition of the polymer initiates phase separation.

Similar behaviour has been observed in other many other surfactant-polymer systems, such as PVP poylmer/SDS surfactant mixtures(85) and Triton X-405 surfactant/ D-glucopyranose polymer mixtures(86). The presence of the polymer in the micellar solution (in conditions where the micelles and polymer have the same charge) results in the negative adsorption (desorption) of the polymer on the surface of the micelle. This negative adsorption causes an osmotic pressure potential and once the micelles are in close proximity to one another, they aggregate. This is an appropriate prediction as both the micelle and the polymer will both be negatively charged so it is reasonable to assume that a mixture of both components could result in depletion flocculation. This phenomenon results in phase separation with a surfactant-micelle-rich region and a polymer-rich region, as seen in the phase diagram as the L_1+ L_1' region. This is possibly the cause of this 2-phase region(87).

The 3 phase region shown in the phase diagram, described by $L_1 + L_\alpha + L_\alpha$', shows a lamellar phase which has a lower density of the lamellar texture dispersed in the isotropic medium at the top of the centrifuge tube compared the bottom phase looks slightly turbid and transluscent, whereas the denser phase is opaque. Therefore, the two different lamellar phases have a different bulk density, resulting from a different bulk packing. Furthermore, Figure 4.8 shows a cross-polarised

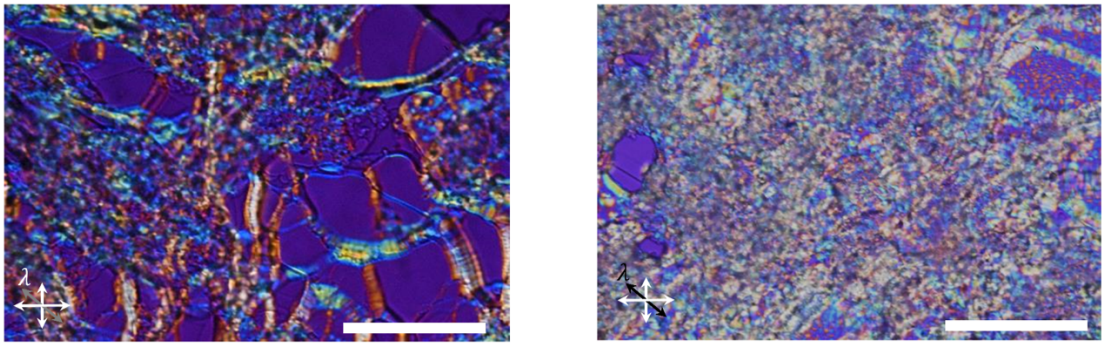

FIGURE 4.8: Cross-polarised microscopy images of the two lamellar phases viewed at 50°C with a full wave plate to emphasise birefringence. The image on the left shows the top, less dense lamellar phase (L_α); and the image on the right shows the bottom, denser lamellar phase (L_α')(3 5 wt% NaLAS, 8 wt% polymer). The scale bar in both images is 5 μm.

micrograph of the two lamellar phases viewed with a full wave plate. It can be seen that both lamellar phases are dispersed in an isotropic medium. However, the micrograph of the less dense phase shows fewer birefringent regions, showing the difference in microscopic packing of the lamellar phase between both phases. The L_α'(top) phase depicts a lower density of the lamellar phase per unit area compared to the L_α(bottom) phase. This is indicative of a difference in macroscopic packing of the phases, and this can be used to justify the difference in the density of the 2 phases. Safran(88) developed a model to describe such behaviour for systems containing a depleting polymer and lamellar structures composed of lipids, which can be used to describe the macroscopic phase separation observed in this system. Consider a multilamellar vesicle (MLV) in terms of its outer bilayer. The outer bilayer has an inner monolayer and an outer monolayer. There are two bilayers in close contact, separated by polymer in water. The outer monolayer of both MLVs are facing the polymer solution. This layout is shown in Figure 4.9. B depicts the polymer rich region between the 2 vesicles. There is a repulsive interaction between the surfactant head groups and the polymer, so the surfactant head groups will act to minimise their contact with the polymer solution. This is achieved by increasing the surfactant packing density. As the area of the head groups and number of surfactant molecules remain constant, phase separation occurs. This specifically occurs in the outer monolayer – there is condensation of surfactants because of the repulsive interactions between the polymer and surfactant. This phase separation is energetically favourable as it results in a lower-density surfactant region being exposed to the polymer-rich solution and this region will have a significantly higher interfacial tension relative to the surfactant-poor region. So, consequently there will be a Marangoni flow of surfactant monomers to reduce the interfacial tension in the high interfacial tension region, the flow of the surfactant monomer results from the high packing density monomers in the outer monomer in region B towards region A (as labelled in Figure 4.9).

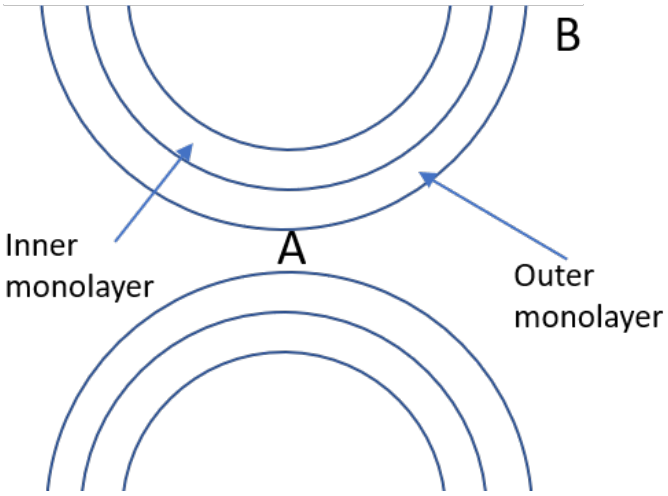

FIGURE 4.9: Schematic showing the outer bilayer of 2 MLVs prior to the addition of a depletive polymer.

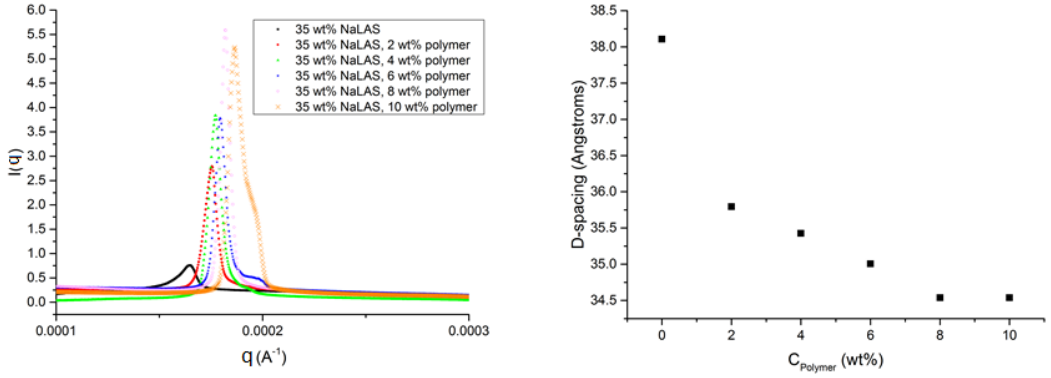

FIGURE 4.10: The d-spacing of the lamellar phase at 35 wt% at 50°C NaLAS as a function of polymer concentration determined using the Bragg equation from the SAXS experiments at 50°C and the raw intensity-q plots of the samples from which the d-spacing is determined.

4.2.3 SAXS

Following this, the nature of the region containing 2 lamellar phases was explored further using SAXS. All the samples (which were prepared in the same way as those analysed for the phase diagrams) were well mixed and were kept in a hot water bath at 50°C for 5 hours until measurement time, then they were placed in a 1.5mm diameter SAXS quartz capillary tube immediately before analysis. The samples were placed in a rack on the beamline and each sample was pre-heated for 5 minutes before X-ray exposure. The exposure time for each sample was 3

minutes (this was sufficient for the high intensity beamline X-ray radiation). Each sample was background subtracted with a deionised water filled tube.

An example of the calculation of the d-spacing when the Brakk peak is 2 $\mathring{A}$ is as follows:

$$q_{Bragg} = 2\mathring{A} \tag{4.1}$$

$$d = \frac{2\pi}{q_{Bragg}} \tag{4.2}$$

$$d = \frac{2\pi}{2} \tag{4.3}$$

$$d = 3.14\mathring{A} \tag{4.4}$$

This could be used to give an idea of whether the lamellar phases of different densities result from lateral phase separation. Samples containing 35 wt% NaLAS with increasing concentrations of polymer were considered and the changes in the changes in the lamellar d-spacing were determined. These results are shown in Figure 4.10. Clearly, a decrease in d-spacing as a function of polymer concentration is observed. The chain lengths of the surfactant doesn't change, so this change is due to a reduction of the water layer thickness. There are 2 potential causes of this phenomena. Firstly, dehydration effects should be considered. The polymer is ionic, therefore, it can screen the charges of the surfactant head groups. As a result, the repulsive forces between headgroups of parallel lamellar layers are reduced, resulting in the water layer thickness reducing. Secondly, depletion flocculation effects resulting from the addition of the polymer. The negatively charged polymer (at pH 7) and negatively charged surfactant can interact in a manner resulting an attractive depletive force forcing the parallel bilayers to come closer together. This is because the negatively charged polymer repels the negatively charged surfactant head groups. This results in an area depleted in polymer

surrounding the surfactant headgroups. This hence results in an osmotic potential difference which forces water out of the inter-bilayer spacing.

4.2.4 NMR analysis of the lamellar phase

Following this, an attempt was made at sizing the MLVs, and to observe the changes in size as a function of polymer concentration. The method used to attempt to achieve this is published by Medronho(89). By dispersing the NaLAS in D_2O and running a basic deuterium NMR spectra, the T_2 relaxation time and quadrupolar splittings:

$$\Delta\nu_Q = \frac{3}{4}|\chi S|, \tag{4.5}$$

Where $\Delta\nu_Q$ is the quadrupolar splitting in the lamellar phase, χ is the quadrupolar splitting and s is the order parameter which can be described by:

$$s = \frac{3cos^2\theta - 1}{2}. \tag{4.6}$$

θ is the angle between the liquid-crystal molecular axis and the local director (which is the 'preferred direction' in a volume element of a liquid crystal sample, also representing its local optical axis). The ^2H line width is much higher in the MLV state than the micellar phase. This shows that the transverse relaxation is mainly due to the slow motion and that is sufficient to consider the zero-frequency spectral density of the slow motion, $j_s(0)$ in the expression for T_2 so that:

$$\frac{1}{T_2} = \frac{9\pi^2}{40}|\chi S|^2 J_s(0), \tag{4.7}$$

If the slow reorientation of water is due to reorientation is due to diffusion within a spherical shell of radius R, then:

$$j_s(0) = \frac{R^2}{3D}, \tag{4.8}$$

where D is the diffusion coefficient. Combining the above Equations gives:

$$\frac{1}{T_{2,n}} = \frac{2\Delta\nu_Q^2 d^2}{15D} n^2 + \frac{1}{T_{2,inhom}}. \tag{4.9}$$

The constant $1/T_{2,inhom}$ takes into account the effect of inhomogeneity of the magnetic field on the line shape, and is equal to the half-width at half maximum in this case of the surfactant in the micellar phase. d is the lamellar d-spacing and n is the number of layers of the MLV.

Before the NMR experiments were carried out, each sample in D_2O was observed between cross-polarisers to gauge an understanding of what to expect in terms of the phase behaviour. These images are shown in Figure 4.11. From this, it can be seen that at 35 wt% NaLAS in water, a small amount of birefringence is seen. As the concentration of polymer is increased, the density of biregringence increases as a function of polymer concentration. As previously stated, this is likely due to the combination of the flocculating and charged nature of the polymer transforming micelles into lamellar structures.

The model proposed by Medronho (89) was validated on a non-ionic surfactant system ($C_{12}E_4$) 40 wt% in D_2O which exhibited the lamellar phase. This sample was sheared at increasing rates between 10 and 40 s^{-1} and simultaneous NMR measurements were taken. From this NMR data, the MLV size as a function for shear rate was calculated. This data was validated using rheo-SALS, and the results of both techniques were consistent. In the system analysed by Medrobho, the lamellar sheets were all converted into multilamellar vesicles upon the addition

of shear, the the quadrupolar splitting was determined by collecting spectra prior to the application of shear. This is the only case in which the model has been applied to a surfactant system (to our knowledge).

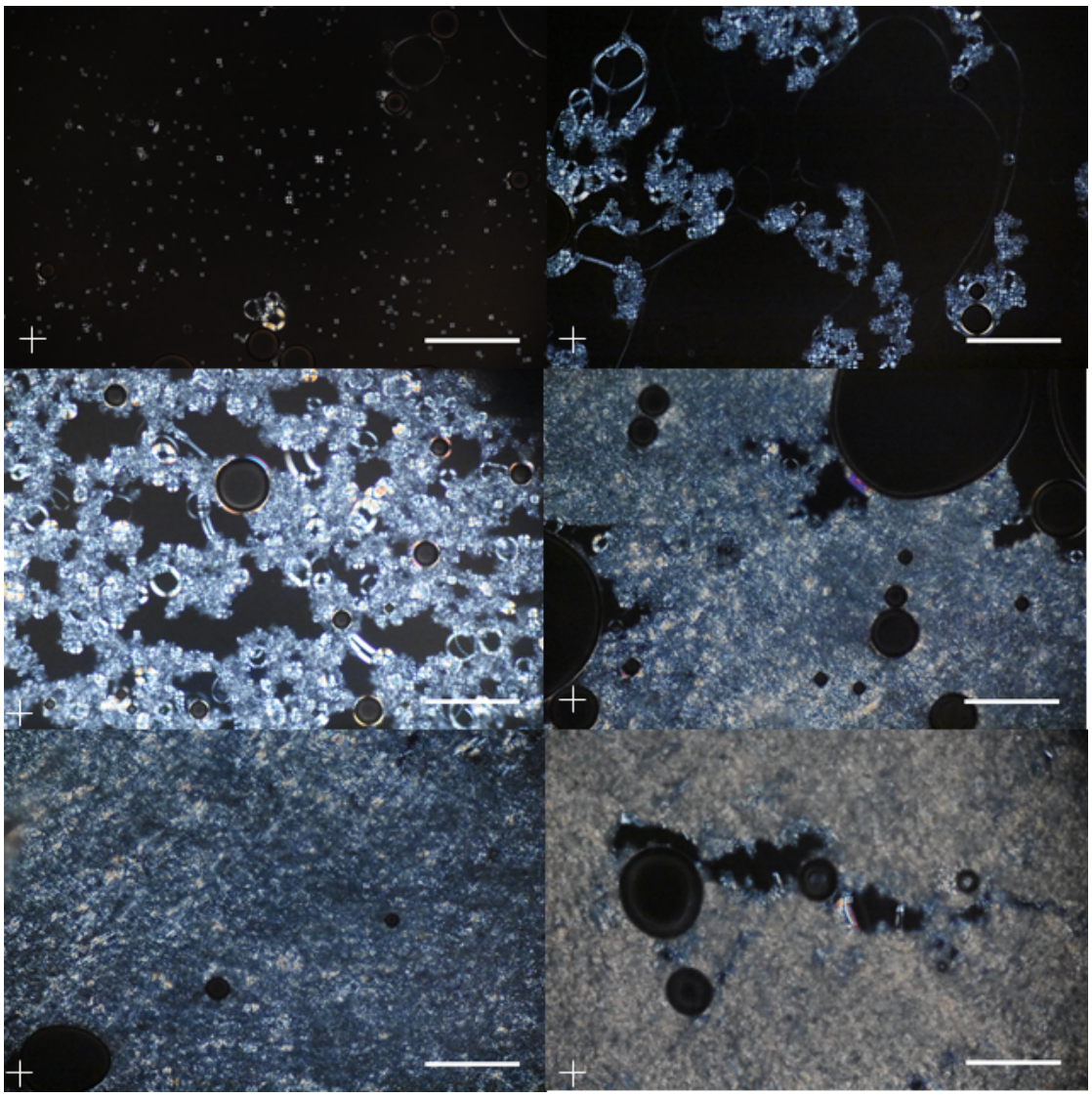

FIGURE 4.11: Cross-polarised images at 50 °C, from top left to bottom right: 35 wt% NaLAS in D_2O; 35 wt% NaLAS, 2 wt% polymer in D_2O; 35 wt% NaLAS, 4 wt% polymer in D_2O; 35 wt% NaLAS, 6 wt% polymer in D_2O; 35 wt% NaLAS, 8 wt% polymer in D_2O; 35 wt% NaLAS, 10 wt% polymer in D_2O. The scale bar represents 5μm.

So following the observation of the phase behaviour of the 35 wt% NaLAS in water system with increasing concentrations of polymer, the NMR experiments were carried out. As the 45 wt% was in water, the samples were oven dried at 80°C for 12 hours to remove the majority of the water and the samples were

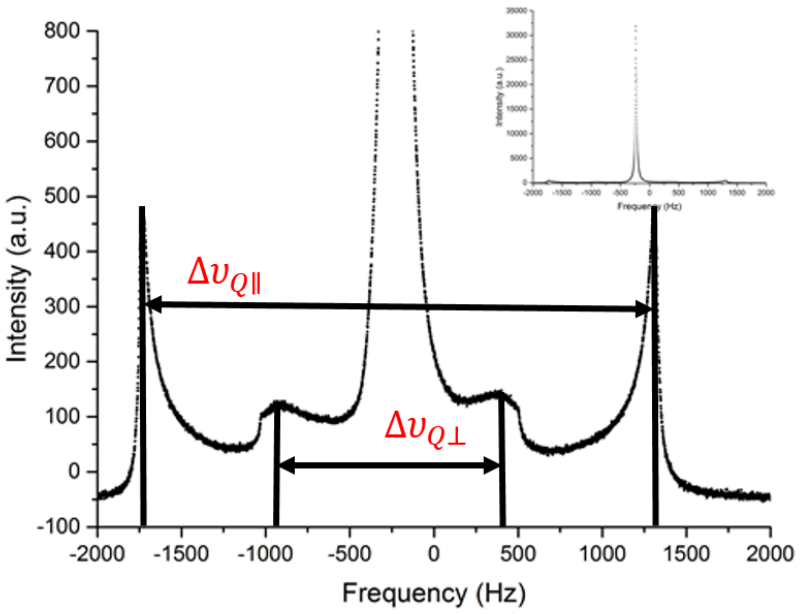

FIGURE 4.12: NMR spectra of 35 wt% NaLAS and 6 wt % polymer at 50°C, after the sample in the NMR tubes was equilibrated with the magnetic field for 40 minutes. The inset shows the spectra zoomed out and the main figure shows the spectra zoomed in to show details of the quadrupolar splitting and the central isotropic peak.

reconstituted with D_2O and the stock 40 wt% polymer solution to the desired concentrations of NaLAS and polymer for the samples. Each sample was kept in an NMR tube at 50°C (in a hot water bath) for 5 days before the NMR experiment. Then before analysis, each sample was kept in the NMR machine for half an hour at 50°C before running the spectra.

Typical spectra obtained are shown in Figure 4.12. From this spectra, it can be seen that there is a central isotropic peak. This central peak arises from the quadrupolar interactions of the D_2O with electric field gradients which are completely averaged out. A splitting pattern phase is seen in the case of lamellar structures arising from the anisotropic nature of the surfactant molecules which imposes anisotropy in the motions of the nearby D_2O. This manifests itself as quadrupolar splitting as the anistropic quadrupolar interactions of this D_2O does not completely average itself out and the magnitude of the splitting depends upon

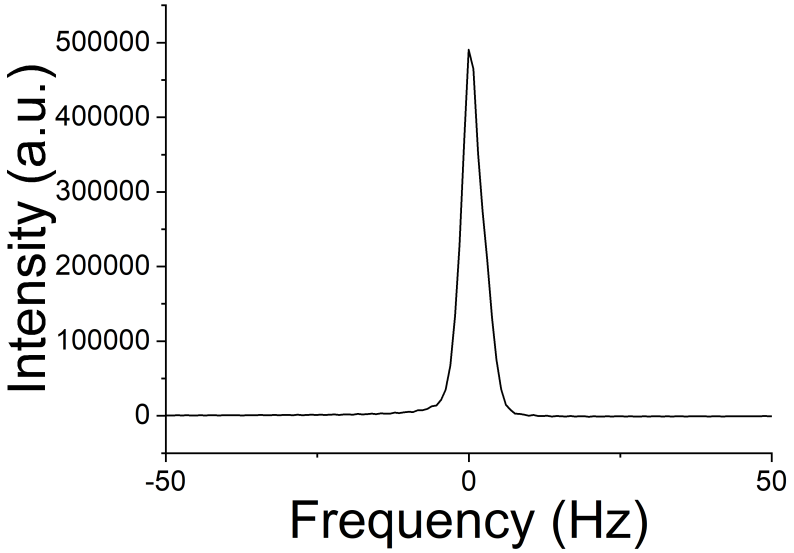

FIGURE 4.13: ^{2}H NMR spectra of 22wt% NaLAS at 50°C.

the amount of time averaging of the electric field gradients. Up to 4 maxima are observed in the spectra when a lamellar phase is present. The distance between one pair can be related to perpendicular order parameter, and the distance between the other pair can be related to the parallel order parameter. Both pairs of the peaks can be seen in Figure 4.12.

In the central peak, there will be a contribution of isotropic water associated with the micelles, water in the bulk as well as water in the multilamellar vesicles. So, a separate experiment was ran on multiple micelle solutions (12, 18 and 24 wt% in D_2O) which all exhibited a spectrum with a single isotropic peak as seen in Figure 4.13. This contribution would is accounted for in the subsequent analysis.

Following this, the diffusion coefficient could be determined corresponding to the central isotropic peak. This was done using a PGSTE method explained further in Chapter 3.

The isotropic peak was then fitted to a lorentzian curve and the half-width at the half maximum of the fitted lorentzian could be used to directly determine

the T_2 relaxation time with the following relationship:

$$\frac{1}{T_2} = \pi\nu_{\frac{1}{2}}. \tag{4.10}$$

So, then the size of the vesicles could be determined using the following model derived by Medronho(89) (the derivation is shown in Chapter 2):

$$R_{MLV} = \sqrt{\frac{15D}{2T_2\Delta\nu_Q^2}} \tag{4.11}$$

The spectra for 35wt% NaLAS with 0,2,4,6 and 8 wt% polymer is shown in Figure 4.14. Figure 4.15 shows the changes in the quadrupolar splitting, half width at half maximum for the isotropic peak, diffusion coefficient of the isotropic peak and the calculated MLV size as a function of polymer concentration. The rest of the raw data for diffusion coefficients and the Lorentzian fits for the central peak is shown in the appendix.

The increase in quadrupolar splitting can be explained by the increase in the ionic strength as a result of the polymer addition, which results in the increase in surface curvature and an increased surface curvature results in an increased order parameter as shown in Equation 4.6. This is because the order parameter is directly proportional to orientational angle. When lamellar sheet is perfectly flat, this angle is zero. As the surface curvature increases this angle increases.

The half width at half maximum of the isotropic peak increases as a function of polymer concentration, showing that the T_2 relaxation time decreases as a function of polymer concentration this is intuitive as the d-spacing decreases as a function of a polymer concentration, the thickness of the water layers in the vesicle decreases, so the mobility of the water is reduced and hence the T_2 relaxation time is also reduced. In accordance to Fick's law, as the thickness of the distance over which a species is diffusing is decreased, the rate of diffusion increases.

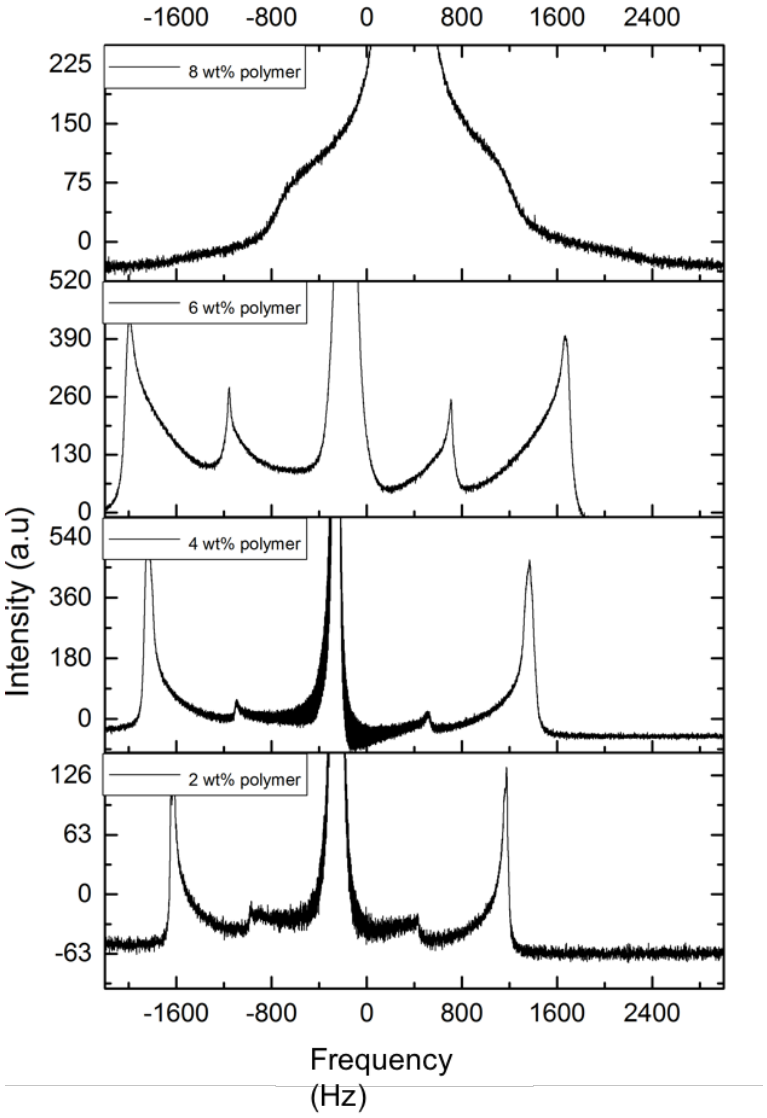

FIGURE 4.14: NMR spectra of 35 wt% NaLAS and 2,4,6 and 8 wt % polymer at 50°C, after the sample in the NMR tubes was left in the machine at 50°C for 40 minutes so the temperature of the sample can reach equilibrium with the NMR machine. All spectra are zoomed in.

However, due to the thin water layer thickness, confinement effects need to also be considered. In an unconfined system, the diffusion coefficient would increase with the size of the bilayer in accordance to Fick's law of diffusion. Farimani and Aluru(90) have reported that when considering water confined in channels, as the channel thickness increases from 10 to 25 A, the diffusion coefficient increases, but as the channel thickness increases from 25 to 50 A, the diffusion coefficient decreases. Poulos stated that for NaLAS, the bilayer thickness is approximately

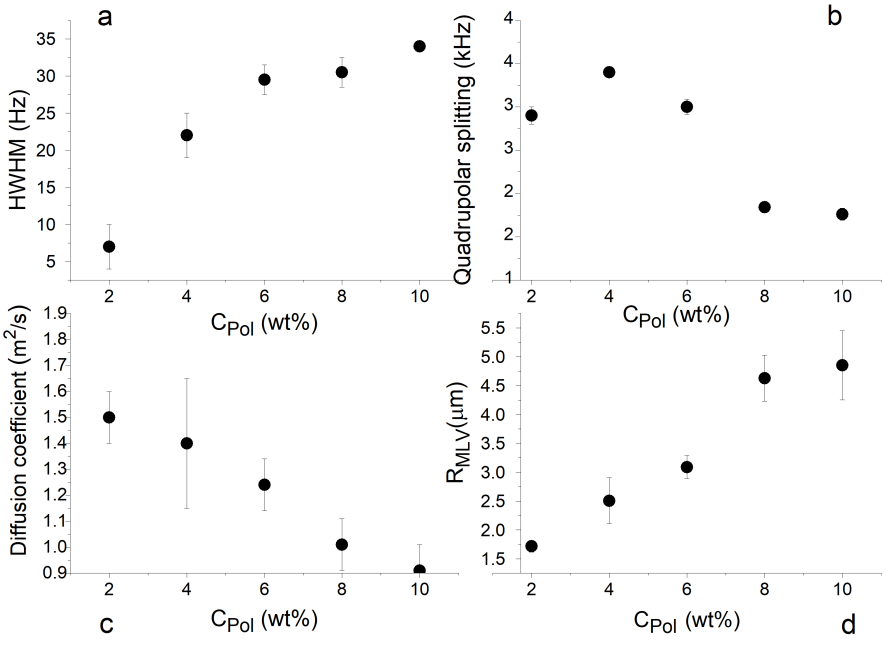

FIGURE 4.15: Data from NMR, all at 35 wt% NaLAS in water with at varying polymer concentrations, at 50°C. a) shows the variation of the half width at half maximum of the fitted lorentzians of the central isotropic peaks, with the HWHM (half-width at half maximum) of the micellar solution of 3Hz subtracted, b) shows the variation of the average quadrupolar splitting as a function of polymer concentration, c) shows the variation of diffusion coefficient corresponding to the isotropic peak as a function of polymer concentration and finally d) shows the calculated MLV (multilamellar vesicle) radius as a function of polymer concentration determined by using the data in graphs a to c. The error bars are based on standard deviations of repeated data sets.

18 - 22A, so subtracting that from the *d*-spacing, the water thickness decreases from about 19A at 2 wt% polymer to 14A and 10 wt% polymer. So, comparing the trend in *d*-spacing to the study by Farimani and Aluru (90), and relating this to the change in diffusion coefficient, an increase in diffusion coefficient would be expected. However, the NaLAS-polymer-water system is significantly more complicated than water confined in between a channel. There are additional surface, van-der-waals and electrostatic interactions which may come into effect when considering the diffusion of the water in the bilayer.

A second factor that needs to be considered is that an attempt was made to fit the diffusion coefficient data to multiple exponentials when determining D

using the Stejskal-Tanner equation, however, the best fit was observed from a single fit. Now, despite this, there is likely to be multiple contributions to the diffusion coefficient. Both the bulk water, and the water confined in the bilayers. As the polymer concentration increases, the density of the lamellar phase increases. Therefore, the contribution of the water from the interlamellar water will be higher at higher polymer concentrations than at lower concentrations. When considering the fact that the bulk diffusion coefficient of water is significantly higher than the diffusion coefficient of water in the bilayers, it can be seen that the weighted average of these diffusion coefficients will be more influenced by the inter-bilayer water at higher polymer concentrations.

Finally, the trend in MLV size as a function of polymer concentration is interesting indeed! This trend can be explained by depletion flocculation, just like the d-spacing trend.

Consider surfactant in water, where the surfactant self-assemble into MLVs. When the polymer is added to the system, it is energetically unfavourable for the polymer coils to approach the vesicle surface. This leads to a region close to the vesicle surface being relatively low in polymer concentration, it can be said the polymer has negatively adsorbed on the MLV surface (91; 92). In a system containing multilamellar vesicles, the addition of a polymer which has a radius of gyration equal to or greater than the length of the interlamellar water thickness, it will be energetically unfavourable for the polymer chains to remain confined between the lamellar layers. Hence, the polymer chains are expelled out of the vesicles. This then results in an osmotic pressure gradient and therefore an increase in the Gibbs free energy of the system. Therefore, to reduce the Gibbs free energy of the system, there is a compression of the vesicles caused by reducing the interlamellar water layer thickness as the water is forced out of the vesicle, this decrease in water layer thickness may perhaps be the cause of the decrease in d-spacing as a function of polymer concentration as the water follows the osmotic

pressure gradient. The polymer added allows depletion flocculation of the system. This, in result, increases the vesicle size by fusion. The polymer is now situated outside the vesicles. The polymer has the same charge as the head groups of the surfactant, which results in a layer depleted of polymer surrounding the vesicles. If 2 of these MLVs with a depleted layer come into close contact with one another due to Brownian motion, the depletion layers overlap due to Brownian motion, resulting in a region between the vesicles being lower in polymer concentration than in the bulk, so there is an osmotic gradient causing a net attractive force between the vesicles. As a result, flocculation of the vesicles occurs. Following this flocculation, the vesicles can fuse by the following process described by Cullis(93):

- Aggregation of the vesicles leading to a close approach of the outer bilayers of two opposite vesicles.
- Formation of highly dynamic intermediate structures between the outer bilayers of two opposed vesicles.
- Rupture of the intermediate non-bilayer structures either back into the starting structure or merging of the vesicles into a larger fused vesicle.

4.2.5 Phase behaviour of NaLAS - polycarboylate polymer which is pH adjusted

The phase diagram for the NaLAS with the polycarboxylate polymer at a low pH of 3.5 is shown in Figure 4.16. Clearly, the adjustment of the pH has a very profound effect on the phase behaviour. Now, there is only one phase transition in this system, this is likely because the extreme pH level as a result of the addition of sodium hydroxide acts to screen the charges of the polymer chains and the surfactant headgroups. Therefore, there is no negative adsorption of the polymer on the surface of the surfactant micelles, and hence no phase separation into a

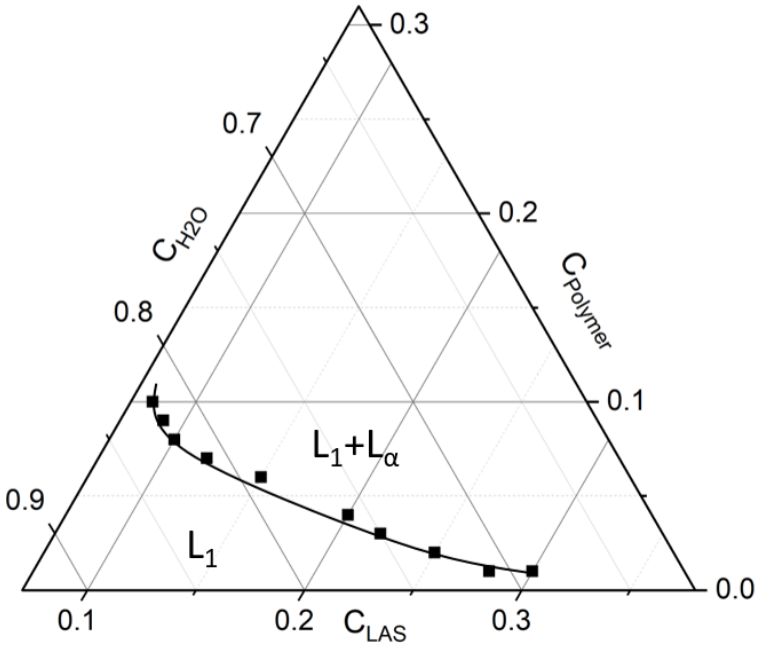

FIGURE 4.16: Ternary phase diagram of the NaLAS-polycarboxylate polymer-water system at 50 °C, with the stock polymer solution at a pH of 4; the phase transitions were determined by centrifugation and cross-polarised microscopy. L_1 represents the low density lamellar phase, L_1' is the high density isotropic phase, L_α is the high density lamellar phase and L_α' is the low density lamellar phase.

surfactant rich and a polymer rich region. Whereas, this phase separation is seen in the high pH polymer system. It instead behaves in a way similar to what would be expected by the addition electrolyte salts, as reported by Stuart (94) and (3). So, at low pH, the second isotropic phase is not observed. The phase transitions for this phase diagram are presented in the appendix.

4.3 Conclusions

The influence of adding a polycarboxylate polymer to a NaLAS-water system was determined by constructing a phase diagram. It was observed that various

types of behaviours were observed depending upon the region of the phase diagram being observed. At low surfactant concentrations, phase separation into two isotropic phases with different densities, likely a result of depletion flocculation, were observed. At higher surfactant concentrations, polymer also causes the phase separation of the lamellar phase into a high surfactant and low surfactant density, as well as the formation of different lamellar phases that have different d-spacings. When in the lamellar phase, the addition of polymer results in the increase in multilamellar vesicle size, as modelled by NMR, perhaps resulting from vesicle fusion. The NMR technique has successfully allowed the sizing of vesicles, the trends in which may be due to the depletion flocculation phenomena.

Chapter 5

Structural characterisation in saturated sodium sulphate solution conditions

5.1 Aims

- To quantify the domain sizes of the continuous isotropic phase of a NaLAS-polymer-saturated salt solution system using PGSTE NMR.
- To understand the influence of polymer on these domain sizes.
- To relate the domain sizes to the the observed phase behaviour.

5.1.1 Introduction

The previous chapter charactersised the phase behaviour of NaLAS in water when formulated with the addition of polycarboxylate polymer. However, in industrial applications, NaLAS is always formulated in very high ionic strength conditions,

resulting from the addition of sodium sulphate. James Stewart's work (95) as well as the work by Sein et al (3) has shown that the addition of sodium sulphate has significant impacts on the phase behaviour on the system. The salt acts to screen the head groups of the surfactants are screened, resulting in an increase in the packing parameter of the surfactant, consequently changing the phase behaviour of the system significantly. Therefore, the influence of polymer in a system may be significantly different in high ionic conditions, and understanding the influence of polymer on the phase and colloidal behaviour in high ionic strength conditions could be useful for helping with formulation decisions. In the previous chapter, a method based on the quadrupolar splitting of the lamellar phase, as well as T_2 relaxation time and diffusion coefficient within the water was used to size the vesicles. The problem with this method is that in very high ionic conditions, all the lamellar sheets have been transformed into lamellar sheets, so the quadrupolar splitting cannot be detected using NMR. Therefore, for this chapter, a different method will be used to characterise the microgeometry of the system - that is modelling the system as a porous system where there is a high density of vesicles, between which water diffuses. The spaces between the vesicles will be modelled as pores.

The theoretical background to PGSTE-NMR measurements are discussed further in Chapter 3, and the pulse sequence is shown in Figure 5.1. In the case where the characteristic diffusion length $\sqrt{DT}$ of the fluid in a porous system is significantly smaller that the obstruction length, i.e. the characteristic pore length, most nuclei will not encounter a boundary during their motion. Only nuclei that began close to the boundary surface within a surface layer of width $\sqrt{DT}$ close to the boundary walls exhibit restricted diffusion and the volume fraction of the nuclei which are affected is $S\sqrt{DT}/V$. S is the surface area of the walls and V is the

total area of the domain So, the diffusion can be described as follows (96):

$$\frac{ADC_0}{D} \simeq 1 - c_0\sqrt{DT}\frac{S}{V}, \tag{5.1}$$

where ADC_0 is the time-dependent diffusion coefficient. c_0 is defined as:

$$c_0 = \frac{4}{3\sqrt{\pi}}\frac{\prec (t_2 - t_1)^{3/2} \succ}{\prec (t_2 - t_1) \succ} \cdot \left(\frac{1}{s}\int_{\delta\Omega} dr(e \cdot n_r)^2\right). \tag{5.2}$$

The temporal average $\prec \cdots \succ$ takes into account the temporal profile, f(t). The final factor of the equation takes into account the scalar product between the gradient direction e and the normal vector n_r, all squared and integrated over the boundary $\delta\Omega$. Therefore, this integral is dependent upon the geometry of the boundary. In a PGSTE experiment, where the value of Δ is very low, the ratio of the 2 temporal averages becomes zero, and Equation 5.2 becomes:

$$\frac{ADC_0}{D} \simeq \left(1 - \frac{4}{9\pi}\sqrt{D\Delta} \cdot \frac{s}{v}\right). \tag{5.3}$$

When the value of Δ is relatively low, Equation 5.3 can be used to model a porous system with a confined liquid that has a low characteristic length relative to the obstruction length. However, at higher values of Δ, the value of $\frac{D}{D_0}$ reaches a constant value, which is dictated by the tortuosity of the system, τ(97):

$$\tau = \lim_{\Delta\to\infty} \frac{D_0}{D(\Delta)}. \tag{5.4}$$

The tortuosity reflects how the microstructure and surface exchange affect diffusion at long times. ADC_0 in Equation 5.3 can be related to D and D_0 as follows:

$$D = D_0\left(1 - \frac{4}{9\pi}\sqrt{D\Delta} \cdot \frac{s}{v}\right). \tag{5.5}$$

Therefore, by carrying out a series of PGSTE experiments and varying Δ, both the surface area to volume ratio (S/V ratio) of the pores and τ can be determined for a porous system. This can be done by varying the value of Δ from very low values to ensure that only a surface level of water experiences restricted diffusion, as well as higher values of Δ to determine the toruosity, τ. This data can be fitted to Equations 5.4 and 5.5 to determine S/V and τ.

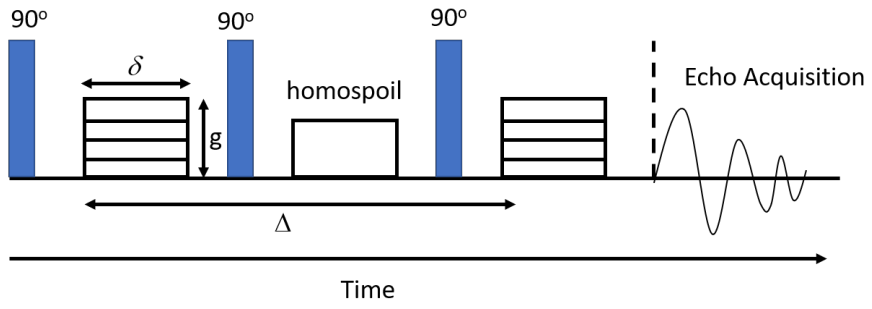

FIGURE 5.1: The PGSTE NMR pulse sequence used to determine the diffusion coefficient at different observation times, Δ.

This method has previously been carried out for a NaLAS-sodium sulphate-water system to determine the changes in characteristic pore size as a function of drying time of a droplet of the system. A decrease in characteristic pore size as a function of decreasing moisture content was observed. There were 2 effects that led to this. As the water content was reduced, residual moisture migrated to smaller pores due to preferential wetting effects. In addition, as the detergent mix dried, the polymer, NaLAS and sodium sulphate came out of solution and crystallised on the edge of the pores, resulting in the pore size decreasing. This technique was validated with S/V measurements using T_2 experiments. This shows that this is a suitable technique for characteristic pore size determination (98).

In this work, this technique will be used for a similar system to the system studied by Griffith, but the concentrations will be slightly different, and the influence of polymer concentration will be probed. The use of this technique is suitable for this system as pore size characterisation is a suitable way of characterising the

pore size and an understanding how the pore size changes as a function of polymer can demonstrate how the polymer influences the micro-structure of the system, providing details on how the polymer interacts with the system.

5.2 Introducing the phase behaviour of the system

The first step necessary to understand the phase behavior of the system required the formation of a phase diagram, this is shown in Figure 5.3. It shows the phase behaviour of NaLAS-polymer in saturated sodium sulphate with increasing concentrations of polymer. There is only one phase boundary, which shows in the absence of polymer, the surfactant systems studied exhibit 2 phases, optically isotropic and lamellar. As the polymer is added, a phase transition occurs which results in a decrease in the ratio of the isotropic phase to lamellar phase, until a single lamellar phase exists. The concentration of polycarboxylate polymer necessary for this transition decreases as the surfactant concentration increases.

This phase transition was determined using centrifugation. Each sample was prepared by weighing out the desired masses of 45 wt% stock solution NaLAS, water and 40 wt% polymer necessary to produce the desired concentration. Each sample was mixed thoroughly and left in a water bath over night. Then, each centrifuge tube was filled with 8 ml of sample. They were well mixed and heated to 50°C for 20 mins in a water bath. The LUMisizer centrifuge was heated for 50°C for 30 minutes. Following this, the samples were placed in the centrifuge for 2 hours 17 minutes at 4000 RPM. Then, each sample was photographed and the phases present were identified.

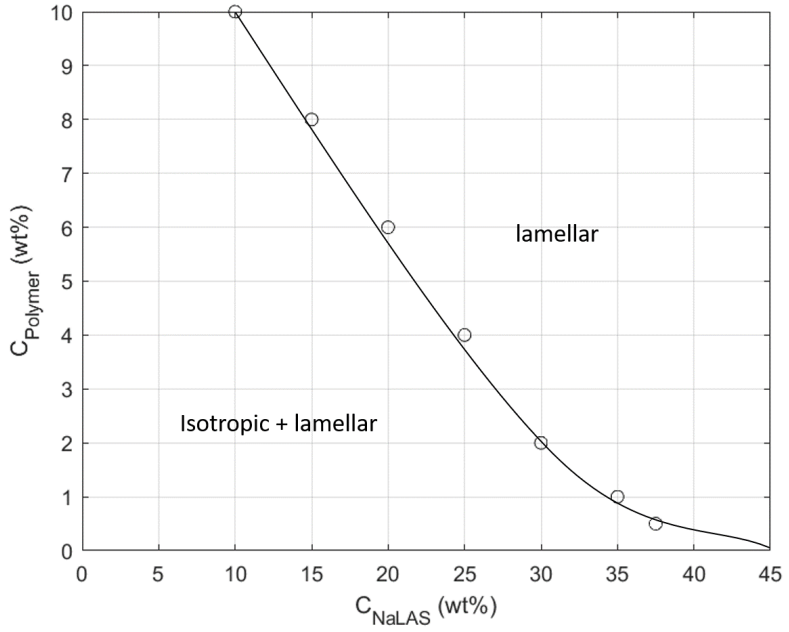

FIGURE 5.2: NaLAS-polycarboxylate polymer phase diagram in saturated sodium sulphate solution at 50°C, the phase transitions were determined by centrifugation.

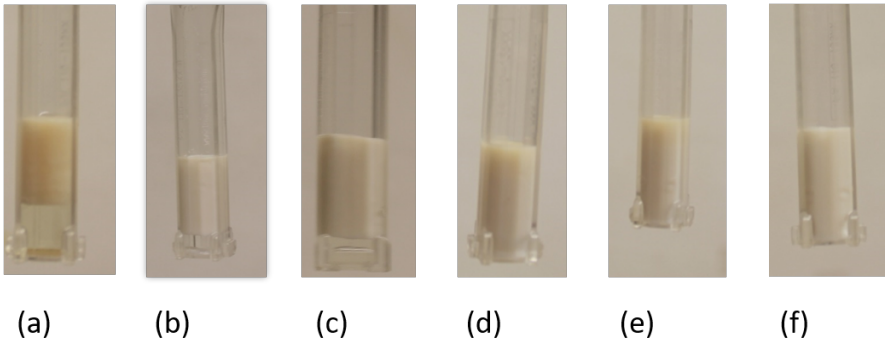

FIGURE 5.3: 20 wt% NaLAS in saturated sodium sulphate solution at 50°C with different polycarboxylate polymer concentrations: a) 0 wt%, b) 2 wt%, c) 4 wt%, d) 6 wt%, e)8 wt% and f) 10 wt%. This is following 2 hour 17 minutes of centrifugation of sample at 4000 RPM at 50°C.

Figure 5.3 shows the samples following centrifugation of 20 wt% NaLAS in water for a range of polymer concentrations, the remaining phase transitions are presented in the Appendix.

Consider the lamellar phase, which consists of MLVs, with water separating vesicles or aggregated vesicles. There is water in the phase, either within the bi-layers or between the vesicles. Water between the vesicles can be referred to as

the 'pore water'. The NMR method described above characterises the spacing between the vesicles, or vesicle aggregates by modelling the space between the vesicles as spherical pores. This geometry can give indications of the microstructure of the system as changes in the water pore size result from changes in the vesicle/aggregated vesicle size changes.

Clearly from Figure 5.3, it can be seen that the ratio of the isotropic phase to lamellar phase decreases until there is no isotropic phase left. So, to try to understand the nature of this change further, the NMR method described will be used, and the 21 wt % model system with increasing polymer concentrations will be analysed in detail.

5.3 Methodology and Materials overview.

The PGSTE method described in Chapter 3 was utilised. The value of δ was fixed at 4 ms and the value of Δ was varied from 0.0025 to 0.75 ms. This ensured that enough data was collected in each of the regions (the decreasing D and constant D regions) for all the samples. The data from each diffusion experiment was fitted to the Stejskal-Tanner Equation (see Chapter 3) where D was one of the fitting parameters. D could then be determined for each observation time and then plotted against $\sqrt{\Delta}$, to which Equation 5.5 could be fitted for the values at low $\sqrt{\Delta}$ values to determine the surface area to volume ratio.

Each sample was prepared using stock NaLAS (45wt% solution, this was made up as shown in Chapter 3). This was diluted down to the concentrations required with H_2O and the required masses of sodium sulphate and water were added. This was left to heat at 70°C for 12 hours, stirring intermittently, and the samples were then poured into NMR tubes, which were kept heated in a water bath at 50°C for

TABLE 5.1: A Table showing the concentrations of the samples analysed for NMR analysis, showing the mass fractions (C) and the molar fractions (χ).

C_{LAS}	C_{POL}	C_{Na2SO4}	C_{H2O}	χ_{LAS}	χ_{Pol}	χ_{Na2SO4}	χ_{Water}
0.2150	0.0000	0.2400	0.5450	0.0193	0.0000E+00	0.0519	0.9289
0.2150	0.0100	0.2360	0.5390	0.0195	4.4318E-06	0.0516	0.9290
0.2150	0.0200	0.2320	0.5330	0.0197	8.9641E-06	0.0513	0.9290
0.2150	0.0400	0.2280	0.5170	0.0203	1.8459E-05	0.0519	0.9278
0.2150	0.0600	0.2240	0.5010	0.0209	2.8534E-05	0.0525	0.9266
0.2150	0.0800	0.2200	0.4850	0.0216	3.9243E-05	0.0532	0.9252

36 hours. This allowed any phase separation to occur. Before measurements were taken, the sample was left in the NMR machine at 50°C for 40 minutes.

As each sample contained 2 phases, the NMR tube was always positioned to ensure that the region of the sample analysed was the lamellar phase.

The concentrations of the sample that were analysed are outlined in Table 5.1.

5.4 Results and discussion

The first data obtained was the signal intensity as a function of magnetic field strength to determine the diffusion coefficient. The data for 0 wt% polymer is shown in Figures C.13 to C.15. The data for other polymer concentrations is presented in the Appendix.

The goodness of fits for the data are very high, between 0.992 and 0.998, and the data is fitted to a single exponential using a least squares fit, implying that NMR is only detecting one water population. When the attempt was made to fit to multiple populations, the fit was much weaker. This data is now subsequently further analysed to determine the surface area to volume ratio.

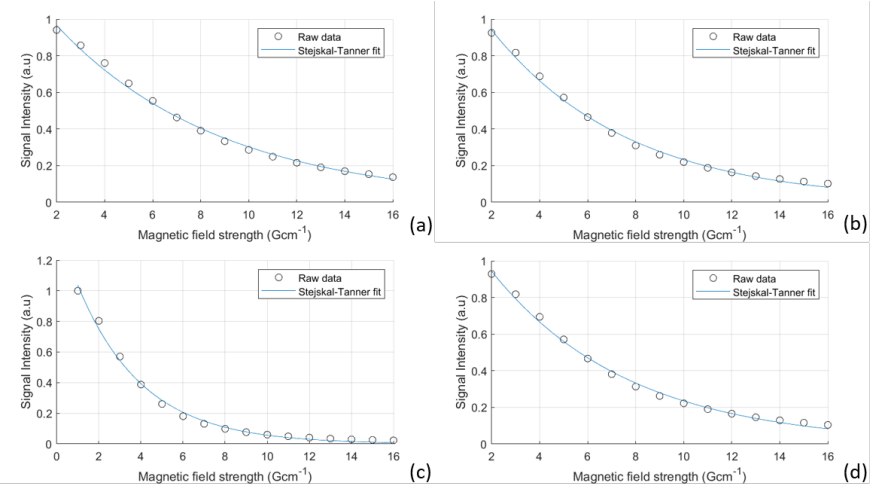

FIGURE 5.4: The raw NMR PGSTE data collected at 50°C, with 16 data points for each experiment, and 4 scans were employed per data point, data shown is for the 4 experiments with Δ values of: (a): Δ=0.0025s, (b):Δ=0.0045s, (c):Δ=0.005s and (d):Δ=0.0075s. The sample had a surfactant concentration of 21.5 wt%, polymer concentration of 0 wt%, sodium sulphate concentration of 24 wt% and water concentration of 54.5 wt%. The sample was left in the NMR machine at 50°C for 15 minutes before analysis.

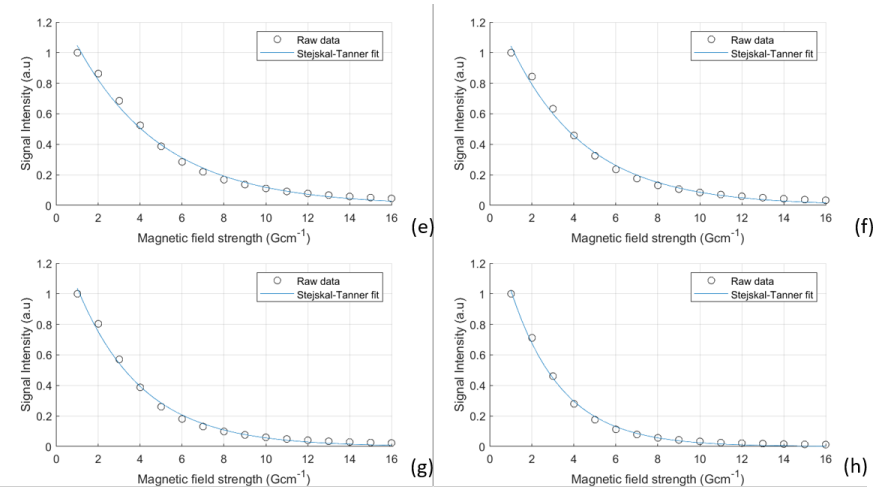

FIGURE 5.5: The raw NMR PGSTE data collected at 50°C, with 16 data points for each experiment, and 4 scans were employed per data point, data shown is for the 4 experiments with Δ values of: (e): Δ=0.025s, (f): Δ=0.035s, (g): Δ=0.08s and (h): Δ=0.18s. The sample had a surfactant concentration of 21.5 wt%, polymer concentration of 0 wt%, sodium sulphate concentration of 24 wt% and water concentration of 54.5 wt%. The sample was left in the NMR machine at 50°C for 15 minutes before analysis.

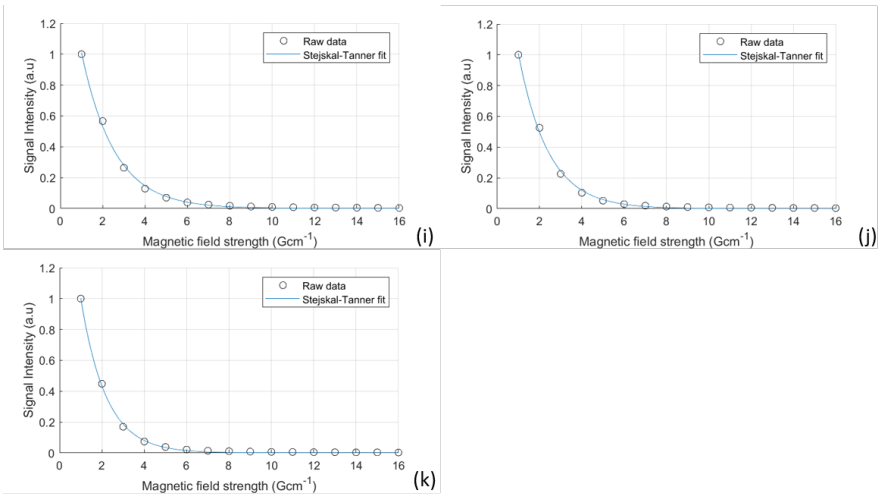

FIGURE 5.6: The raw NMR PGSTE data collected at 50°C, with 16 data points for each experiment, and 4 scans were employed per data point, data shown is for the 4 experiments with Δ values of: (a): Δ=0.2s, (j): Δ=0.3s and (k): Δ=0.45s. The sample had a surfactant concentration of 21.5 wt%, polymer concentration of 0 wt%, sodium sulphate concentration of 24 wt% and water concentration of 54.5 wt%. The sample was left in the NMR machine at 50°C for 15 minutes before analysis.

5.4.1 Determination of surface area to volume ratio of the pores

Following this, for the various values of Δ, the Diffusion coefficient vs $\Delta^{0.5}$ data could be plotted. The data for this is shown in Figures 5.7 to 5.12.

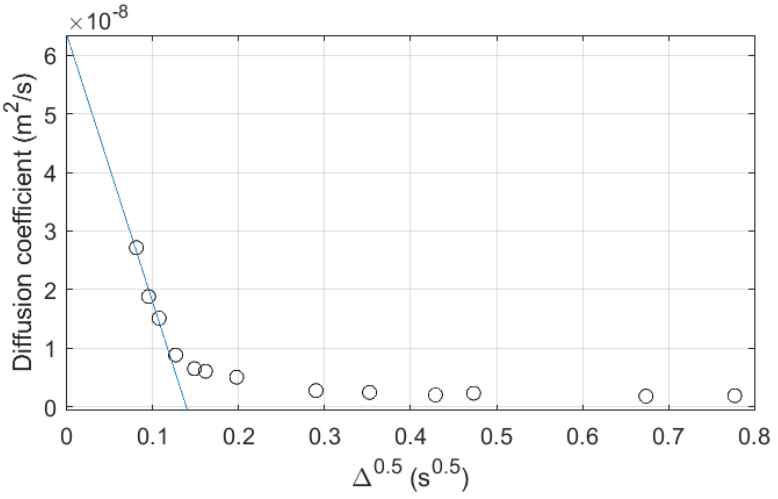

FIGURE 5.11: The diffusion coefficient vs Δ^2 plots for 6 wt% polymer. The first 3 data points were fitted to the Mitra Equation shown in Equation 5.5. The experiments were carried out with 21 wt% NaLAS in saturated sodium sulphate solution for a range of Δ values between Δ=0.0025 s and Δ=0.75 s

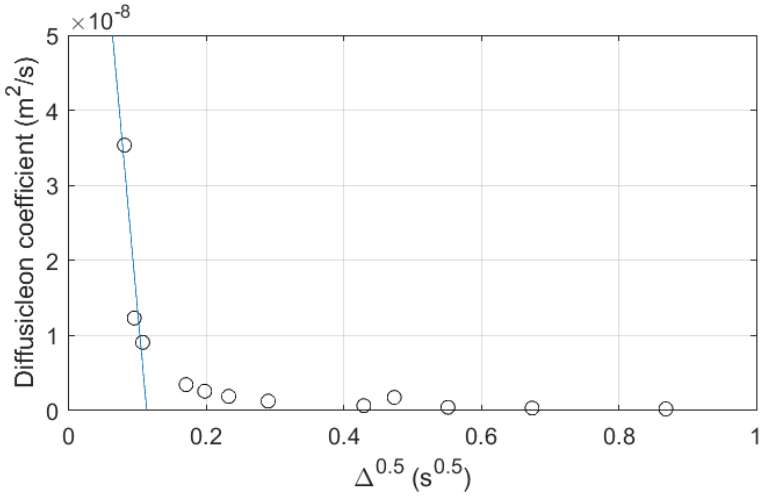

FIGURE 5.7: The diffusion coefficient vs Δ^2 plots for 0 wt% polymer. The first 3 data points were fitted to the Mitra Equation shown in Equation 5.5 The experiments were carried out with 21 wt% NaLAS in saturated sodium sulphate solution for a range of Δ values between Δ=0.0025 s and Δ=0.75 s

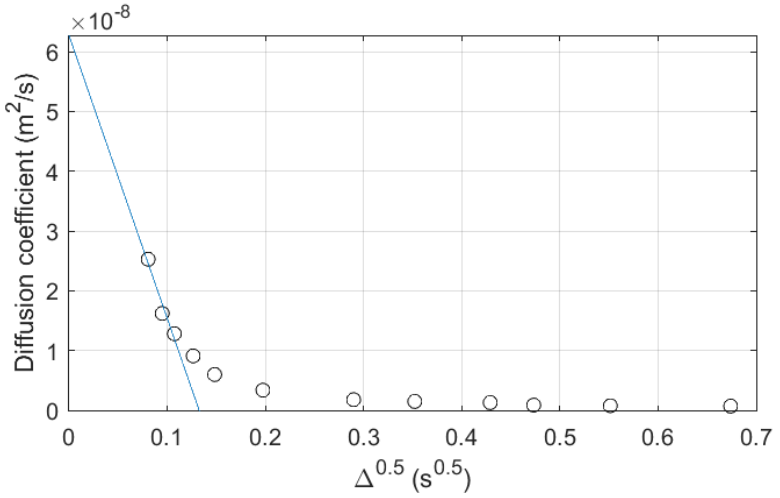

FIGURE 5.8: The diffusion coefficient vs Δ^2 plots for 1 wt% polymer. The first 3 data points were fitted to the Mitra Equation shown in Equation 5.5 The experiments were carried out with 21 wt% NaLAS in saturated sodium sulphate solution for a range of Δ values between Δ=0.0025 s and Δ=0.75 s

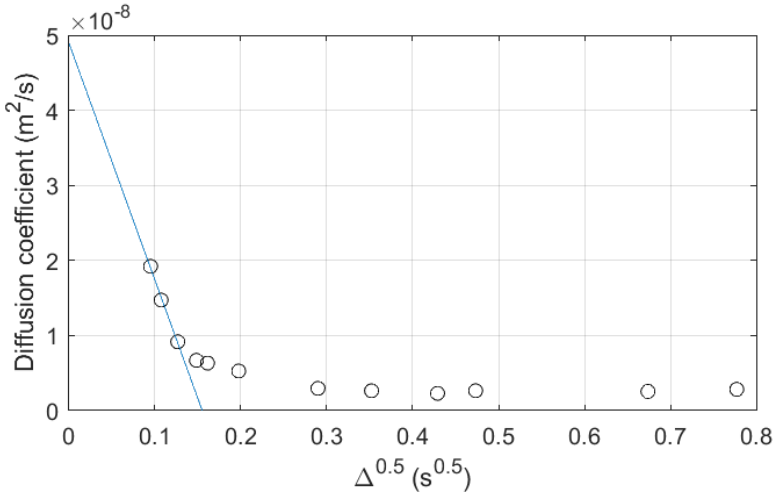

FIGURE 5.12: The diffusion coefficient vs Δ^2 plots for 8 wt% polymer. The first 3 data points were fitted to the Mitra Equation shown in Equation 5.5. The experiments were carried out with 21 wt% NaLAS in saturated sodium

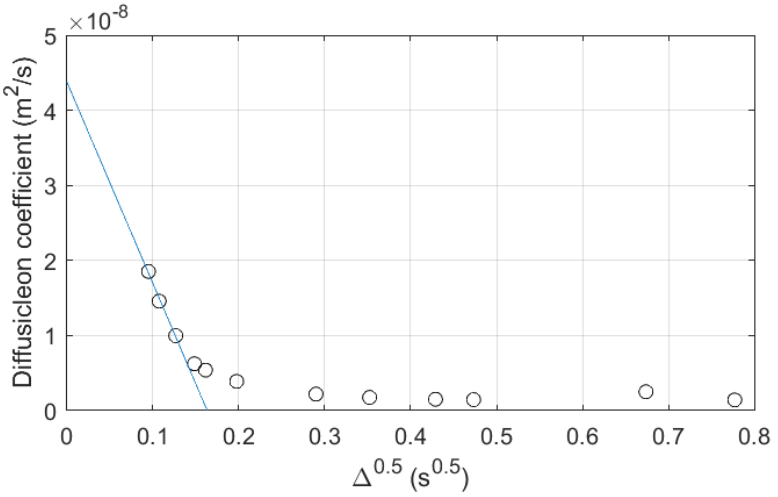

FIGURE 5.9: The diffusion coefficient vs Δ^2 plots for 2 wt% polymer. The first 3 data points were fitted to the Mitra Equation shown in Equation 5.5. The experiments were carried out with 21 wt% NaLAS in saturated sodium sulphate solution for a range of Δ values between Δ=0.0025 s and Δ=0.75 s

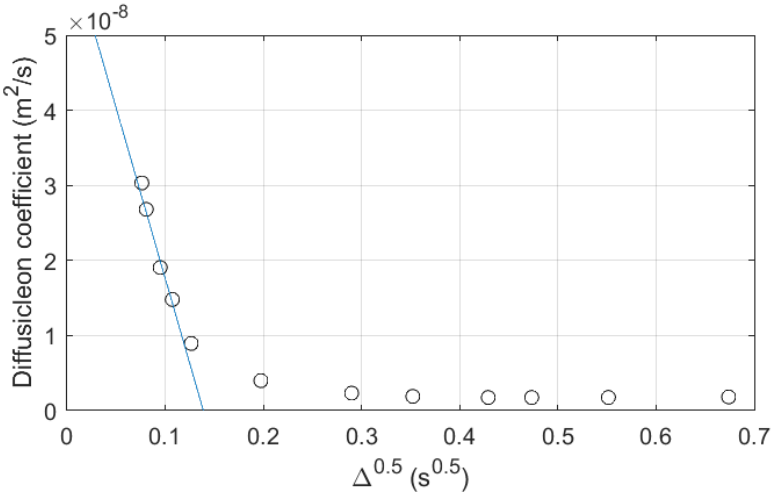

FIGURE 5.10: The diffusion coefficient vs Δ^2 plots for 4 wt% polymer. The first 3 data points were fitted to the Mitra Equation shown in Equation 5.5. The experiments were carried out with 21 wt% NaLAS in saturated sodium sulphate solution for a range of Δ values between Δ=0.0025 s and Δ=0.75 s

The first few data points were fitted to the Equation 5.5. This is subsequently be used to determine the S/V ratio for each system.

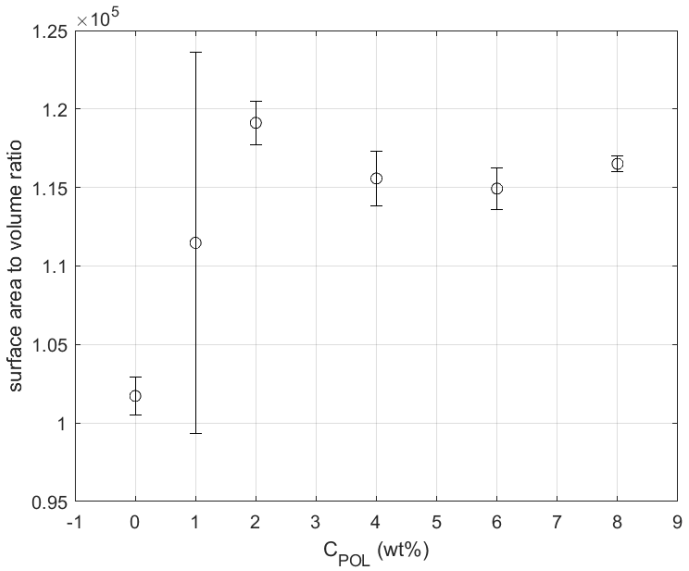

FIGURE 5.13: Graph depicting the influence of polymer concentration on the surface area to volume ratio of the pores, at 50°C.

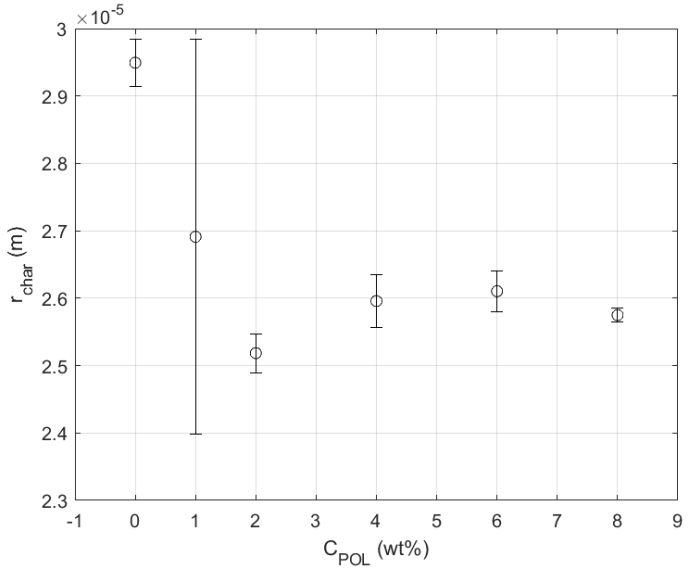

FIGURE 5.14: Graph depicting the influence of polymer concentration on the characteristic pore size, at 50°C.

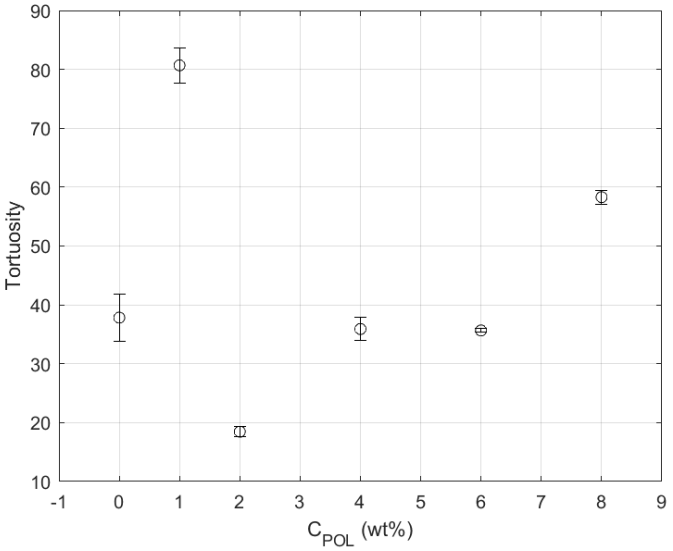

FIGURE 5.15: Graph depicting the influence of polymer concentration on the tortuosity of the system, at 50°C.

Figure 5.13 shows the change in surface area to volume ratio as a function of polymer concentration. There is no distinct relationship between polymer concentration and the pore surface area to volume ratio. This is perhaps because the ionic strength of the system is already very high as the solvent is saturated sodium sulphate solution. Therefore, the addition of the polymer is unlikely to cause any further aggregation of vesicles by further increasing the strong attractive forces between vesicles. As the addition of polymer doesn't have any clear effect on the surface area to volume ratio of the pores, there is naturally once again a lack of clear relationship between polymer concentration and the characteristic pore size seen in Figure 5.14, as well as the lack of trend between the polymer concentration and tortuosity shown in Figure 5.15. When relating this behaviour to the phase behaviour seen in Figure 5.3, it is rather strange. Firstly, the fact that there is less water in the isotropic phase implies that the polymer is forcing the water into the lamellar phase, as a result as the amount of water in the lamellar phase changes, it would be expected that the water pore size would increase, either by increasing the water pore size, or by swelling the lamellar sheets. Clearly, it has no effect

on the pore size, so the next step to be explored is the lamellar d-spacing using SAXS.

5.4.2 SAXS

Following this, SAXS was carried out to determine whether the phase behaviour changes could be attributed to the swelling of the lamellar phases. A water only sample was also analysed for background subtraction. Quartz capillary SAXS tubes were used with a 1.5 mm diameter, the acquisition time was 10 minutes per sample, and each experiment was carried out at 50°C. The SAXS machine was calibrated using silver behenate, and a Xeuss, 2.0 SAXS Small Angle X-Ray Scattering equipment equipped with Dectris Pilatus 3R 200K-A SAXS detector. Each sample was placed in a SAXS tube which were left in a hot water bath for 72 hours prior to analysis via SAXS. The samples were mounted onto the machine as such to ensure the lamellar region of the tube was analysed. The results are shown in Figure 5.16.

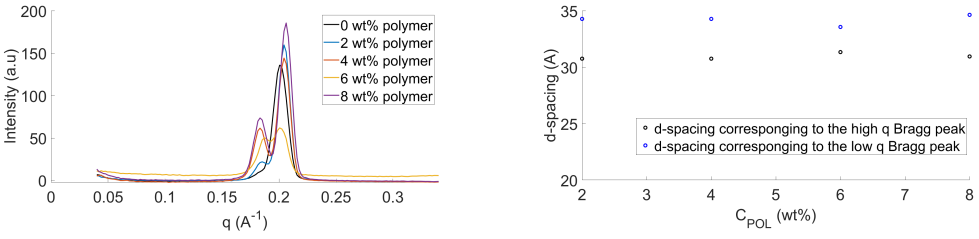

FIGURE 5.16: Raw SAXS data (left) and corresponding d-spacings of the Bragg peaks (right) of 21 wt% NaLAS in saturated sodium sulphate solution with increasing concentrations of polycarboxylate polymer.

From Figure 5.16, it can be seen that in all samples there are 2 Bragg peaks observed, indicating the presence of 2 lamellar phases resulting from the phase separation of the NaLAS phenyl isomers. However, there is no significant difference in the *d*-spacing as a function of concentration of polymer, this implies that the phase behaviour does not result from the swelling of the lamellar phase.

Now, the combination of the results from both NMR and SAXS are peculiar, as the increasing ratio of the amount of lamellar phase to isotropic phase implies that extra water has been forced into the lamellar phase, whereas the NMR and SAXS data implies that this is not the case.

A possible explanation for the increased volume fraction of the lamellar phase is the addition of polymer acting to increase the stability of the lamellar phase significantly. This can occur in the case in which the polymer is non-adsorbing. In most systems, non-adsorbing polymers act to destabilise colloids. If the polymer concentration is high enough, the depleting polymer ends up acting as a stabilising polymer - this is known as depletion stabilisation (99). This occurs because the concentration of polymer in water is high enough to ensure that the mixing Gibbs free energy is high enough to cause a repulsive the potential between the colloid and the polymer (at low polymer concentrations this is attractive). This supports why the stability increases further as the polymer concentration increases - the mixing Gibbs free energy of the system increases. The model behind this phenomenon is described further in the work by Feigin et al (100). This phenomenon however has to date not been frequently observed or studied in much detail, unlike the delpletion flocculation phenomenon which has been discussed greatly in literature (101–103).

5.5 Conclusion

This chapter characterised the phase behaviour of a NaLAS-polycarboxylate polymer system in saturated sodium sulphate solution. It observed a transition from a 2-phase lamellar/isotropic region to a single lamellar phase as determined by centrifugation. In order to try to understand this transition clearly, PGSTE NMR was used to determine the pore size as a function of polycarboxylate polymer concentration by carrying out PGSTE diffusion experiments. There was no trend

between the water pore size and polymer concentration observed. Furthermore, SAXS was carried out on the samples too, and no discernable change in the d-spacing of the 2 lamellar bragg peaks as a function of polymer concentration was observed. This was a peculiar result, as the phase diagram showed that increasing the polymer concentration increased the ratio of the volumes of the lamellar phase to the isotropic phase. However, it seemed that the pore size did not change, and the lamellar layers of the vesicles did not swell. This is peculiar as if the water has not been forced into the lamellar phase (as implied from the NMR and SAXS data) - where has it gone? A further analysis on the interactions of the polymer with the vesicles imply the polymer likely acts to stabilise the vesicles.

Chapter 6

Time dependent structural changes resulting from the application of shear

6.1 Overview

The literature review discussed some of the publications of the effect of shear on general surfactant systems, as well as the current understanding of the effect of shear on NaLAS-water systems.

There is, however, no current literature on extended time dependant behaviour on the structures, i.e. studies exploring if the extended application of shear influence the phase or colloidal behaviour, as is explored in this chapter.

The only published rheology experiments of NaLAS systems were carried out by James Stewart as shown in his doctoral thesis (5) for NaLAS in water and NaLAS-water-sodium sulphate systems. The studies were limited to flow curves

of 45 and 55 wt% NaLAS in water with increasing concentrations of sodium sulphate and the influence of temperature of the rheological behaviours. The main findings are shown in Figure 2.8. He observed shear thickening behaviour (but this data could not be easily fitted to any standard rheology model). This was likely a result of lamellar structures transforming into multi-lamellar structures upon the application of shear. The systems studies by Stewart, however are not representative of the model surfactant systems used in powdered detergent production, as slurry from which detergent powders are formed contain large amounts of undissolved sodium sulphate which may change the rheological behaviour completely. Moreover, he did not discuss any time related changes with respect to structure which are incredibly important when considering the processing of surfactant formulations because the structural changes influence the final product structure and hence performance with respect to powder flowability and dissolution properties. These time related changes will be discussed in this chapter.

6.2 Aims

- To observe the viscosity changes as model surfactant formulations are sheared at a constant rate in order to mimic industrial mixing;
- To relate these changes in viscosity of the model system to any internal structural changes.

6.3 Defining the model system

For this chapter, the initial model system, the composition of which is representative of a washing powder slurry, was analysed. The model system only contained

NaLAS in saturated sodium sulphate solution, with an extra amount of undissolved sodium sulphate, but changes in the composition were made in subsequent experiments to help determine structural understandings, as well as the influence of polymer.

The model system was defined by the following composition:

- 7.53 wt% NaLAS,
- 73.40 wt% Na_2SO_4,
- 19.07 wt% H_2O.

This system is the standard model system. and changes to this model formulation will be made slightly to help understand the causes in changes in viscosity, as well as the influence of polymer on time dependent changes.

6.3.1 Structure of the model system of interest

The model system consists of 3 phases. A neat lamellar phase (consisting of 2 lateral phase-separated lamellar phases), a lye (optically isotropic) phase and undissolved sodium sulphate. The presence of a high concentration of salt has a huge influence on the microstructure compared to if there is no sodium sulphate present (94). Without any salt, 21 wt% NaLAS (which is the percentage of NaLAS in water in the system when excluding the excess sodium sulphate) in water would consist of simply micelles in water. The presence of 21 wt% NaLAS in saturated sodium sulphate solution dehydrates the micelle head-groups, resulting in the aggregation of the micelles. This forms lamellar structures with a high surface curvature, so they mainly have a MLV morphology. The excess salt does not contribute to the surfactant phase behaviour, but can contribute to the structuring of the mixture, by essentially increasing the bulk density.

6.4 Experimental set-up

The time dependent changes in viscosity was measured using a rheometer. Various considerations with respect to the formula were made in order to determine the most suitable experimental set-up, particularly when choosing the most suitable rheometer geometry.

Due to the viscous and concentrated nature of the model system, wall slip could be an issue. Also, the system had a tendency to phase separate at some concentration regimes. So for this reason, the vane geometry proved the most suitable geometry for the experiments. The initial shear rate utilised was 3600 s^{-1} to help mimic high industrial mixing rates - other rates were also tested: 100s^{-1} and 1800 s^{-1}. Equipment details are provided in Chapter 3.

The samples were prepared using the 45 wt% NaLAS solution which was produced as described in Chapter 3, and the polycarboxylate 40 wt$^{\%}$ polymer in water solution. Finally, the sodium sulphate was provided by Sigma Aldrich. Prior to the rheology experiment, the required mass for each component was calculated. For NaLAS, the mass was measured directly ina a 20ml syringe, for the polymer, directly in a a 10ml syringe, the water into a 10 ml syringe and the sodium sulphate was weighed out in a 30 ml vial. The rheometer was heated and the procedure was set-up as necessary, and the temperature was set to 50 °C. Once the rheometer cup was left at 50°C for 20 minutes, the NaLAS was syringed into the rheometer cup, as well as the water, sodium sulphate and polymer. The rhometer was sealed with a solvent trap. Each component was left in the rheometer for 15 minutes without any stirring before the experiment could proceed to ensure that each component has reached the necessary temperature.

A vane geometry was used which had a diameter of 28 mm and a length of 42 mm. The cup was filled with at least 35 ml, this ensured that the whole vane

geometry was immersed in the sample.

6.4.1 Results and discussion: time-dependent viscosity changes for the model system.

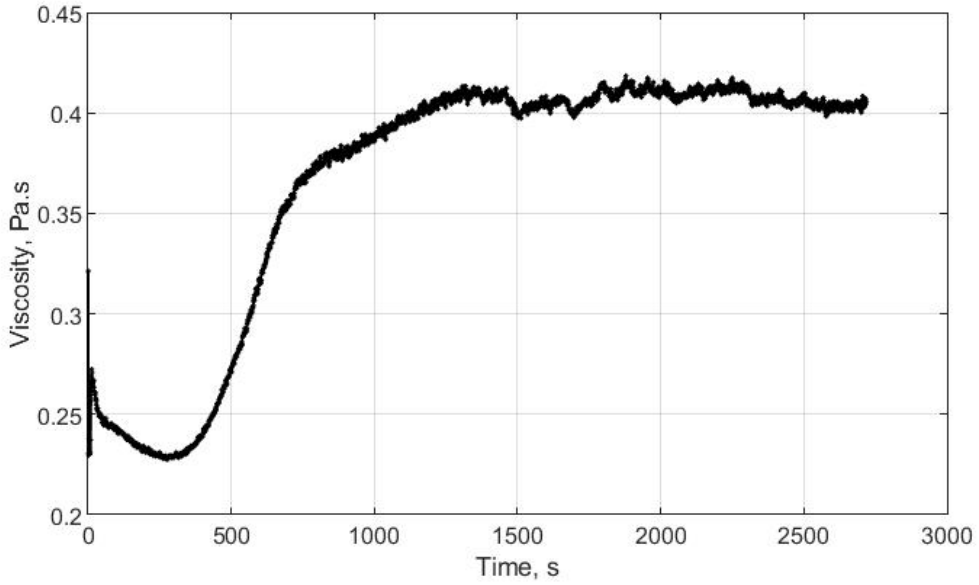

FIGURE 6.1: The results of a rheology experiment showing the change in viscosity over time for the model NaLAS-sodium sulphate-water system at 50°C over time, using a vane geometry at 3600s^{-1}.

The viscosity as a function of time was measured for the model system and the results are shown in Figure 6.1. Each component was added separately into the rheometer, so that all mixing occurred within the rheometer cup. Once all the components were added, the mixtures were left to heat to 50°C for 10 minutes. The sample was then sheared for 40 minutes at 3600 s^{-1}.

From 6.1, it can be seen that there is an initial drop in viscosity, this is likely due to the sodium sulphate powder being dissolved in the water and dispersed evenly. Following this, a sudden increase in viscosity from about 0.2 Pa.s to 0.41 Pa.s was observed over a time period of about 1000 seconds. This is characteristic of rheopectic behaviour, i.e. time dependent thickening upon the application of a constant shear stress as a function of time. This, however, is not in enough to show

rheopectic behaviour, as rheopectic behaviour is reversible, so the reversible nature of this should be explored with shear sweeps. So, the subsequent experiments in this chapter will show the results of the shear sweep and explore the possible causes of these viscosity changes.

6.5 Shear sweeps

6.5.1 Introduction and methodology: shear sweep experiments

The model system was analysed with 3 consecutive shear loop cycles. The experiment was carried out at 50°C, at logarithmically spaced intervals between $0.01s^{-1}$ to 3600^{-1}, then back again from 3600 s^{-1} to 0.01 s^{-1}. This loop was carried out 3 times, and followed a 100 second preshear at 3600 s^{-1}. In the case of rheopectic behaviour, hysteresis loops (which are reversible) should be observed.

6.5.2 Results and discussion: shear sweeps

From Figures 6.3, 6.4 and 6.5, and it can clearly be seen that the model system is not rheopectic. This is because a defining factor of a rheopectic system is the presence of a hysteresis loop that can be repeated indefinitely. This certainly is not the case in this system. In the first cycle there is a small difference in the behaviour of the flow curve between the increasing shear rate section and decreasing shear rate cycle (i.e. the loop shows some hysteresis), this is likely due to the the initial structural changes that are implemented as a result of the application of shear. These changes are irreversible, hence on the two subsequent cycles, no hysteresis is observed at all. This implies that the initial viscosity increase when shearing the NaLAS - sodium sulphate - water model system, as seen in Figure 6.1 maybe the

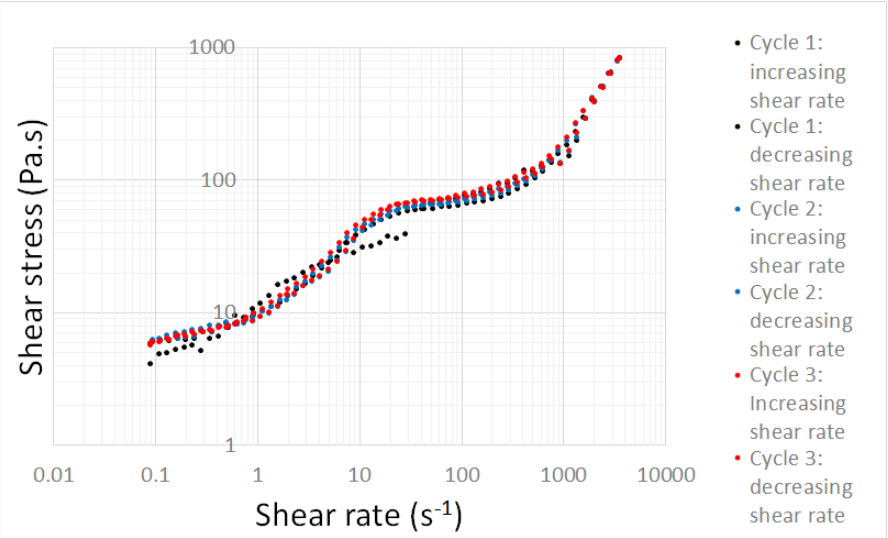

FIGURE 6.2: All 3 flow cycle curves following a 100 second preshear at 3600s^{-1}. Each cycle increased flow rates at logarithmically spaced intervals from 0.1 to 3600 s^{-1}, then decreased back to 0.1 s^{-1}. The experiment utilised a vane geometry at 50°C for the model formulation.

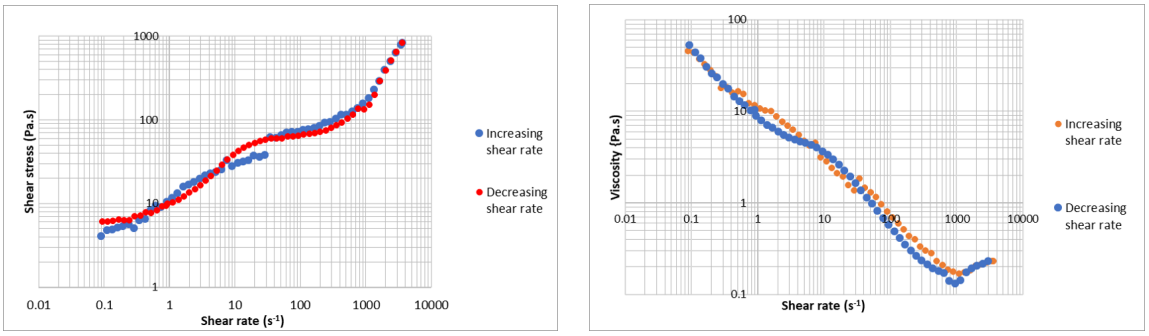

FIGURE 6.3: First cycle: flow curve cycle of the model system where the data points are logarithmically spaced, for shear rates between 0.1 s^{-1} and 3600 s^{-1} at 50 °C. The shear rates first increased from 0.1 to 3600 s^{-1}, then decreased back to 0.1 s^{-1}.

result of a permanent break down of some sort of structures within the system, or the result of the dissolution of the sodium sulphate. This break down of structure occurs within the time frame of the first hysteresis loop. At high shear rates (above about 1000 Pa) there is a gradual increase in viscosity. This is likely a result of secondary flow effects arising from the turbulent nature of the system at these rates.

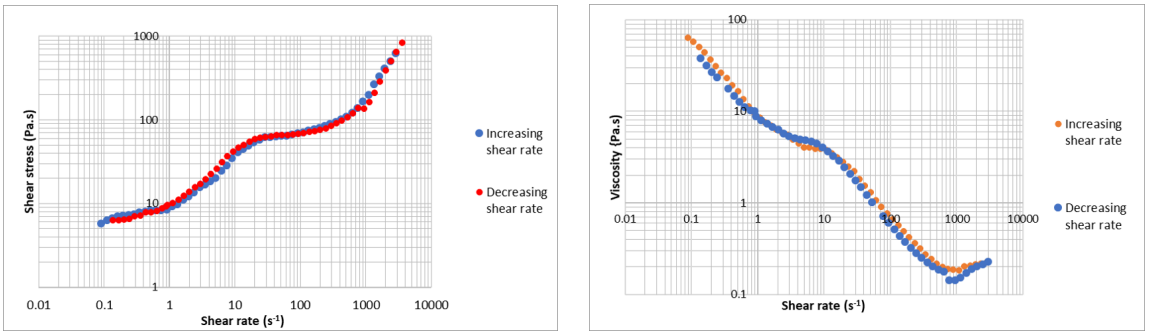

FIGURE 6.4: Second cycle: flow curve cycle of the model system where the data points are logarithmically spaced, for shear rates between 0.1 s^{-1} and 3600 s^{-1} at 50 °C. The shear rates first increased from 0.1 to 3600 s^{-1}, then decreased back to 0.1 s^{-1}.

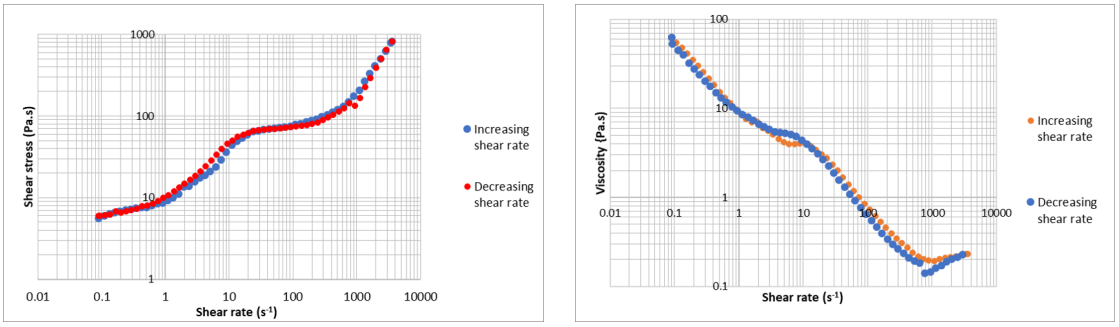

FIGURE 6.5: Third cycle: flow curve cycle of the model system where the data points are logarithmically spaced, for shear rates between 0.1 s^{-1} and 3600 s^{-1} at 50 °C. The shear rates first increased from 0.1 to 3600 s^{-1}, then decreased back to 0.1 s^{-1}.

6.6 Exploring the effect of excess salt

6.6.1 Introduction and system analysed

The model formulation was altered to remove the excess salt. Considering the water concentration in model system is 19.07 g/100 g, the solubility of sodium sulphate is 47.5 g/100 g water, so for 19.07 g of water there should be 8.97 g and the remaining NaLAS would be 7.03 g. Hence, the new concentration becomes:

$$C_{\text{NaLAS}} = \frac{7.03}{7.03 + 19.07 + 8.97} = 0.200, \tag{6.1}$$

$$C_{\text{Sodium Sulphate}} = \frac{8.97}{7.03 + 19.07 + 8.97} = 0.255, \tag{6.2}$$

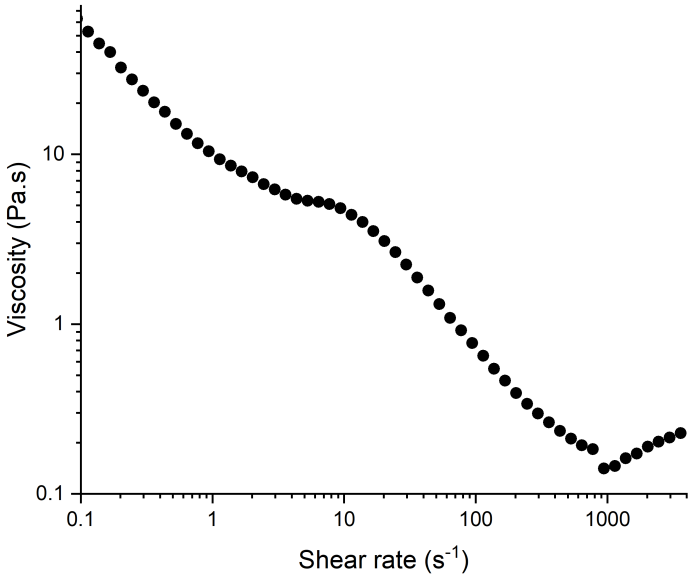

FIGURE 6.6: Second cycle: flow curve cycle of the model system at where the data points are logarithmically spaced. The shear rates increase from 0.1 s^{-1} to 3600 s^{-1} at 50 °C.

$$C_{\text{Water}} = \frac{19.07}{7.03 + 19.07 + 8.97} = 0.54. \tag{6.3}$$

This left a mixture of NaLAS dispersed in saturated sodium sulphate solution, this was subsequently analysed via rheology at a constant shear rate of $3600s^{-1}$ at 50°C.

6.6.2 Results and discussion: the effect of the addition of excess salt.

From Figure 6.7 There is an incredibly gradual increase in viscosity over time, from 0.44 Pa.s to 0.48 Pa.s over the 3600s experiment, this is almost negligble, and the difference in viscosity is not as profound in this system compared to the difference observed in the model formulation rheology experiment. This shows that the drastic increase in viscosity observed in the model system is results from the presence of the excess salt.

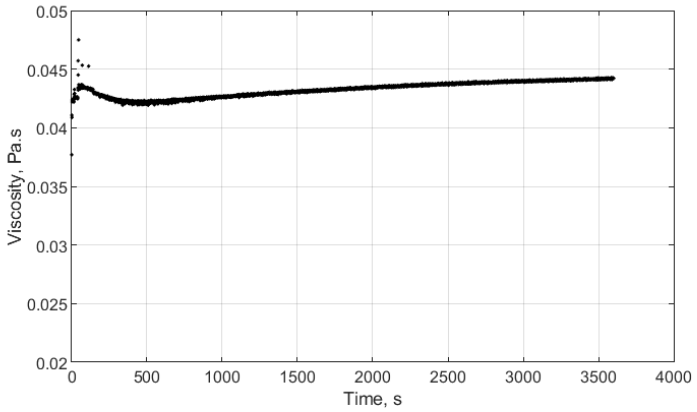

FIGURE 6.7: The change in viscosity as a function of time of a 20 wt% NaLAS, 25.5 wt% sodium sulphate and 45.4wt% water system measured by a rheometer at 50°C, with a vane geometry at 3600s^{-1}.

6.7 Exploring the dissolution of salt in the system

6.7.1 Introduction and methodology: the dissolution of salt in the system

Sodium sulphate is well known to increase the viscosity of water, and the extent to which is magnified as the salt concentration is increased. In this system there is a very high concentration of salt, enough for saturation plus extra which would remain as an undissolved solid. As the sodium sulphate is immediately added to the rheometer cup before the rheology experiment, it is possible that it is taking time for the sodium sulphate to dissolve completely.

In order to explore the cause of the increase in viscosity of the system, the idea that it may be due to sodium sulphate dissolution was explored. Some salts show a decrease in viscosity as a result of the dissolution of salt such as sodium chloride as they are 'structure breaking', but sodium sulphate shows an increase as it is 'structuring' (104). The reason for this has been proposed by Falkenhagen and Dole (105); electrical forces are established between ions in the solution which

results in a preferred arrangement that effectively 'stiffens' the solution, increasing the viscosity. Goldsack and Franchetto (106) explained that this viscosity increases exponentially with the concentration of the salt, so saturated solutions should have a viscosity (in the case of structuring salts) significantly higher than pure water. The viscosity of saturated sodium sulphate solution at 50°C is approximately 0.892 mPa.s, which is significantly higher than the 0.5465 mPa.s viscosity of water (104).

Now, in this system, there is the extra NaLAS component, which will have a profound influence of the bulk viscosity, as a range of additional forces come into play and these further contribute to the viscosity of the mixture, as well as undissolved sodium sulphate (the mass fraction of which is significant). So, for this reason it is clear that there are many factors that could contribute to the viscosity increase, but in this instance we are particularly exploring dissolution effects. Furthermore, the presence of salt can cause the micelles to aggregate into lamellar structures, which will naturally have a significantly different viscosity to micelles in water, this may also contribute to the changes in viscosity.

So, the constant rate rheology experiment was carried out to see if the observed increase in bulk viscosity of the model system by shearing over time is a result of the dissolution of sodium sulphate occurring in the rheometer. To do this, a sample was pre-made the day before the rheology experiment, where each component was mixed together and left at an elevated temperature for 16 hours, so any dissolution could occur prior to the rheology experiment. If the observed viscosity increase in the model system was due to the dissolution, the previously observed viscosity increase should not be observed in this experiment.

The mixture was placed in a 60 ml vial and heated to 80°C for 5 minutes in a water bath, then agitated thoroughly by hand with a spatula for 15 minutes. Following this, the sample was sealed and left in a hot water bath at 80°C for 12

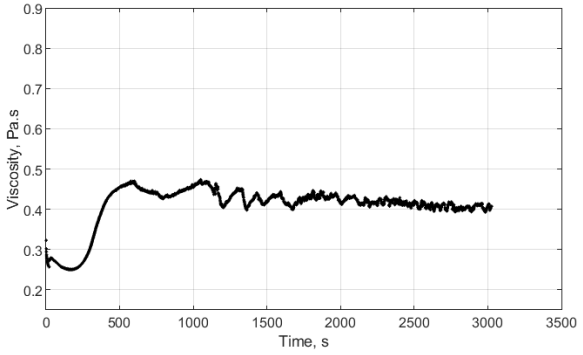

FIGURE 6.8: The change in viscosity as a function of time of a model NaLAS - sodium sulphate - water system, measured by a rheometer at 50°C, 12 hours after the sample is mixed and in a hot water bath at 50 °C. The rheology experiment was ran with a vane geometry at a rate of $3600s^{-1}$

hours, following which the viscosity as a function of time was measured using a rheometer.

6.7.2 Results and discussion: exploring the dissolution of salt in the system

From Figure 6.8, it can be seen that the same viscosity increase followed by a plateau is still seen, just like what is observed when the model system is sheared for 3600s with each component being added separately to the rheometer cup immediately before the rheology experiment, so this implies that the viscosity increase is not due to salt dissolution.

6.8 SAXS experimental analysis of the structural analysis of microstructure evolution

6.8.1 Introduction

As previously described, NaLAS can be characterised in terms of its lamellar d-spacing when in the lamellar phase. This describes the repeating thickness of the surfactant layer plud the water layer. It is possible that the change in viscosity as a function of time is due to changes in the d-spacing. This was therefore explored by aliquoting samples during the SAXS runs and analysis the sample using SAXS equipment and different points along the rheology experiment.

6.8.2 Methodology

Multiple rheology runs were carried out, for different lengths of time at a shear rate of $3600s^{-1}$ using a vane rheometer for the model system. These include: 60 seconds (experiment A), 120 seconds (experiment B), 300 seconds (experiment C), 500 seconds (experiment D), 800 seconds (experiment E), 1100 seconds (experiment F), 1700 seconds (experiment G) and 1800 seconds (experiment H).

For sample aliquoting, a 5 ml syringe and needle which had been kept in a beaker in a water bath at 50 °C. This syringe was used to take 1 ml of sample out of the rheometer, which was immediately used to fill a paste cell with a small amount (about 200mg) of the sample. Everything was kept at 50°C. The paste cell with the sample in was mounted on a SAXS holder which was also heated to 50°C. Each sample was ran using the SAXS equipment for 30 minutes. They data from the tubes were background subtracted using an empty paste cell. Each cell was sealed with polyimide tape which was transparent to the X-ray radiation.

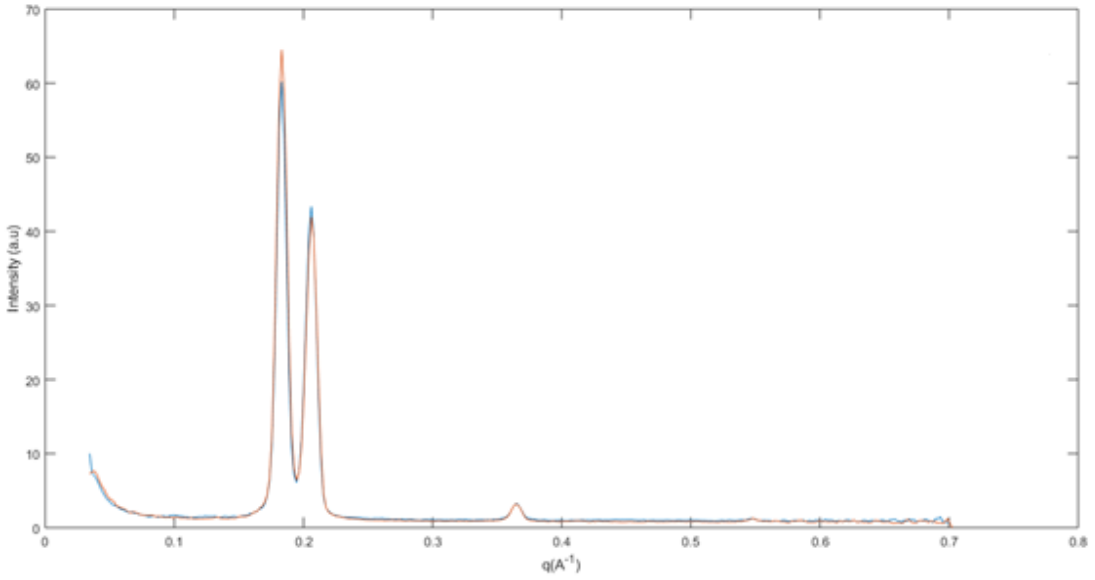

FIGURE 6.9: SAXS data at 50°C of the model system after it had been sheared for 120 seconds (orange) and 800 seconds (blue). X-ray exposure time was 30 minutes and all data is background subtracted.

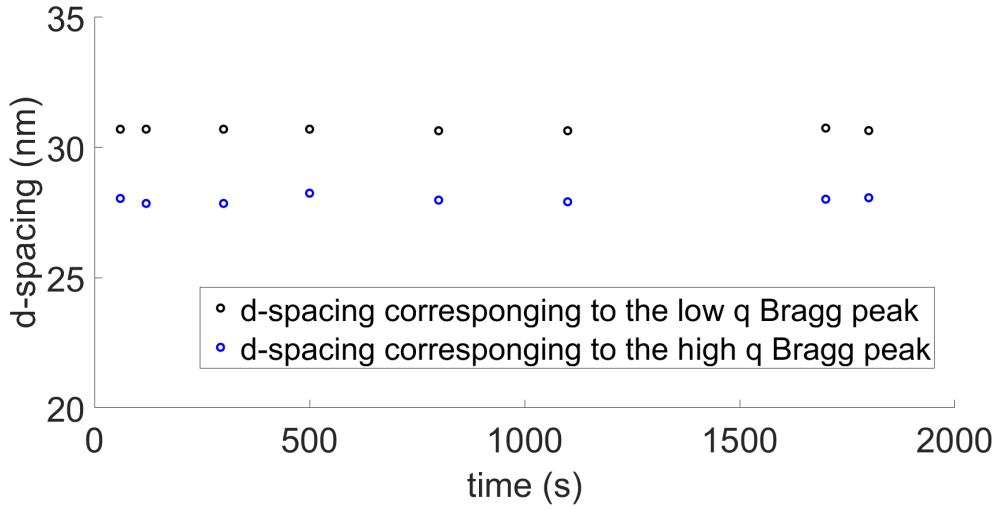

FIGURE 6.10: SAXS data at 50°C of the model system, showing how the d-spacing of the 2 lamellar peaks change as a function of shearing time. The shearing occurred at 50°C, at a rate of 3600 s^{-1} using a vane geometry.

6.8.3 Results and discussion

Figure 6.9 shows an exemplar raw SAXS data plot of 2 of the data sets. This is representative of all the data, as all the data showed two Bragg peaks at q values between 0.18 and 0.22 A^{-1}. A repeating Bragg peak was also observed at $2q_{Bragg}$.

It is clear from Figure 6.10 that there is no change in d-spacing as the sample is sheared, this makes clear that any structural change does not result from the swelling or de-swelling of the lamellar structures.

6.9 Direct structural evolution observation using cryo-SEM

6.9.1 Introduction and methodology: cryo-SEM experiments

Cryo-SEM was used to directly observe any structural changes that occur over time whilst shearing. The first sample analysed was 120 seconds into the rheology experiment (so just before the observed viscosity increase began). The second sample was following 600 seconds of shear, i.e in the middle of the viscosity increase slope. Finally, the last sample was analysed after the sample had been sheared for 30 minutes, when the sample had plateaued for some time (all at $3600s^{-1}$. The rheology experiment was the same as what was described in section 3 with respect to the sample analysed and shear rate used. However, the experiment was stopped after 120 seconds for the first cryo-SEM experiment, 600 seconds for the second cryo-SEM experiment and 30 minutes for the third cryo-SEM experiment.

So for each sample, once the sample had been sheared for a sufficient time, the cup containing the sample was immediately removed from the rheometer and placed in a hot thermos cup to maintain the temperature of the sample. The sample temperature was tracked as the sample was quickly transported to the room containing the cryo-SEM, where a small sample from the rheometer cup was taken and quickly plunged into nitrogen. This sample was then fractured with a

knife and spluttered with aluminium. Due to the relatively low moisture content, sublimation was not necessary.

6.9.1.1 Results: shearing for 120 seconds

A low magnification image of the sample after shearing the sample for 120 seconds can be seen in Figure 6.11. In this sample, there is a high density of crater like structures which are due to bubbles in the sample. Higher magnification images can also be seen in Figure 6.11, where the bubbles can be seen more clearly, and very small spherical like structures - likely mutilamellar vesicles can be seen, which seem pretty mono-disperse in size. Also, some irregular-shaped flake like structures which are likely salt crystals were present.

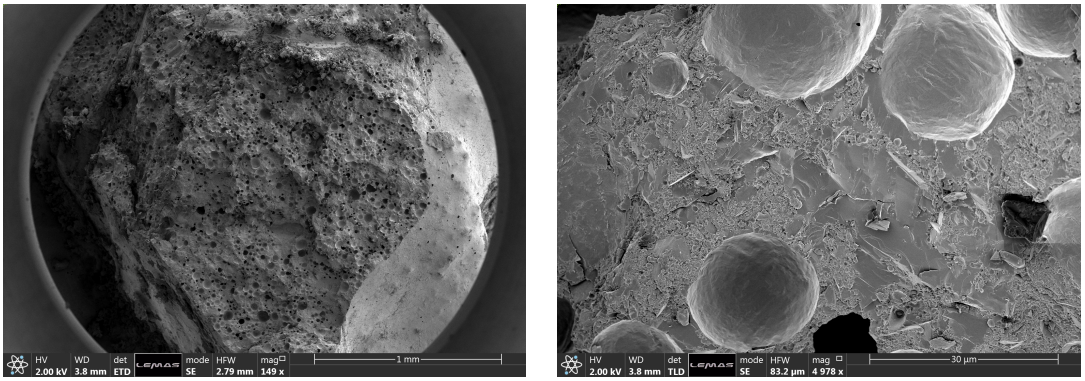

FIGURE 6.11: Cryo-SEM image of the model system, quenched after mixing the system in a vane rheometer set-up at 50°C for 120 seconds The width of the left micrograph represents 3.8mm and the width of the right micrograph represents 80 μm.

6.9.1.2 Results: shearing for 600 seconds

Figure 6.12, shows the cryo-SEM micrographs of the model system following 600 seconds of shear at 3600 s^{-1}. the features seen are again mainly spherical structures and irregular flake like structures just like the micrographs following 120 seconds shear. The main difference, however, is the bubbles seen in the low magnification

image. The density of bubbles present is noticeably lower, and the ones which are present are larger.

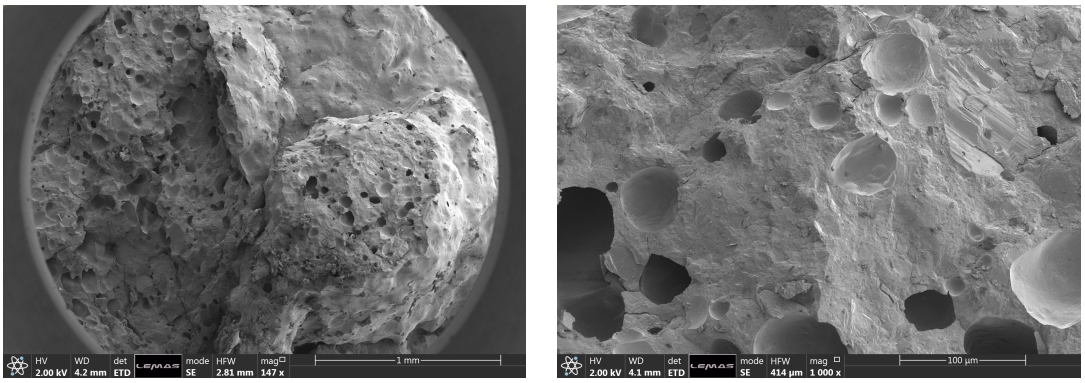

FIGURE 6.12: Cryo-SEM image of the model system, quenched after mixing the system in a vane rheometer set-up at 50°C for 600 seconds. The width of the left micrograph represents 3.8mm and the width of the right micrograph represents 500 μm.

6.9.1.3 Results: shearing for 30 minutes

Again, in Figure 6.13, the features seen in the micrographs which shows the formulation structures that result from shearing for 30 minutes again is similar to the previous 2 samples, but the main difference is the bubbles. In this sample, there are very few bubbles in comparison to the previous 2 samples and any bubbles which are present are significantly larger.

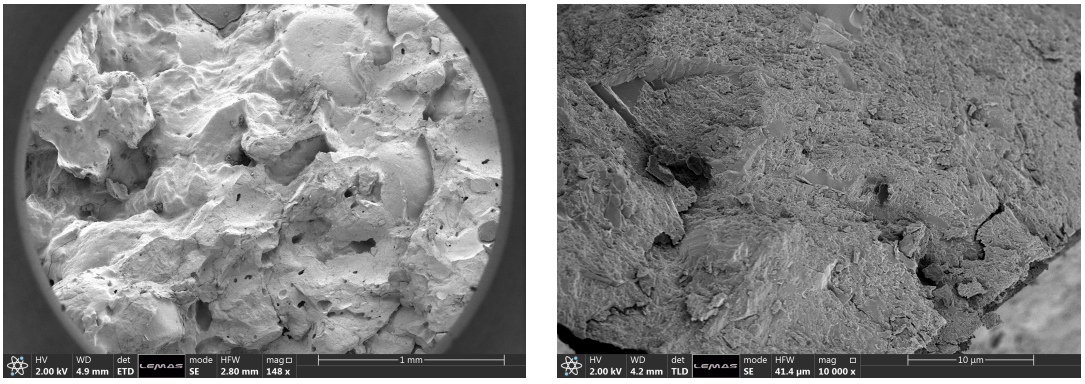

FIGURE 6.13: Cryo-SEM image of the model system, quenched after mixing the system in a vane rheometer set-up at 50°C for 30 minutes. The width of the left micrograph represents 3.8mm and the width of the right micrograph represents 80 μm.

6.9.2 Discussion of cryo-SEM experiment results

When comparing the cryo-SEM micrographs for each of the 3 systems, there is one distinct difference between all the samples. The first sample has a very high volume fraction of bubbles present, these bubbles are relatively small. By the second sample, this fraction this has significantly decreased. Finally, this volume fraction has decreased to almost zero by the final sample, and any bubbles which are presents are on average significantly larger than in the first sample.

This is perhaps the cause of the decrease in viscosity. Taylor (107) expanded on Einstein's model of the viscosity of solid-in-liquid dispersions to model the viscosity of fluid spheres-in-liquid dispersions in terms of the mass fraction of the dispersed phase present. It is a simple model as shown in Equation 6.4:

$$\eta_d = \eta \left[1 + 2.5\phi \frac{\chi_E + 0.4}{\chi_E + 1.0} \right], \tag{6.4}$$

where η_d is the mixture viscosity η is the viscosity of the continuous phase, ϕ is the volume fraction of the dispersed phase and χ_E is the viscosity ratio (i.e. dispersed phase viscosity to continuous phase viscosity ratio).

In the case in which the dispersed phase is gaseous (as it in this case) the viscosity ratio ≈ 0, so Equation 6.5 becomes (107):

$$\eta_d = \eta(\phi + 1). \tag{6.5}$$

This system does not fit Einstein's model, so to understand the behaviour, it is perhaps best to consider the viscosity in terms of the fact that air has a significantly lower viscosity than the NaLAS-sodium sulphate-water continuous phase, by incorporating the air into the mixture. Therefore, the system exhibits a volume weighted average of the 2 viscosities, and when the volume fraction of

air is higher, the mixture viscosity is lower. As the bubbles rise and bursts and the air volume fraction decreases, the mixture viscosity increases. The viscosity plateau is reached when the air has been removed from the system.

There are 3 ways in which a bubble can disappear is either by the bubble reaching the surface and creaming, dissolution and coalescence. The viscosity of the bulk system containing the undissolved solids and surfactant is very high. So when considering Stokes's law, the rise velocity of the bubbles is very low, as there is an inverse relationship between the rise velocity and continuous phase viscosity. Therefore, the surfactant stabilised bubbles remain kinetically stable (108). They are unlikely to reach the surface and burst. However, when the sample is sheared, the bubbles are moved around rapidly. The probability of 2 bubbles coming in close contact with each other is significantly increased and the velocity of the bubbles means that there is an increased probability that 2 bubbles collide with a force sufficient to coalesce (109). In Figure 6.12, it can be seen that after shearing for 600 seconds, the bubbles present are much larger than those at the start of the rheology experiment, supporting the theory that the high shear rate promotes coalescence. Once the droplet radius increases, the droplet rise velocity also increases, increasing the rate at which it reaches the surfaces and ruptures. Coalescence is only facilitated at high shear rates, where the Reynolds' number is high enough to ensure that the collision velocity of 2 droplets is sufficient to overcome the repulsive forces resulting from the surfactant stabilisation of the bubbles. Moreover, as the sample is moving around in the rheometer cup at such a rapid rate, the probability of a bubble reaching the surface and bursting is significantly increased. Another mechanism which may come into play in increasing the bubble break-up is the fact that at high shear rates, the viscosity is significantly increased compared to when the mixture is at rest.

The behaviour of this system does not follow Einstein's model of a gas dispersed in a liquid. From Equation 6.5 it can be deduced that as the volume fraction

of the air decreases, the viscosity should decrease. This however is not the case in this system - the viscosity increases as the volume fraction of air decreases. This is perhaps because as the air bubbles are removed, the surfactant vesicles and salt crystals can pack closer together on average. This tighter packing means the attractive forces throughout the system are stronger, hence the resistance to flow and subsequently viscosity, is increased.

One important thing to note is that the act of mixing the system per se is likely the cause of the air entrainment in the system, which the shearing acts to break up. It is hence important to carry out these time dependent experiments at different shear rates to see if the behaviour is observed at other shear rates, this is shown in the next section.

6.10 The influence of shear rate on time-dependent behaviour

6.10.1 Introduction and methodology: the influence of shear rate on time-dependent behaviour

The model system displayed the sudden increase of viscosity at a high shear rate of 3600 s^{-1}. The experiment was hence carried out at lower shear rates to determine whether this behaviour was observed at lower shear rates - 100 s^{-1} and 1800 s^{-1}. The data is shown in Figures 6.14 and 6.15.

6.10.1.1 Results and discussion: the influence of shear rate on time-dependent behaviour

From Figure 6.14, at $100s^{-1}$, the viscosity is somewhat constant over time but the curve is not smooth, it fluctuates slightly over time. Despite the fact that $100s^{-1}$ is still a relatively high shear rate, it still does not provide a sufficient shear to facilitate the removal of the bubbles from the system. As previously stated, the high viscosity of the continuous phase results in the dispersed air bubbles in the system stable as their rise velocity is very low. In the model system at 3600 s^{-1} , the viscosity of the continuous phase is significantly lower than at 100 s^{-1}, therefore, the rise velocity of the bubbles at this viscosity is lower still than at 3600 s^{-1}, therefore, more work needs to be done to increase the bubble rise velocity. the relatively low shear rate is not sufficient to force the bubbles to the surface or facilitate bubble coalescence, hence the bubbles cannot be broken down. Note that in Figure 6.14, the data is noisy, this is probably due to the log-jamming effect where the particles can't respond quickly enough when bumping into each other. This is much more likely to happen at lower shear rates (this was the lowest shear rate tested (110)).

At $1800s^{-1}$ (Figure 6.15, the increase in viscosity over time is once again observed. However, this increase is much more gradual than at $3600s^{-1}$. This is perhaps because the lower shear rate means that coalescence and bubble rise occurs at a much lower rate, because the viscosity of the system (excluding the bubbles) is much lower.

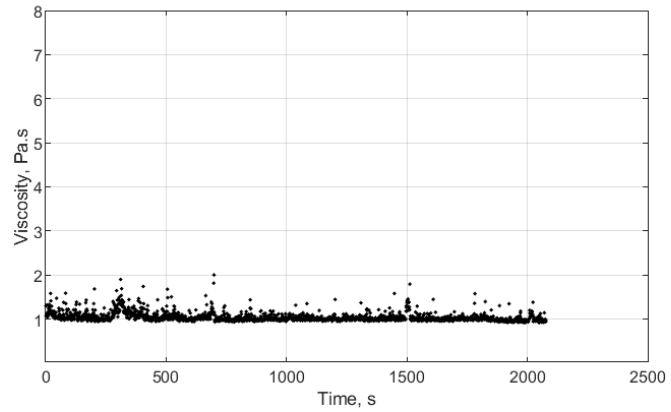

FIGURE 6.14: The change in viscosity as a function of time of a model NaLAS - sodium sulphate - water system, measured by a rheometer at 50°C, using a vane geometry, at a rate of $100s^{-1}$.

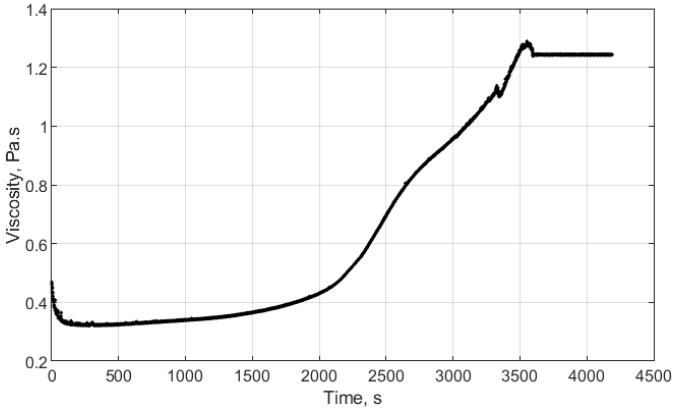

FIGURE 6.15: The change in viscosity as a function of time of a model NaLAS - sodium sulphate - water system, measured by a rheometer at 50°C at a rate of at a rate of $1800s^{-1}$ with a vane geometry.

6.10.2 Introduction and methods: the influence of the addition of polymer to the system.

6.10.3 CryoSEM of the system with polymer

Following this, the influence of adding polymer was explored on the time dependent behaviour of the system. 2 wt% of the polycarboxylate polymer was added as well as the other components (effectively displacing 2 wt% of the salt) and the viscosity as a function of time was measured. The results of which are seen in Figure 6.16.

A cryo-SEM experiment, where the experimental procedure was the same as described earlier in the chapter was also carried out on the system with 2 wt% polymer following 120 seconds of shear at 3600 s^{-1}. The cryo-SEM micrographs are shown in Figure 6.17.

Also, for a more comprehensive understanding of the influence of polymer on the phase behaviour of the system, a SAXS experiment was carried out for the model system, the model system with 2 wt% and the model system with 4 wt%. A water only sample was also analysed for background subtraction. Quartz capillary SAXS tubes were used with a 1.5 mm diameter, the acquisition time was 10 minutes per sample, and each experiment was carried out at 50°C. The SAXS machine was calibrated using silver behenate, and a Xeuss, 2.0 SAXS Small Angle X-Ray Scattering equipment equipped with Dectris Pilatus 3R 200K-A SAXS detector.

6.10.4 Results and discussion: the influence of the addition of polymer to the system

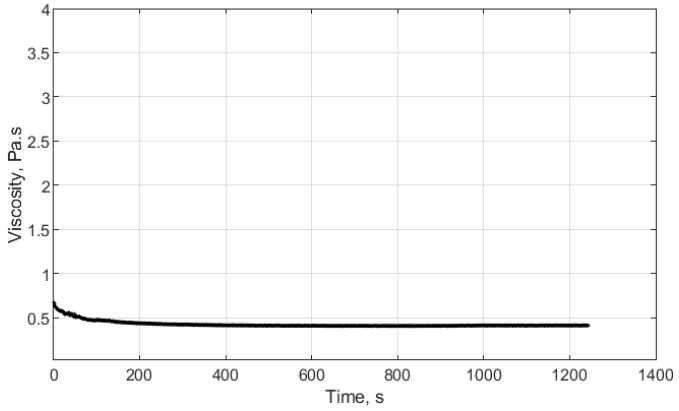

FIGURE 6.16: The change in viscosity as a function of time of a model NaLAS - sodium sulphate - water system, with 2 wt% of polycarboxylate polymer in place of some of the salt, at a rate of 3600s^{-1} with a vane geometry at 50°C.

The addition of polymer has significant effects on the time dependent behaviour of the model system. It is clear that once the polymer is added, the time

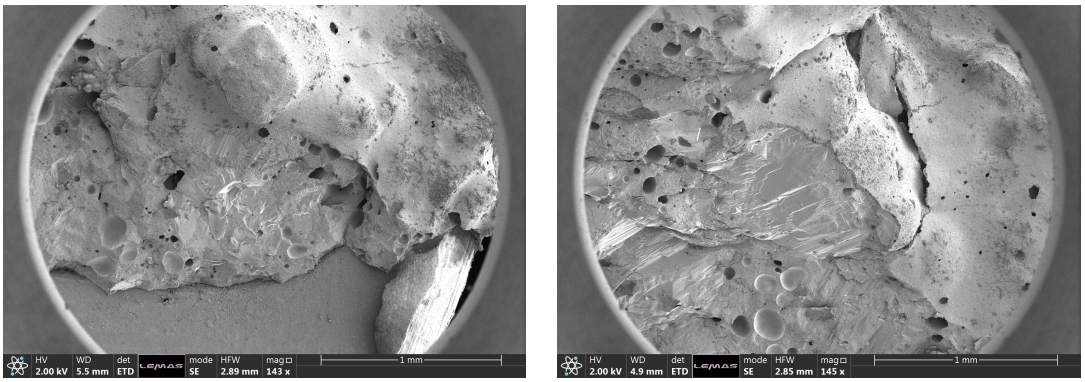

FIGURE 6.17: Cryo-SEM image of the model system with 2 wt% polymer, quenched after mixing the system in a vane geometry set-up at 50°C, sheared for for 120 seconds at 3600s^{-1}. The width of both micrographs represents 3.8 mm.

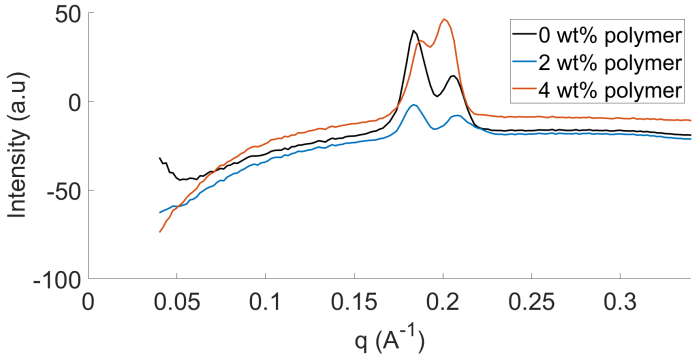

FIGURE 6.18: Raw SAXS data for the excess salt system with increasing concentrations of polymer at 50°C, with an acquisition time of 10 minutes per sample, the data is background subtracted.

dependent effects are elucidated; the viscosity as a function of time remains constant, this implies that the addition of polymer removes the air from the system, or prevents bubbles from forming in the first place. It is clear from the SAXS data in Figure 6.18 that this viscosity decrease is not due to changes in the phase structure. Looking at the cryo-SEM micrographs in Figure 6.17, it can be seen that the structure of the formulation after shearing at 3600s^{-1} for 120 seconds, and it can be seen that there are very few bubbles which are relatively large compared to the system without polymer which had been sheared for 2 minutes. This shows that the polymer inhibits the formation of small, kinetically stable bubbles. The mechanism for this is not completely clear, because from comparing the rheology data in Figures 6.11 and 6.17, it can be seen that the polymer acts to reduce the volume

fraction of the bubbles significantly, this is why the significant increase in viscosity is not observed in the system with the polymer, there aren't a significant amount of small bubbles which need to coalesce and cream to the surface of the model system. However, the mechanism by which the by which this occurs is not clear. What is surprising about this result is that the bulk viscosity of the model system is lower than the bulk viscosity of the model system with polymer, this is peculiar as Stokes' law shows that the creaming rate of the bubbles is higher in lower viscosity systems, so based on this it would be expected that any kinetically formed bubbles are more stable in the system with the added polymer. Considering this, it shows that the addition of polymer most likely inhibits the formation of kinetically stable bubbles in the first place. It is pretty unclear how the polymer acts to prevent the formation of these small kinetically stable bubbles, perhaps it is by preventing bubble nucleation in the first place. The polymer is not hydrophobic, so is unlikely to behave as a defoaming agent. Also it doesn't reduce the viscosity either, so an unconventional mechanism must be occurring to prevent the bubble formation or significantly increase the bubble rise velocity. Maybe the explanation for this can be considered by considering the phase behaviour described in Chapter 5. Increasing the polymer concentration increases the stability of the vesicles, and this is likely due to the polymer behaving as a deflocculant. Now, this system is not the same as the system described in Chapter 5 as there is a high mass fraction of undissolved sodium sulphate here, but a deflocculant primarily acts to decrease the viscosity of a system, as opposed to increase it, and the viscosity of the system with the polymer is higher than the viscosity without the polymer. This system can be modelled in such a way where the continuous phase is the same as described in Chapter 5, but there are 2 dispersed phases, the undissolved sodium sulphate and bubbles. Therefore, the mechanisms are incredibly difficult to simplify, as polymer can act to interact with the undissolved sodium sulphate, as well as the surfactant systems too, and the multiple mechanisms consequently make it incredibly difficult to attribute the exact cause of how the polymer acts

to prevent bubble nucleation.

6.11 Conclusion

This chapter explored a model system and how the system changed in viscosity over time as it was sheared. It was clear that the viscosity of this model system increased as a function of time until the viscosity plateaued, implying a structural change with time. However, this behaviour was only observed at very high shear rates and was irreversible. Further cryo-SEM studies showed that the viscosity decrease was due the removal of bubbles in the sample, this observation was backed up with previously published theories on the influence of air dissolved in a liquid on the system viscosity, as well as the breakdown of bubbles using shear at stressed above a critical stress. It was also shown that the addition of polycarboxylate polymer to the model system prevented the observed viscosity increase, this is because the polymer acts to help inhibit bubble nucleation.

Chapter 7

Conclusions

This thesis aimed to elucidate the phase and colloidal structural changes resulting from the addition of the polymer and those resulting from processing.

The influence the addition of the polycarboxylate polymer had on the phase and colloidal structure of NaLAS in water depended heavily upon the region of the phase diagram being considered. In the system at at 50°C, at low surfactant concentrations, the addition of the polymer induced phase separation of the micellar phase into 2 isotropic phases. At higher surfactant concentrations, the addition of the polymer induced the formation of a lamellar phase. At the highest studied concentrations of surfactant, the addition of the polymer induced a second lamellar phase which had both a different bulk density to the initial lamellar phase as well as an extra lamellar phase which could be observed by SAXS. Finally, ^{2}H NMR showed that an increase in multilamellar vesicle size was observed as a function of the polymer concentration. The combination of all this observed behaviour is likely a result of the polymer causing depletion flocculation effects in the system. The phase separation into 2 isotropic phases occured because the addition of the polymer to a micellar system created an osmotic gradient resulting from the negative adsoprtion of the polymer on the micelle surface. The increase

in the measured vesicle size resulting from the addition of the polymer caused the vesicles to aggregate and subsequently fuse into larger vesicles. In the future, techniques could be developed to determine the compositions of the different phases that phase separate.

Following this, the phase diagram of NaLAS-polycarboxylate polymer in sodium sulphate solution at 50°C was constructed. A clear transition from a visible lamellar plus isotropic phase to a single lamellar phase was observed after the samples were centrifuged. Diffusion NMR was carried out to probe this further by modelling the lamellar phase as a MLV system surrounded by water pores, and PGSTE NMR experiments were carried out to determine the changes in the surface area to volume ratio (S/V) of the pores as well as the pore size and system tortuosity as a function of the polymer concentration. No clear changes were seen in the S/V ratio, tortuosity or pore size as a function of the polymer concentration. Also, SAXS was carried out on the samples, and no changes in the d-spacing of the 2 lamellar peaks were seen either. This shows that although the transition of the 2 phase system to the one phase lamellar system should occur as a result of the water in the isotropic phase moving into the lamellar phase, either in the pores between the vesicles or within the lamellar layers, neither NMR or SAXS detected this happening.Therefore, it seems that the addition of the polymer acted to sterically stabilised the MLVs or groups of aggregated vesicles, which significantly increased the stability of the vesicle. This hence reduced the supernatant volume following centrifugation.

Finally, the influence of a high constant shear rate applied to a model slurry system was determined to model industrial mixing conditions. It was observed that when a high constant shear rate was applied, a distinct increase in viscosity over time was observed until a plateau was reached. Despite this being characteristic of rheopectic behaviour, it was shown that the behaviour certainly wasn't

rheopectic due to its irreversible nature, and the fact that this change was not observed at low shear rates. Cryo-SEM showed this viscosity increase resulted from bubble coalescence and hence the bubble rise velocity increasing. Once the bubbles reached the surface, they could burst. So as this process occured at a rapid rate at high shear rates, the volume fraction of the bubbles was reduced. This behaviour does not follow Einstein's equation for the viscoity of colloids which predicts an decrease in viscosity as the bubble fraction is decreased. The addition of a small amount of the polymer completely removes this time dependent changes in viscosity, perhaps because the addition of the polymer prevents bubble nucleation in the first place.

This work aimed develop a method to size the multilamellar vesicles in the high salt concentration system as a function of the polymer concentration. The technique used in the first results Chapter for MLV sizing is not suitable for this system under high ionic concentrations. During the project progress was made in developing a 2-D NMR pulse sequence which would be suitable for sizing vesicles in this system. Due to time limitations, however, this was not completed. This information would be incredibly helpful in understanding the influence of the addition of the polymer in the high sodium sulphate concentration systems in more detail.

Despite not sizing the vesicles in the high sodium sulphate conditions, this PhD was successful in characterising the influence of both polymer on the formulation structure in nil salt conditions and high salt concentration conditions, as well as how processing influences the structure of a model slurry.

Appendix A

Appendix A

Figure A.1 to A.3 shows the raw data for the transitions used to create the phase diagram in Figure 4.7

Figures A.4 and A.5 show the transitions for the phase diagram in Figure 4.16.

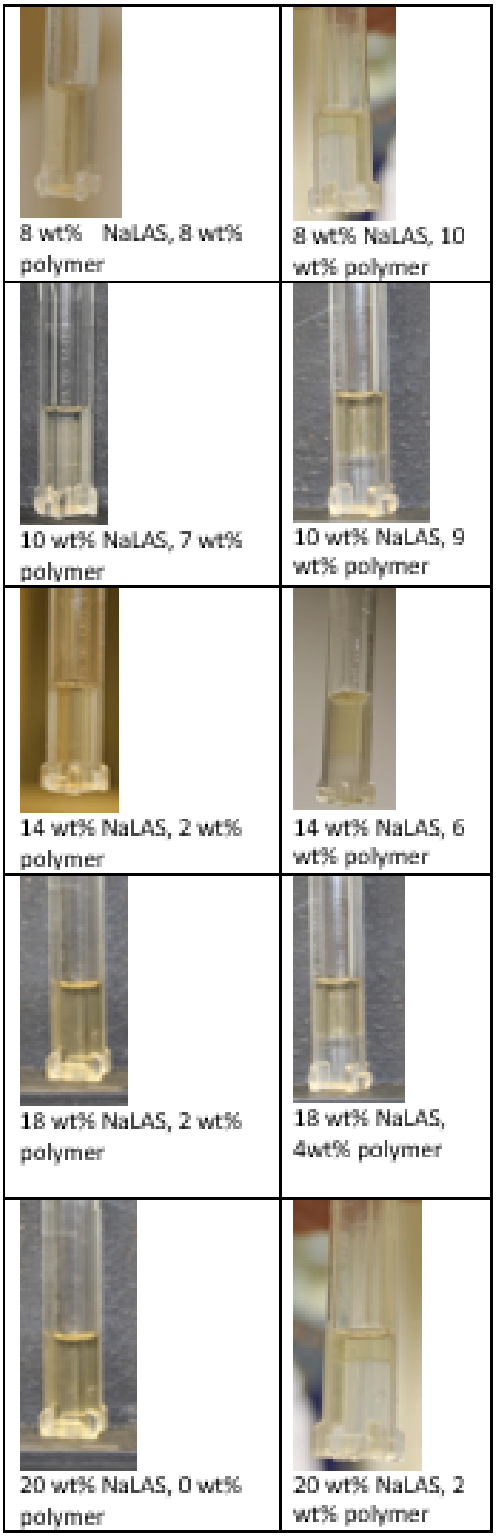

FIGURE A.1: Centrifugation to show the phase transitions for L_1 to L_1 + L_1'. All samples centrifuged at 50° for 2 hours and 17 minutes.

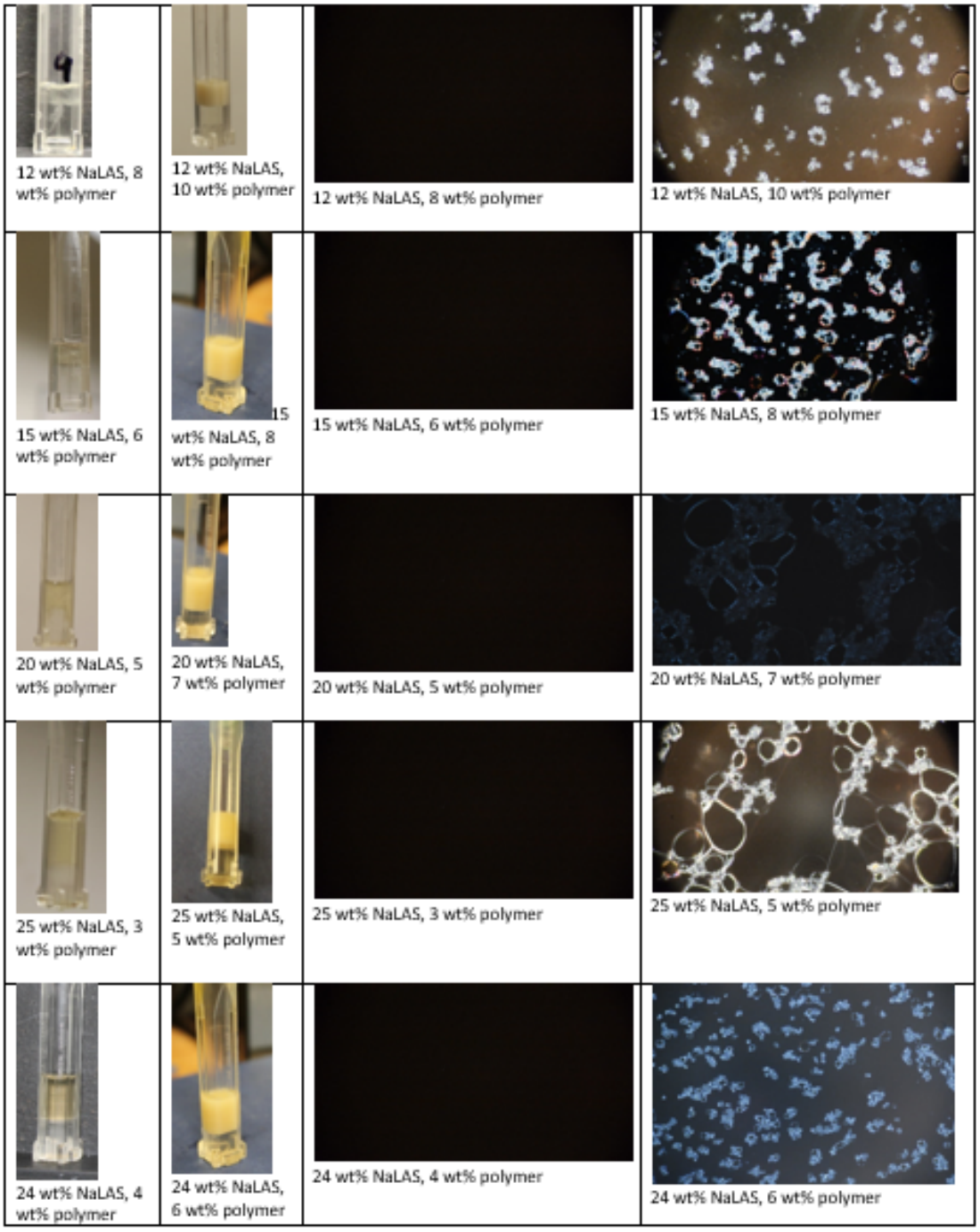

FIGURE A.2: Centrifugation and cross polarised microscopy to show the phase transitions for $L_1 + L_1$' to $L_1 + L_\alpha$. All samples centrifuged at 50° for 2 hours and 17 minutes, microscopy samples analysed at 50°, too.

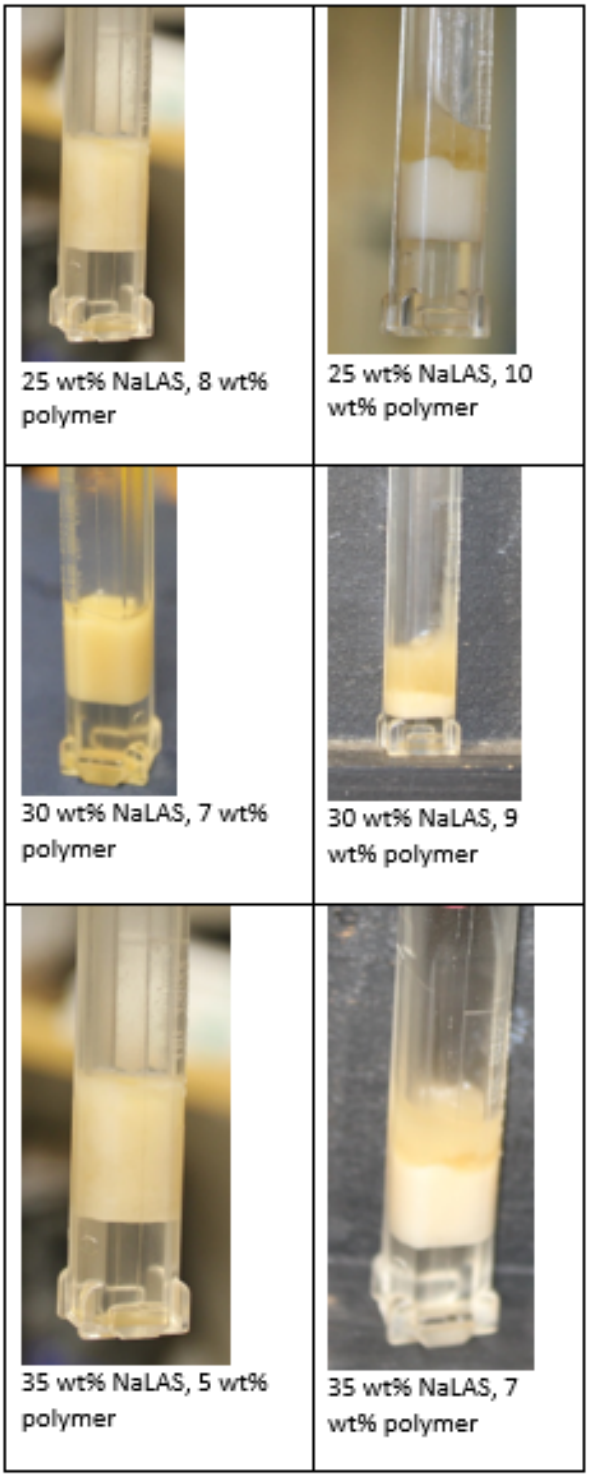

FIGURE A.3: Centrifugation to show the phase transitions for L_1 + L_α to L_1 +L_α+ L'_α. All samples centrifuged at 50° for 2 hours and 17 minutes.

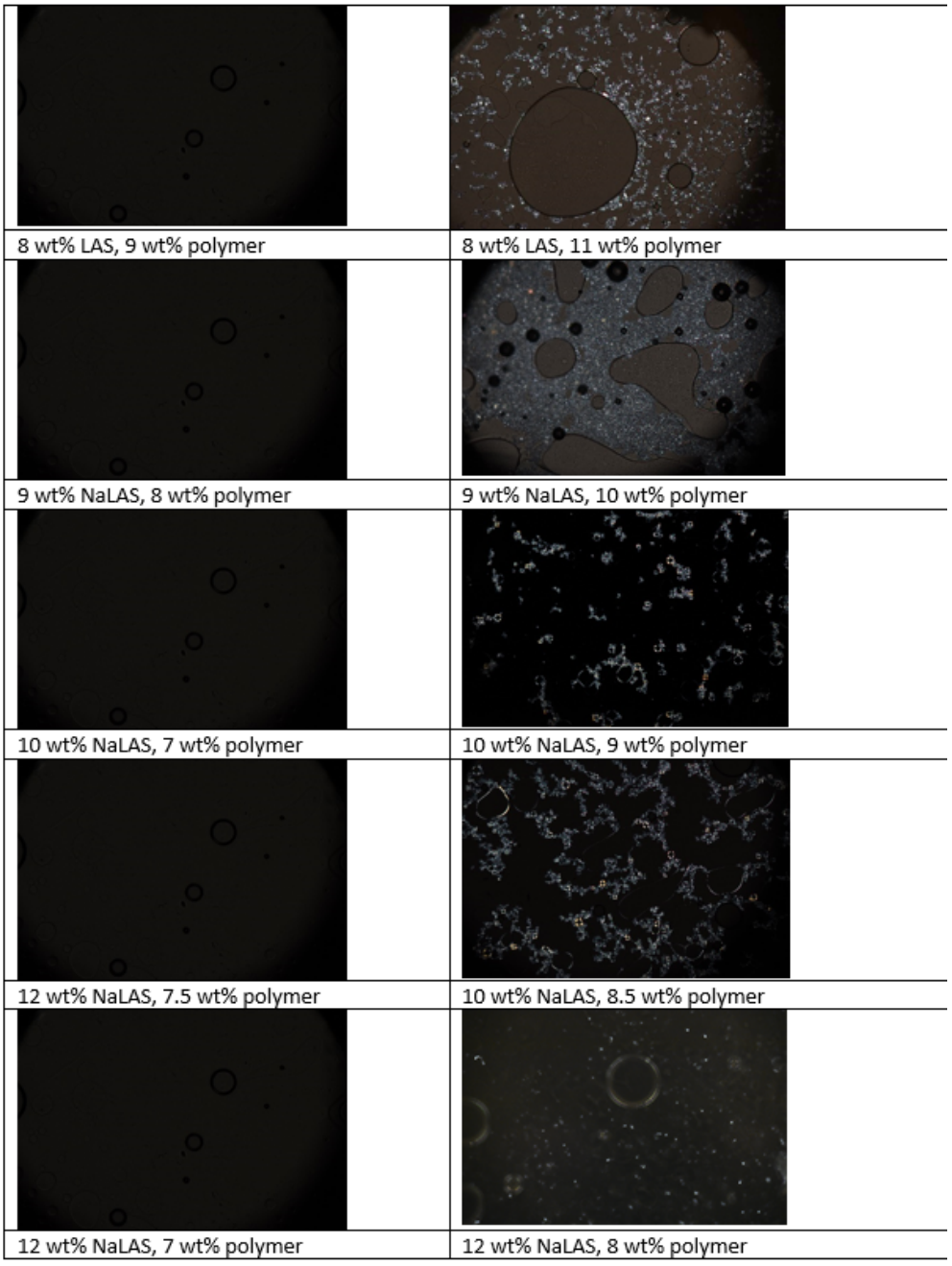

FIGURE A.4: Centrifugation to show the phase transitions for L_1 to L_1 + L_1'. All samples centrifuged at 50° for 2 hours and 17 minutes.

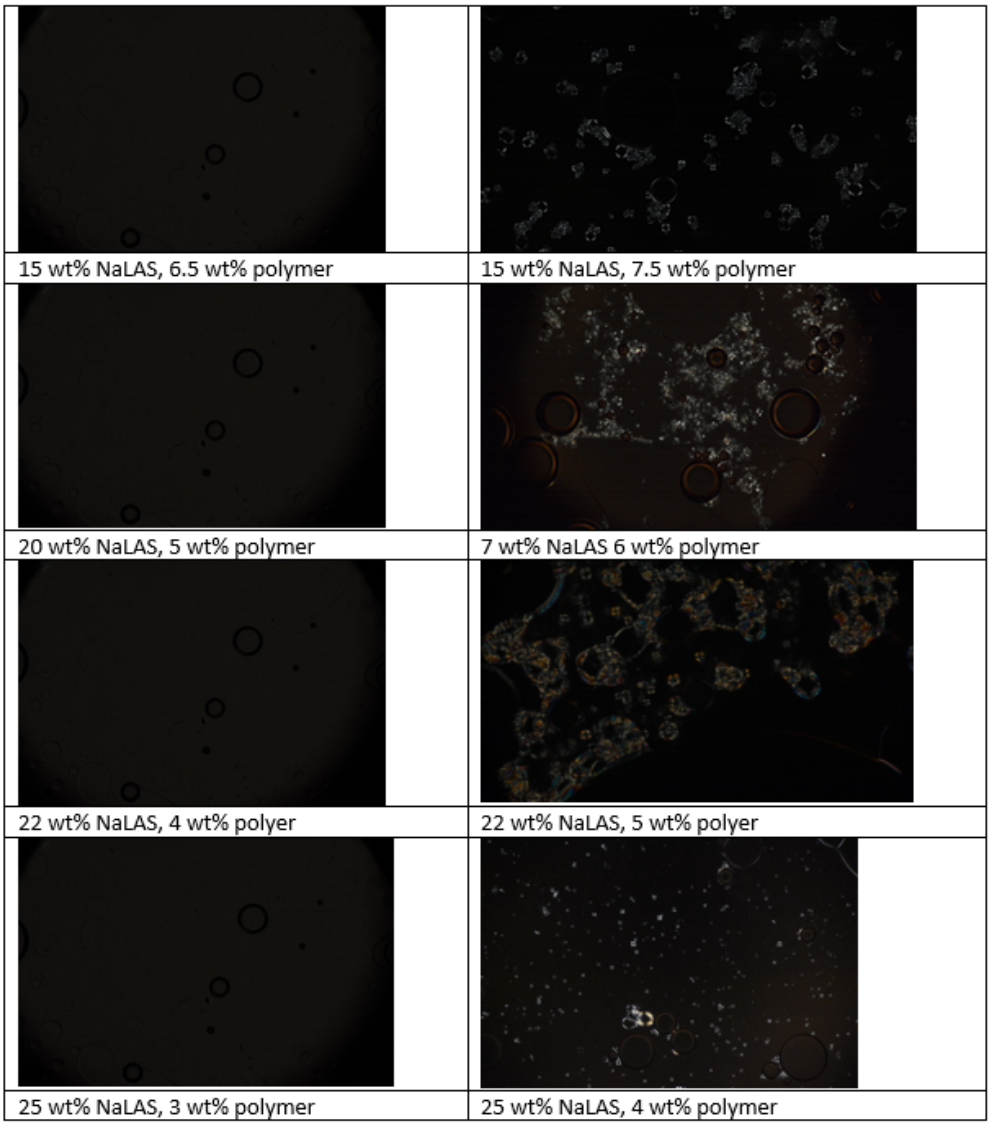

FIGURE A.5: Centrifugation to show the phase transitions for L_1 to L_1 + L_1'. All samples centrifuged at 50° for 2 hours and 17 minutes.

Appendix B

Appendix B

The data in this appendix shows the Lorentzian fits used to determine the half width at half-maximum and the Intensity-Magnetc field strength data used to calculate the diffusion coefficients for the data in Figure 4.15.

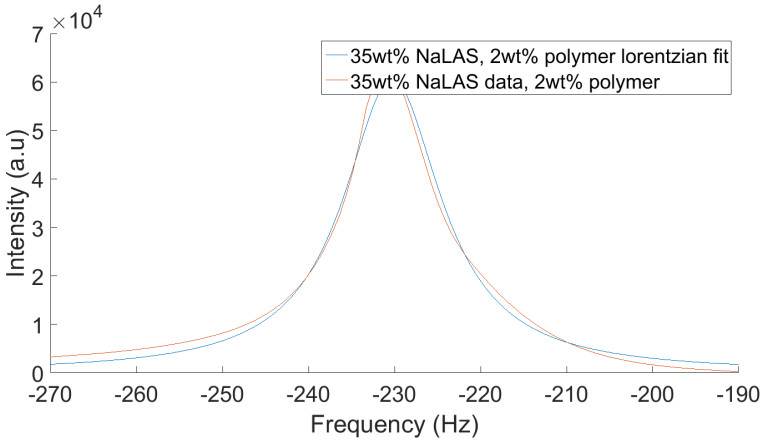

FIGURE B.1: Lorentzian fit to deuterium NMR spectra at 50°C. 35 wt% NaLAS and 2 wt % polymer.

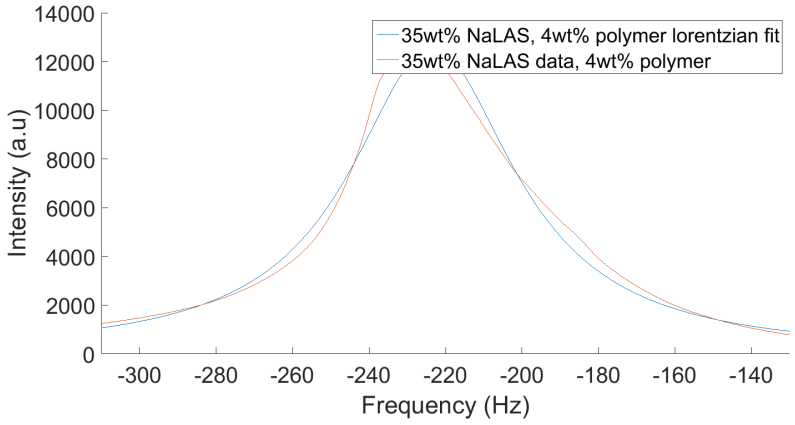

FIGURE B.2: Lorentzian fit to deuterium NMR spectra at 50°C. 35 wt% NaLAS and 4 wt % polymer.

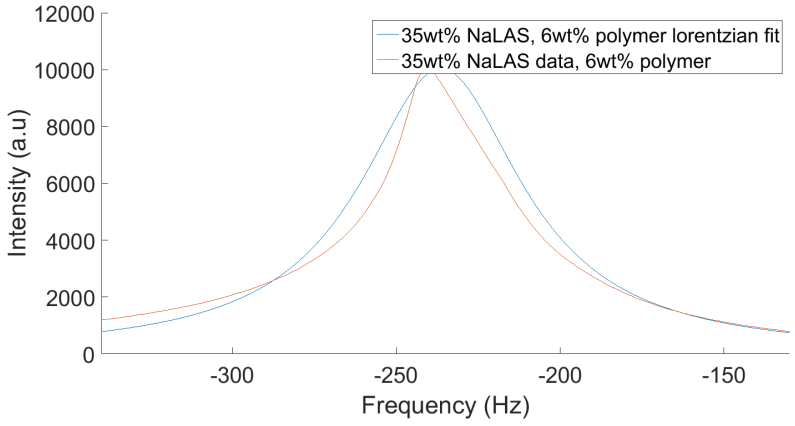

FIGURE B.3: Lorentzian fit to deuterium NMR spectra at 50°C. 35 wt% NaLAS and 6 wt % polymer.

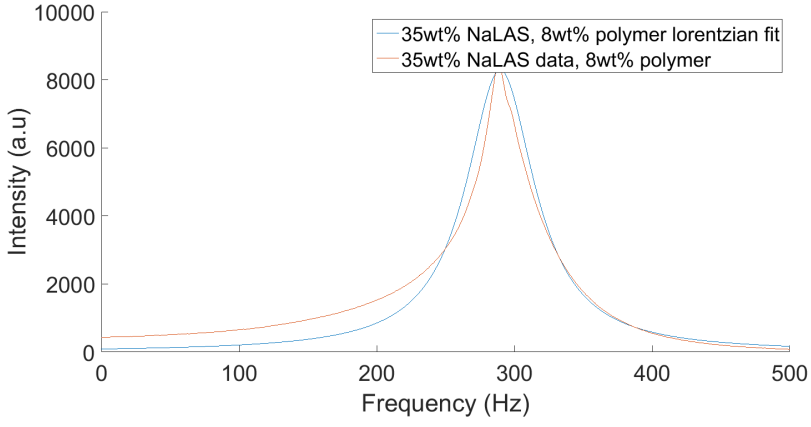

FIGURE B.4: Lorentzian fit to deuterium NMR spectra at 50°C. 35 wt% NaLAS and 8 wt % polymer.

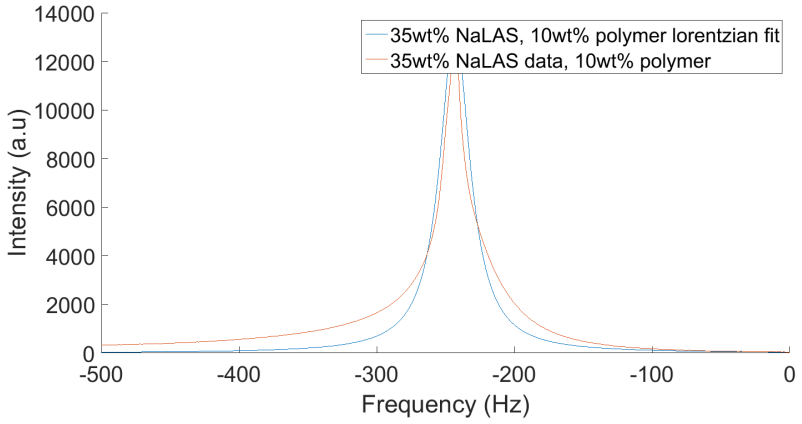

FIGURE B.5: Lorentzian fit to deuterium NMR spectra at 50°C. 35 wt% NaLAS and 10 wt % polymer.

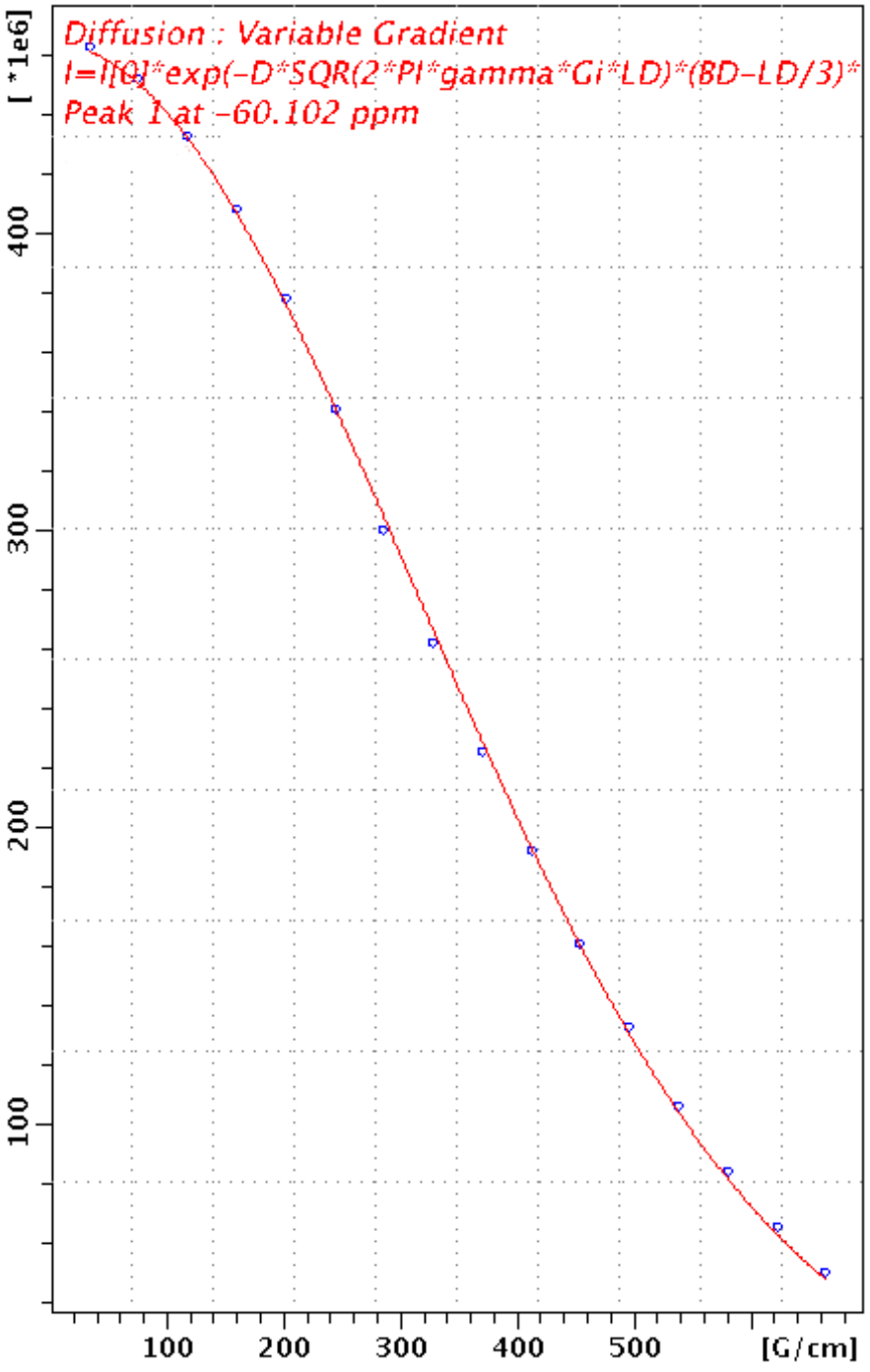

FIGURE B.6: RAW NMR of intensity of central isotropic peak as a function of Magentic field strength.The data shows the Stejskal-Tanner fit which is used to calculate diffusion coefficient. Experiment at 50°C - 35 wt% NaLAS and 2 wt % polymer.

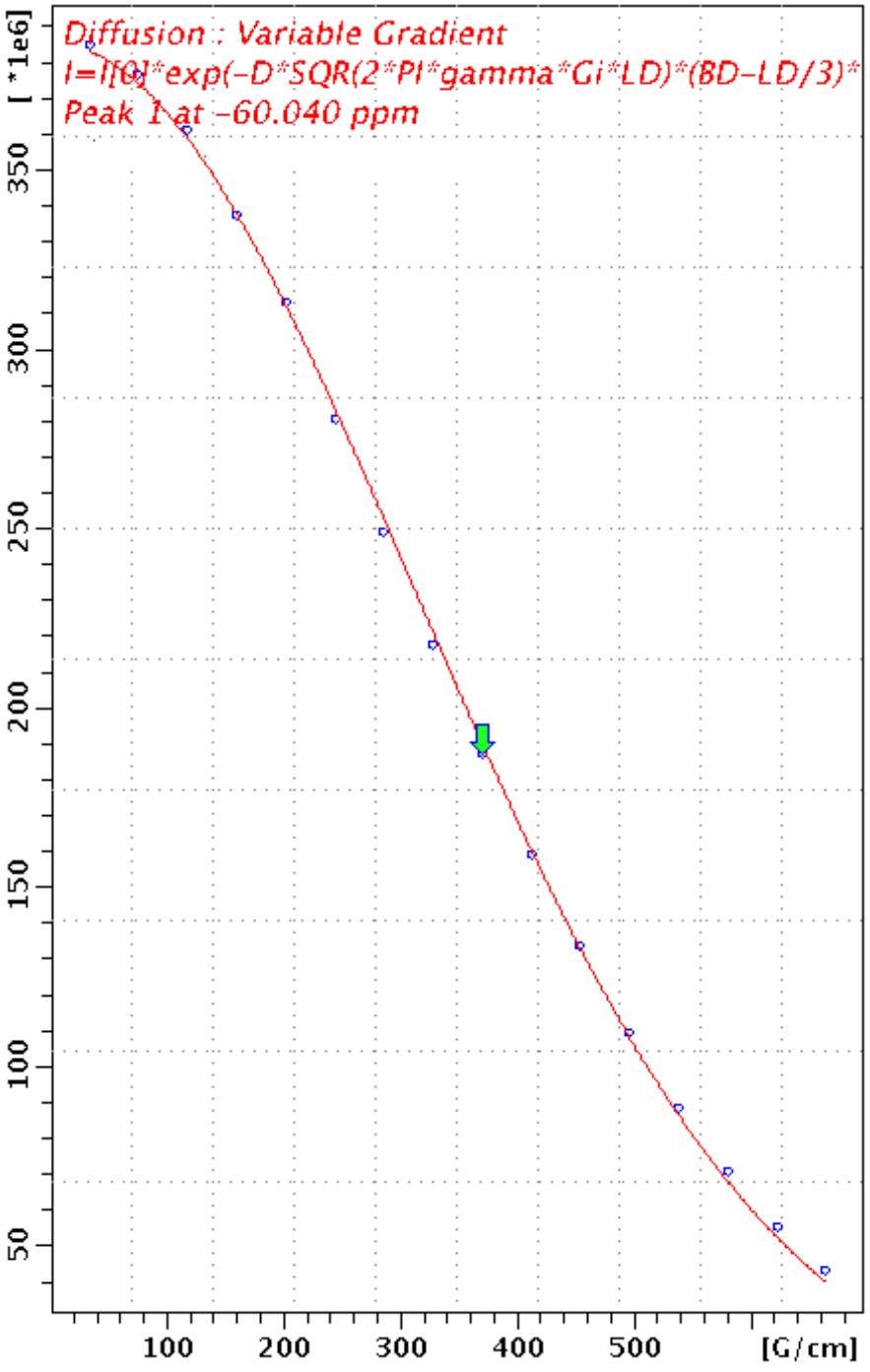

FIGURE B.7: RAW NMR of intensity of central isotropic peak as a function of Magentic field strength.The data shows the Stejskal-Tanner fit which is used to calculate diffusion coefficient. Experiment at 50°C - 35 wt% NaLAS and 4 wt % polymer.

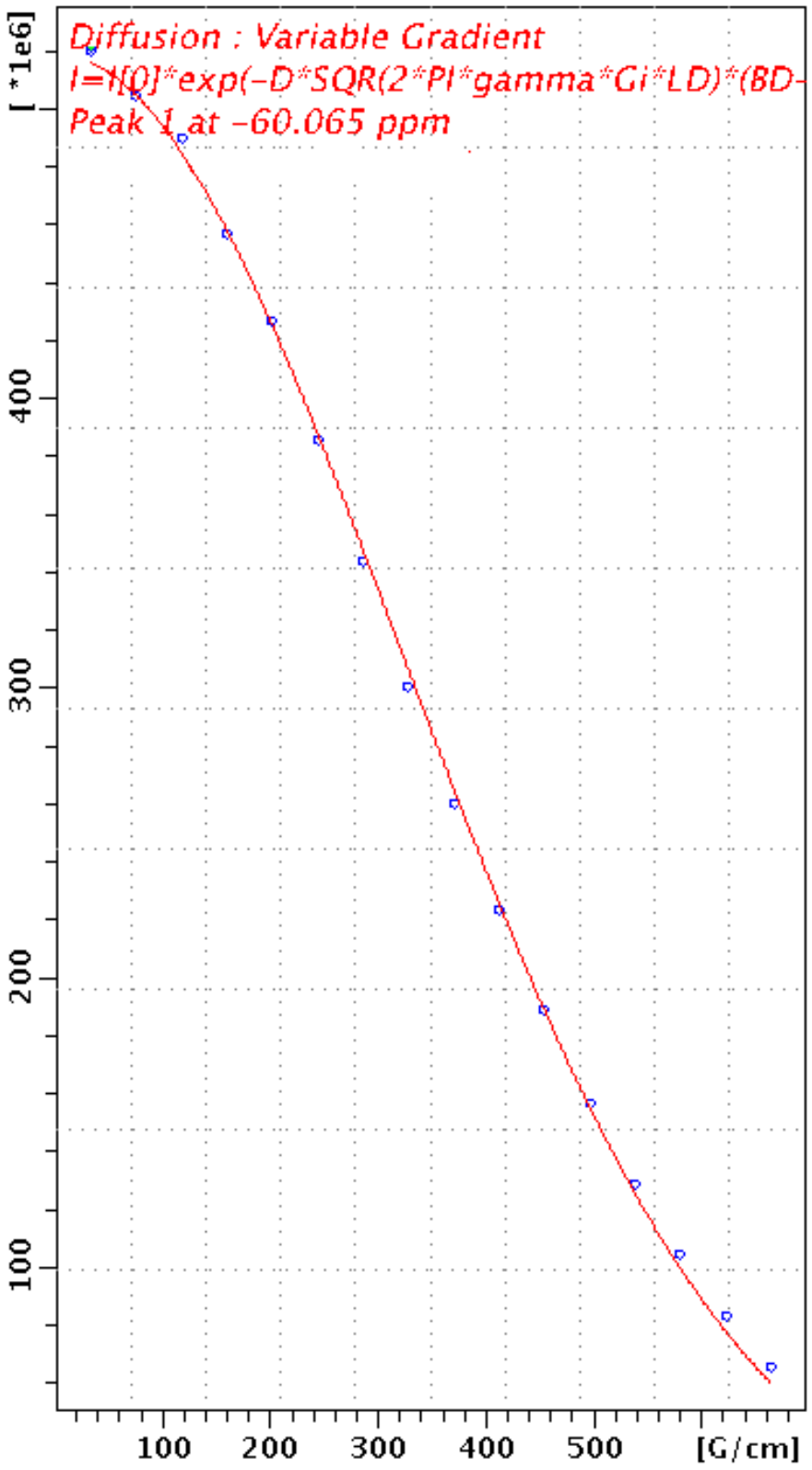

FIGURE B.8: RAW NMR of intensity of central isotropic peak as a function of Magentic field strength.The data shows the Stejskal-Tanner fit which is used to calculate diffusion coefficient. Experiment at 50°C - 35 wt% NaLAS and 6 wt % polymer.

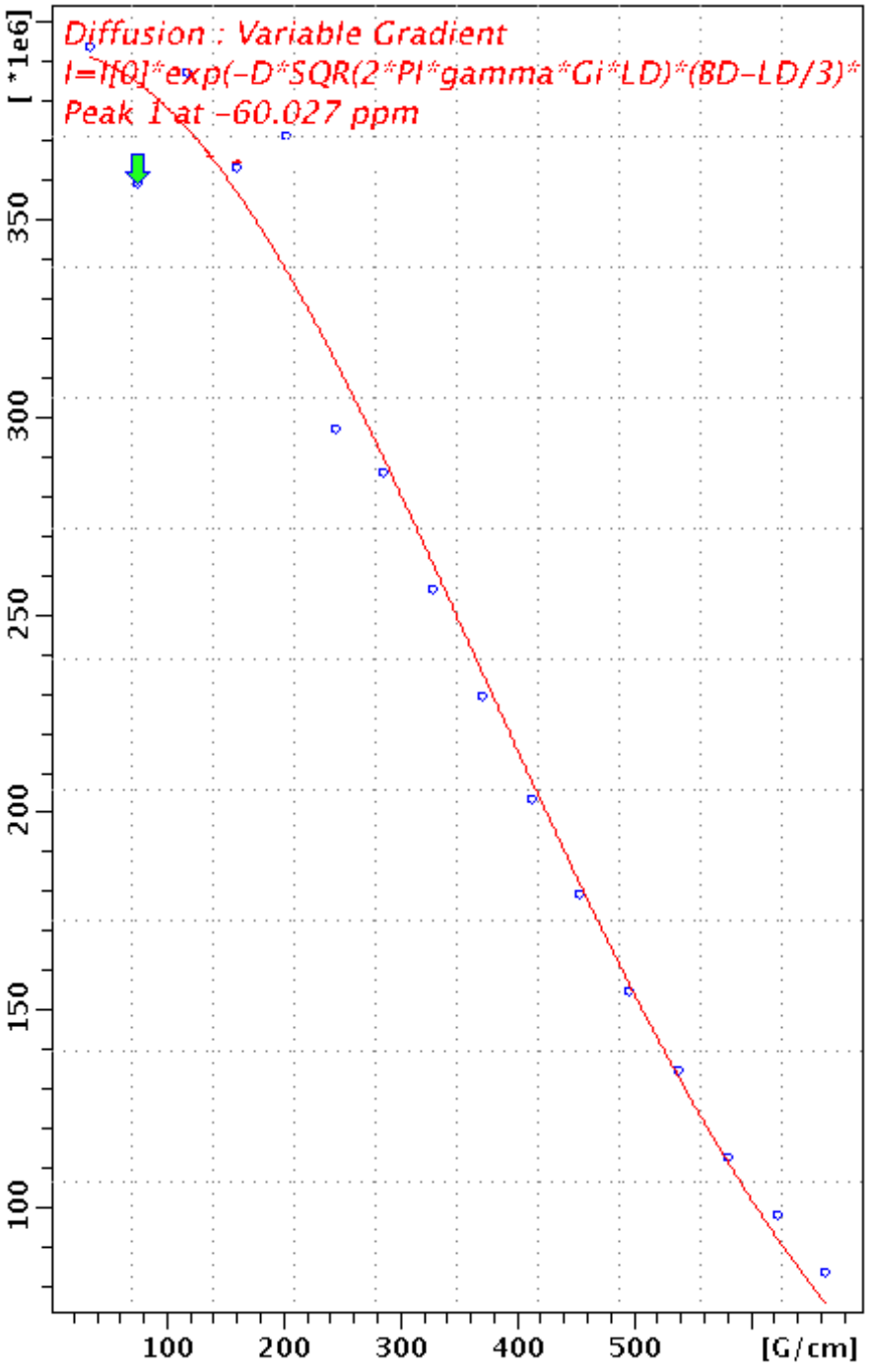

FIGURE B.9: RAW NMR of intensity of central isotropic peak as a function of Magentic field strength.The data shows the Stejskal-Tanner fit which is used to calculate diffusion coefficient. Experiment at 50°C - 35 wt% NaLAS and 8 wt % polymer.

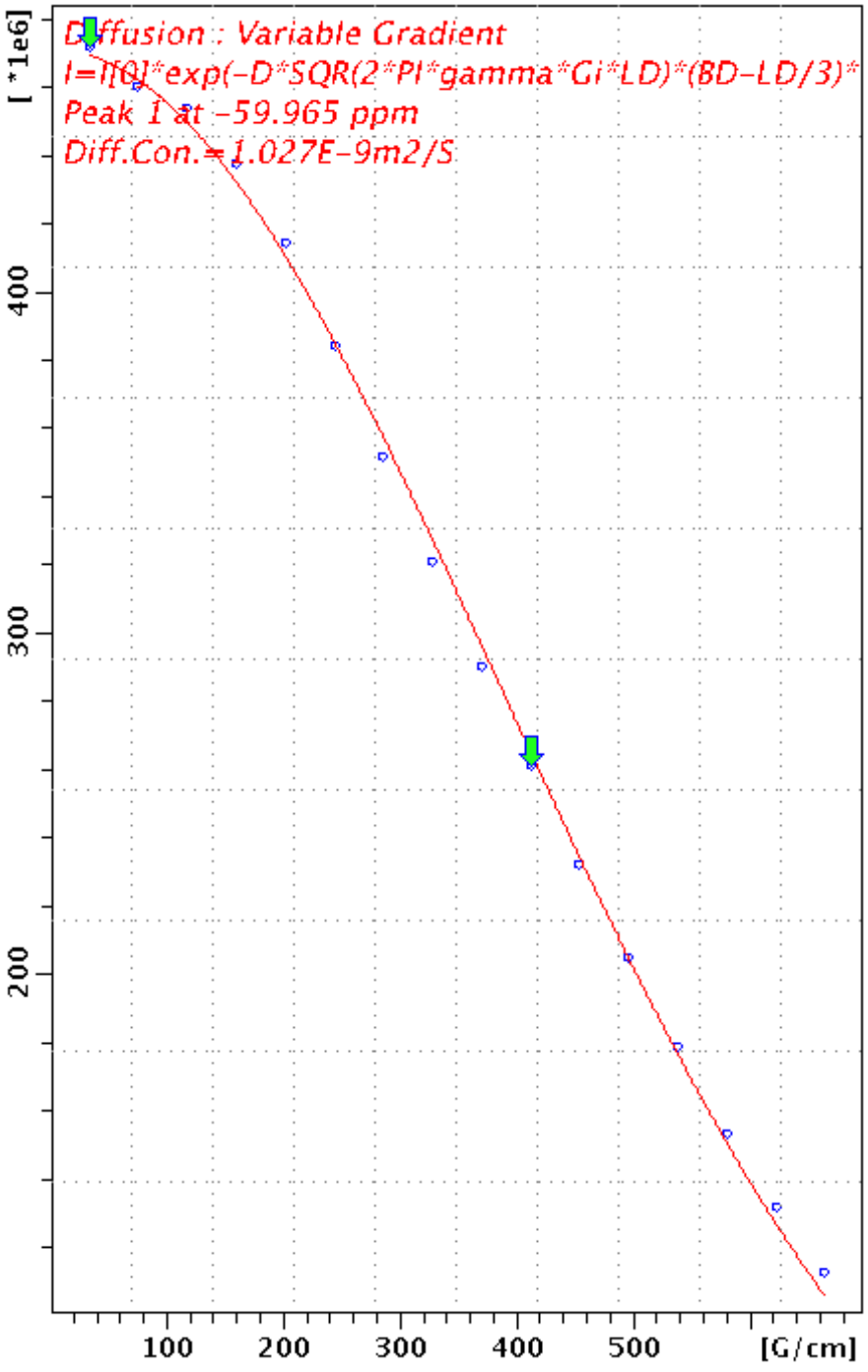

FIGURE B.10: RAW NMR of intensity of central isotropic peak as a function of magentic field strength. The data shows the Stejskal-Tanner fit which is used to calculate the diffusion coefficient. Experiment at 50°C - 35 wt% NaLAS and 1 wt % polymer.

Appendix C

Appendix C

Below is the raw PFG data for chapter 5.

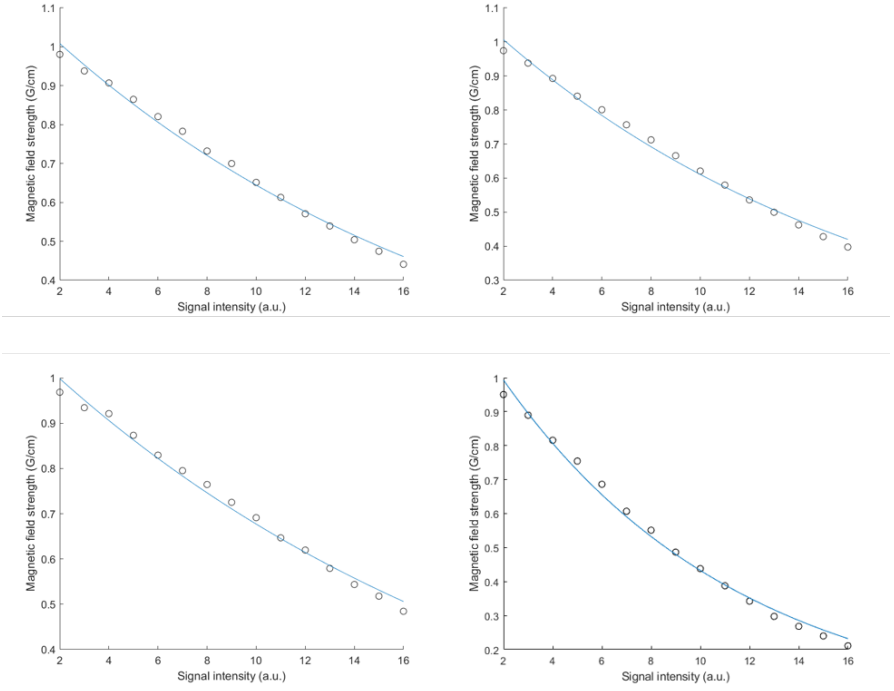

FIGURE C.1: The raw NMR PGSTE data collected at 50°C, with 16 data points for each experiment, and 4 scans were employed per data point, data shown is for the 4 experiments with Δ values of: (a): Δ=0.0025s, (b):Δ=0.0045s, (c):Δ=0.005s and (d):Δ=0.0075s. The sample had a surfactant concentration of 21.5 wt%, polymer concentration of 1 wt%, sodium sulphate concentration of 24 wt% and water concentration of 54.5 wt%. The sample was left in the NMR machine at 50°C for 15 minutes before analysis.

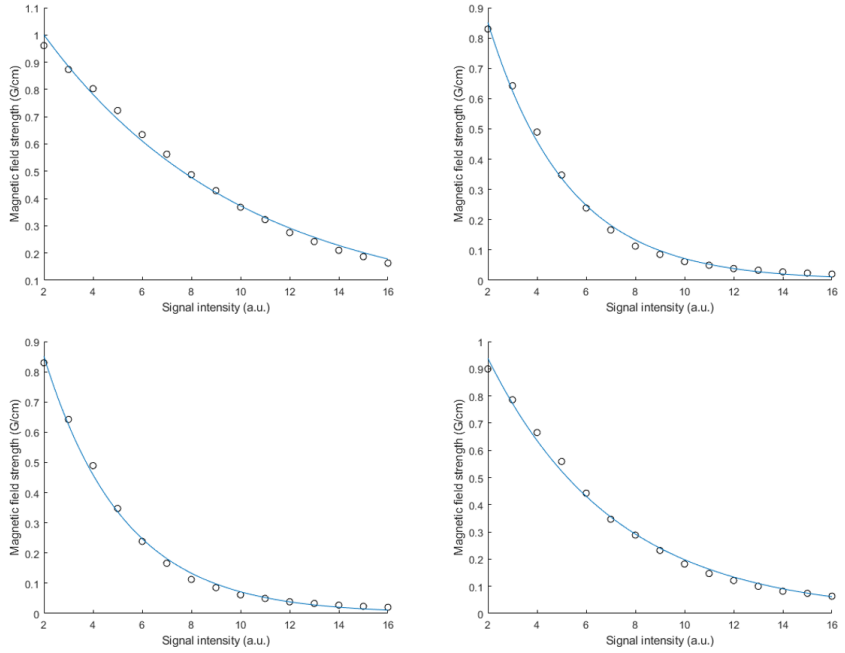

FIGURE C.2: The raw NMR PGSTE data collected at 50°C, with 16 data points for each experiment, and 4 scans were employed per data point, data shown is for the 4 experiments with Δ values of: (e): Δ=0.025s, (f): Δ=0.035s, (g): Δ=0.08s and (h): Δ=0.18s. The sample had a surfactant concentration of 21.5 wt%, polymer concentration of 1 wt%, sodium sulphate concentration of 24 wt% and water concentration of 54.5 wt%. The sample was left in the NMR machine at 50°C for 15 minutes before analysis.

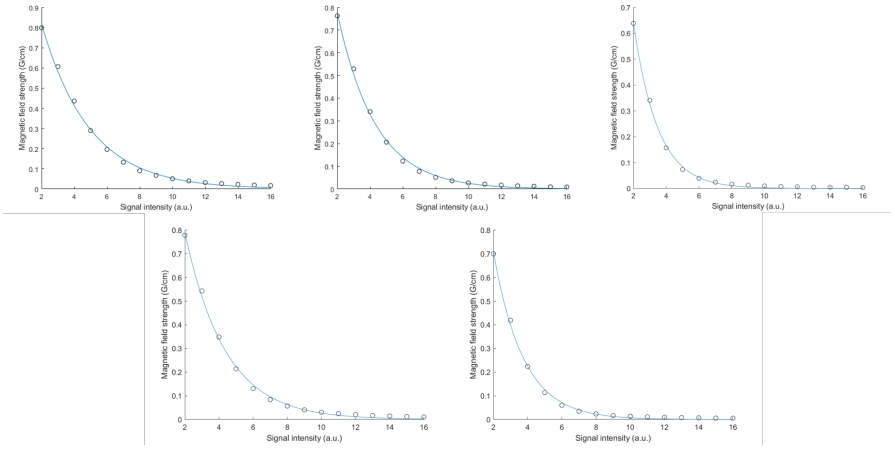

FIGURE C.3: The raw NMR PGSTE data collected at 50°C, with 16 data points for each experiment, and 4 scans were employed per data point, data shown is for the 4 experiments with Δ values of: (a): Δ=0.2s, (j): Δ=0.3s and (k): Δ=0.45s. The sample had a surfactant concentration of 21.5 wt%, polymer concentration of 1 wt%, sodium sulphate concentration of 24 wt% and water concentration of 54.5 wt%. The sample was left in the NMR machine at 50°C for 15 minutes before analysis.

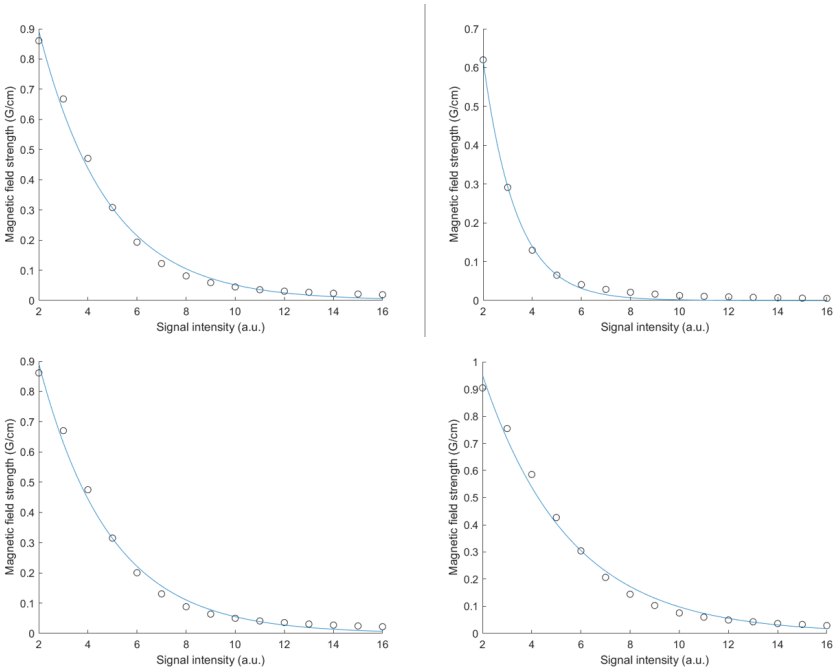

FIGURE C.4: The raw NMR PGSTE data collected at 50°C, with 16 data points for each experiment, and 4 scans were employed per data point, data shown is for the 4 experiments with Δ values of: (a): Δ=0.0025s, (b):Δ=0.0045s, (c):Δ=0.005s and (d):Δ=0.0075s. The sample had a surfactant concentration of 21.5 wt%, polymer concentration of 2 wt%, sodium sulphate concentration of 24 wt% and water concentration of 54.5 wt%. The sample was left in the NMR machine at 50°C for 15 minutes before analysis.

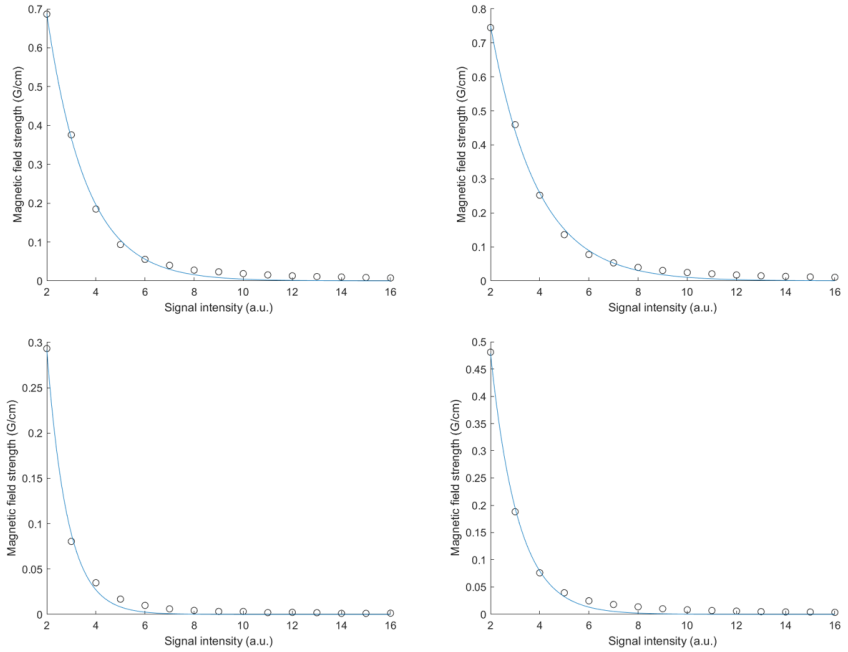

FIGURE C.5: The raw NMR PGSTE data collected at 50°C, with 16 data points for each experiment, and 4 scans were employed per data point, data shown is for the 4 experiments with Δ values of: (e): Δ=0.025s, (f): Δ=0.035s, (g): Δ=0.08s and (h): Δ=0.18s. The sample had a surfactant concentration of 21.5 wt%, polymer concentration of 2 wt%, sodium sulphate concentration of 24 wt% and water concentration of 54.5 wt%. The sample was left in the NMR machine at 50°C for 15 minutes before analysis.

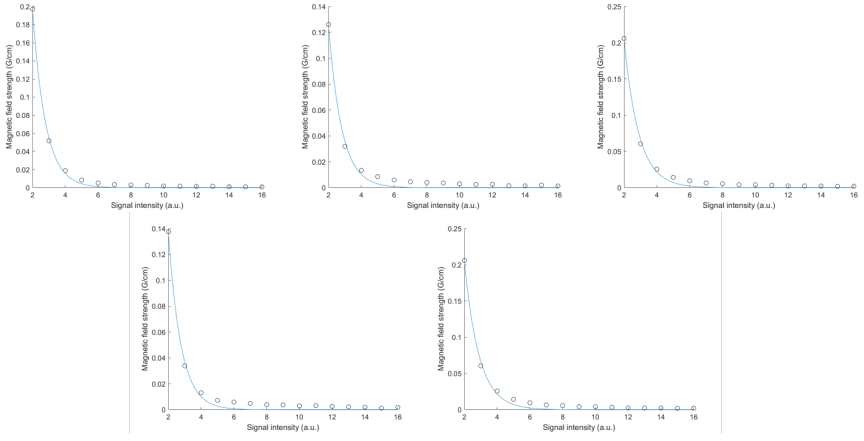

FIGURE C.6: The raw NMR PGSTE data collected at 50°C, with 16 data points for each experiment, and 4 scans were employed per data point, data shown is for the 4 experiments with Δ values of: (a): Δ=0.2s, (j): Δ=0.3s and (k): Δ=0.45s. The sample had a surfactant concentration of 21.5 wt%, polymer concentration of 2 wt%, sodium sulphate concentration of 24 wt% and water concentration of 54.5 wt%. The sample was left in the NMR machine at 50°C for 15 minutes before analysis.

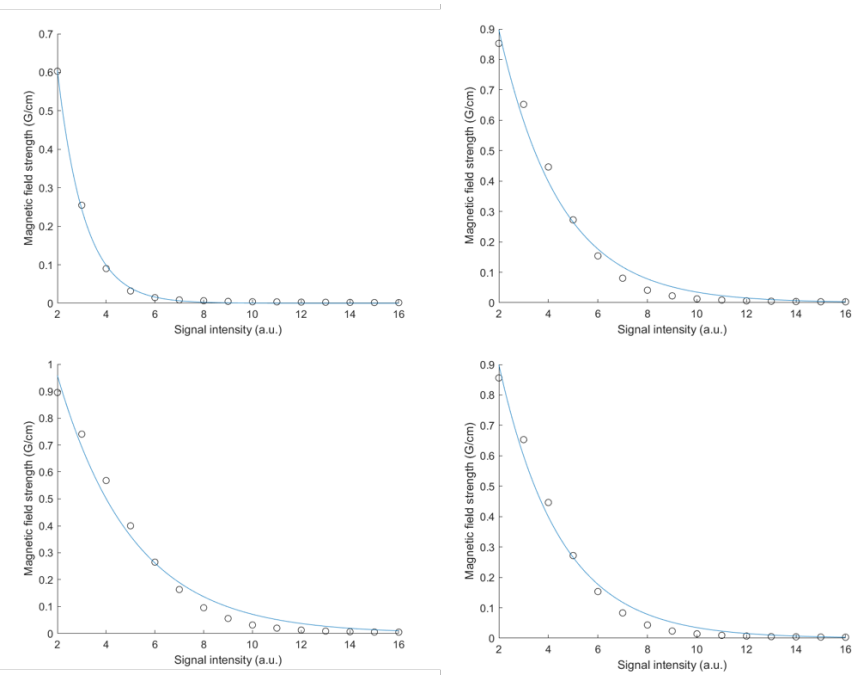

FIGURE C.7: The raw NMR PGSTE data collected at 50°C, with 16 data points for each experiment, and 4 scans were employed per data point, data shown is for the 4 experiments with Δ values of: (a): Δ=0.0025s, (b):Δ=0.0045s, (c):Δ=0.005s and (d):Δ=0.0075s. The sample had a surfactant concentration of 21.5 wt%, polymer concentration of 4 wt%, sodium sulphate concentration of 24 wt% and water concentration of 54.5 wt%. The sample was left in the NMR machine at 50°C for 15 minutes before analysis.

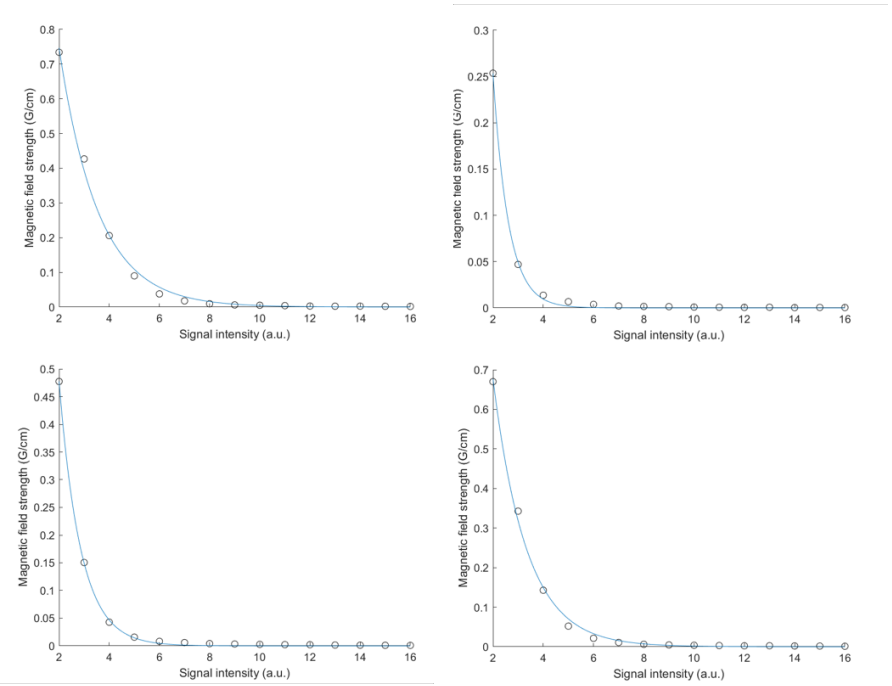

FIGURE C.8: The raw NMR PGSTE data collected at 50°C, with 16 data points for each experiment, and 4 scans were employed per data point, data shown is for the 4 experiments with Δ values of: (e): Δ=0.025s, (f): Δ=0.035s, (g): Δ=0.08s and (h): Δ=0.18s. The sample had a surfactant concentration of 21.5 wt%, polymer concentration of 4 wt%, sodium sulphate concentration of 24 wt% and water concentration of 54.5 wt%. The sample was left in the NMR machine at 50°C for 15 minutes before analysis.

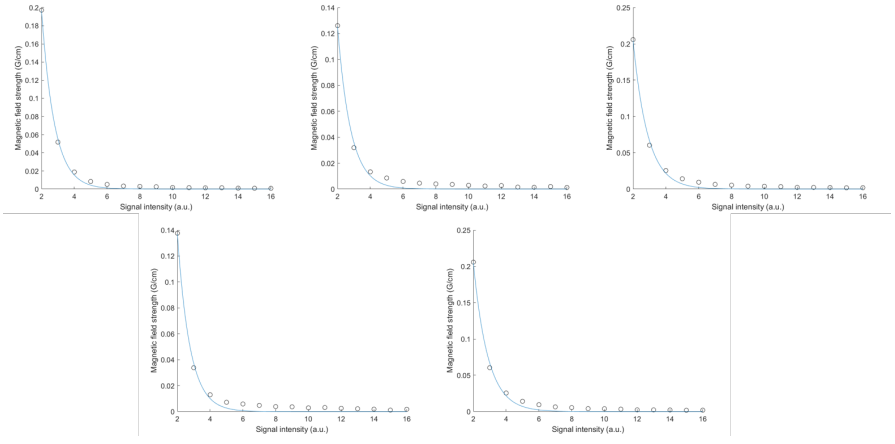

FIGURE C.9: The raw NMR PGSTE data collected at 50°C, with 16 data points for each experiment, and 4 scans were employed per data point, data shown is for the 4 experiments with Δ values of: (a): Δ=0.2s, (j): Δ=0.3s and (k): Δ=0.45s. The sample had a surfactant concentration of 21.5 wt%, polymer concentration of 4 wt%, sodium sulphate concentration of 24 wt% and water concentration of 54.5 wt%. The sample was left in the NMR machine at 50°C for 15 minutes before analysis.

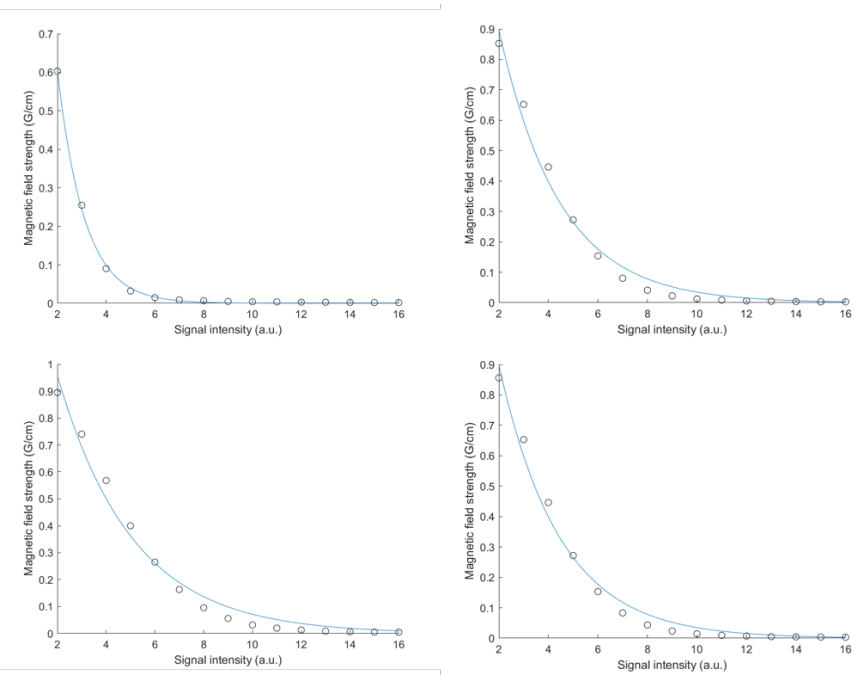

FIGURE C.10: The raw NMR PGSTE data collected at 50°C, with 16 data points for each experiment, and 4 scans were employed per data point, data shown is for the 4 experiments with Δ values of: (a): Δ=0.0025s, (b):Δ=0.0045s, (c):Δ=0.005s and (d):Δ=0.0075s. The sample had a surfactant concentration of 21.5 wt%, polymer concentration of 6 wt%, sodium sulphate concentration of 24 wt% and water concentration of 54.5 wt%. The sample was left in the NMR machine at 50°C for 15 minutes before analysis.

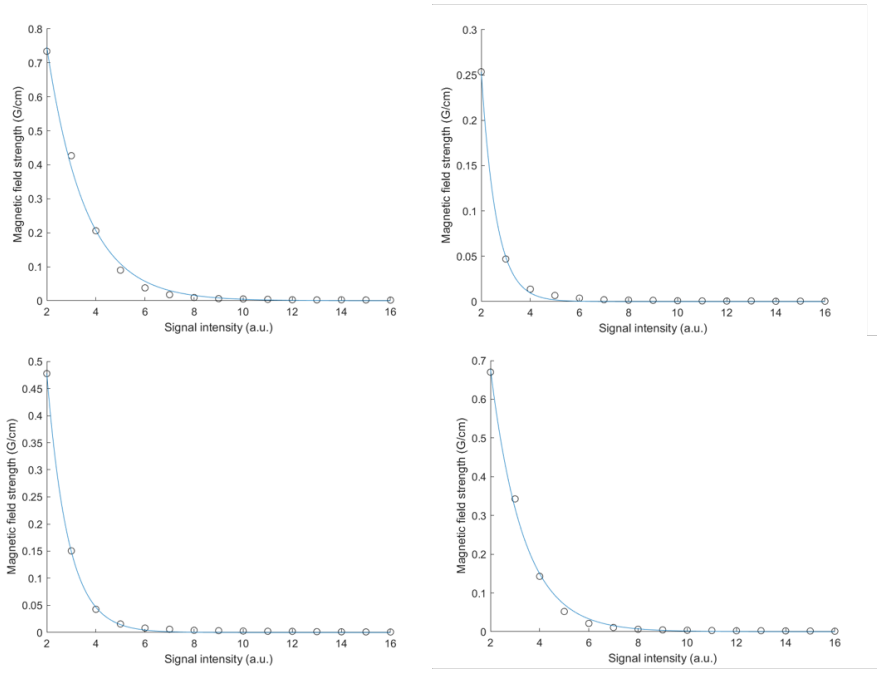

FIGURE C.11: The raw NMR PGSTE data collected at 50°C, with 16 data points for each experiment, and 4 scans were employed per data point, data shown is for the 4 experiments with Δ values of: (e): Δ=0.025s, (f): Δ=0.035s, (g): Δ=0.08s and (h): Δ=0.18s. The sample had a surfactant concentration of 21.5 wt%, polymer concentration of 6 wt%, sodium sulphate concentration of 24 wt% and water concentration of 54.5 wt%. The sample was left in the NMR machine at 50°C for 15 minutes before analysis.

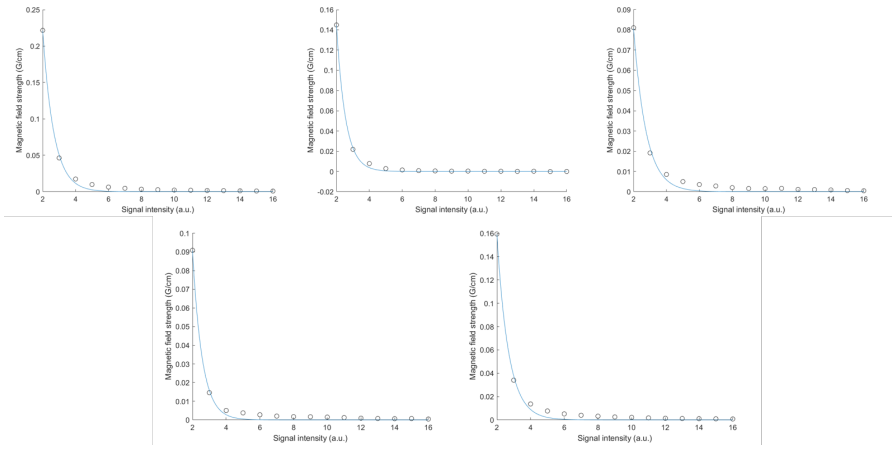

FIGURE C.12: The raw NMR PGSTE data collected at 50°C, with 16 data points for each experiment, and 4 scans were employed per data point, data shown is for the 4 experiments with Δ values of: (a): Δ=0.2s, (j): Δ=0.3s and (k): Δ=0.45s. The sample had a surfactant concentration of 21.5 wt%, polymer concentration of 6 wt%, sodium sulphate concentration of 24 wt% and water concentration of 54.5 wt%. The sample was left in the NMR machine at 50°C for 15 minutes before analysis.

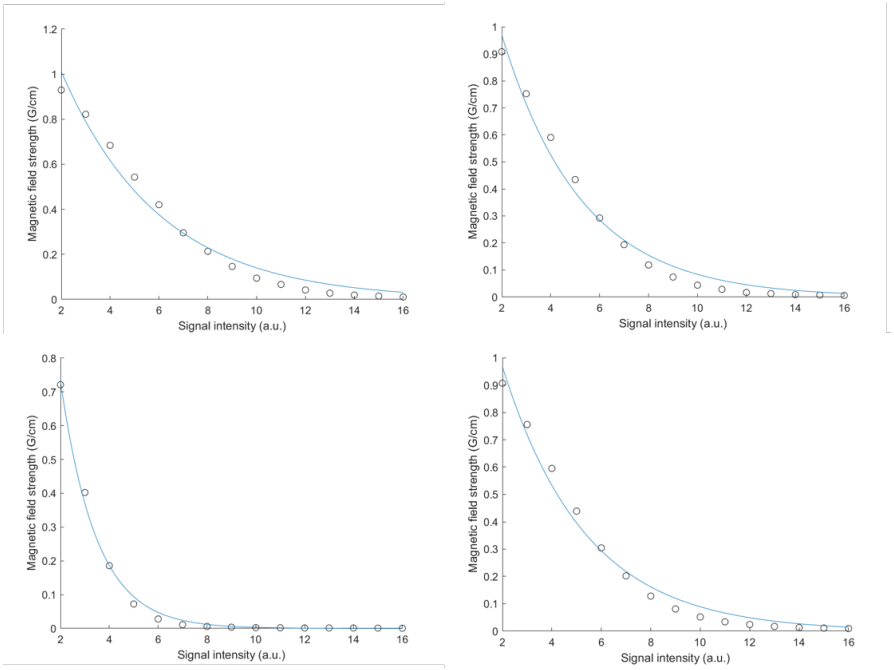

FIGURE C.13: The raw NMR PGSTE data collected at 50°C, with 16 data points for each experiment, and 4 scans were employed per data point, data shown is for the 4 experiments with Δ values of: (a): Δ=0.0025s, (b):Δ=0.0045s, (c):Δ=0.005s and (d):Δ=0.0075s. The sample had a surfactant concentration of 21.5 wt%, polymer concentration of 8 wt%, sodium sulphate concentration of 24 wt% and water concentration of 54.5 wt%. The sample was left in the NMR machine at 50°C for 15 minutes before analysis.

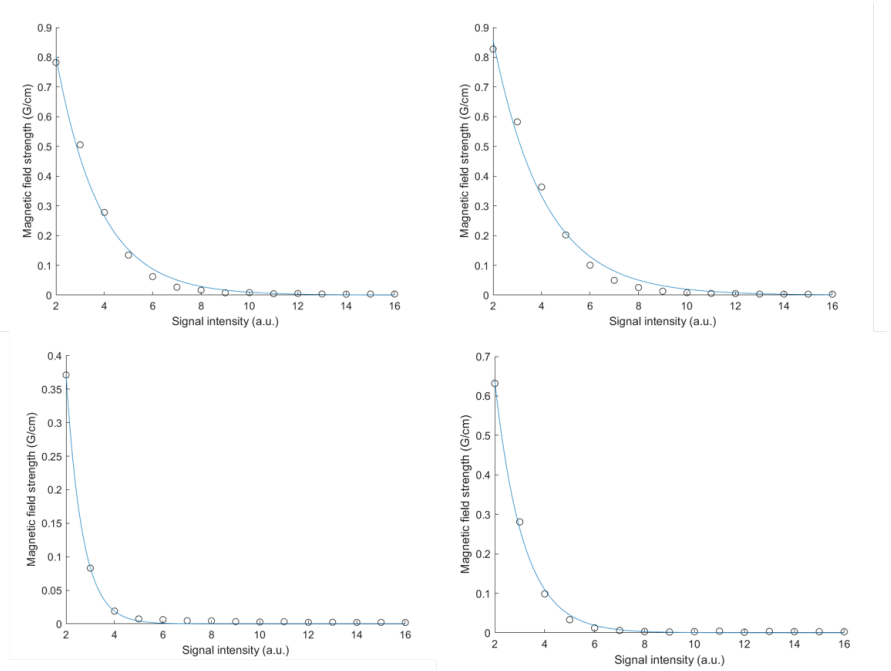

FIGURE C.14: The raw NMR PGSTE data collected at 50°C, with 16 data points for each experiment, and 4 scans were employed per data point, data shown is for the 4 experiments with Δ values of: (e): Δ=0.025s, (f): Δ=0.035s, (g): Δ=0.08s and (h): Δ=0.18s. The sample had a surfactant concentration of 21.5 wt%, polymer concentration of 8 wt%, sodium sulphate concentration of 24 wt% and water concentration of 54.5 wt%. The sample was left in the NMR machine at 50°C for 15 minutes before analysis.

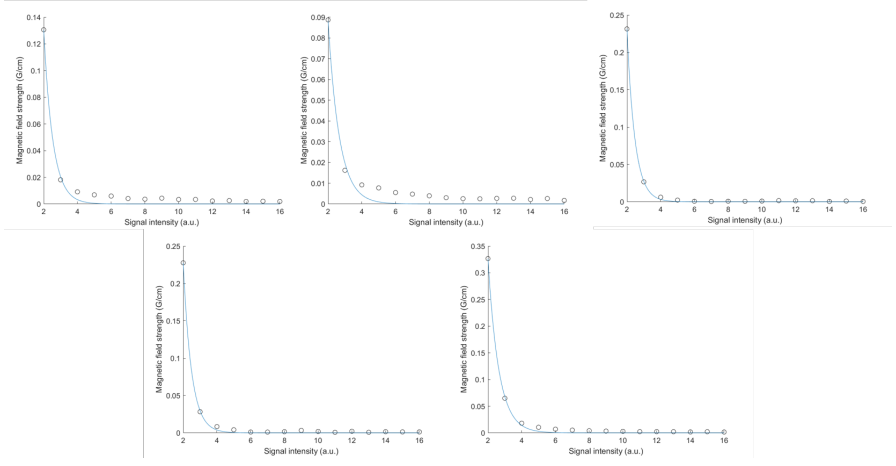

FIGURE C.15: The raw NMR PGSTE data collected at 50°C, with 16 data points for each experiment, and 4 scans were employed per data point, data shown is for the 4 experiments with Δ values of: (a): Δ=0.2s, (j): Δ=0.3s and (k): Δ=0.45s. The sample had a surfactant concentration of 21.5 wt%, polymer concentration of 8 wt%, sodium sulphate concentration of 24 wt% and water concentration of 54.5 wt%. The sample was left in the NMR machine at 50°C for 15 minutes before analysis.

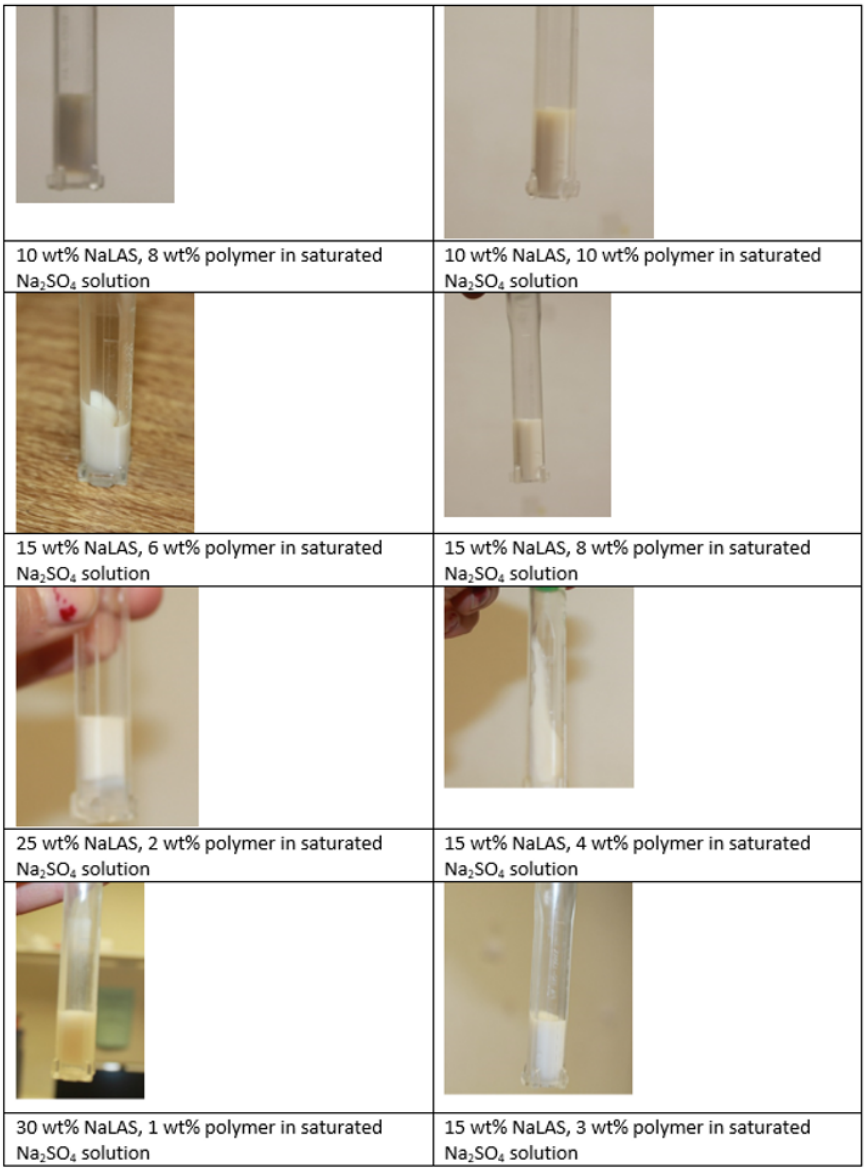

FIGURE C.16: Various concentrations of surfactant and polymer in saturated sodium sulphate solution to show the phase transitions in Figure 5.3. This is following 2 hour 17 minutes of centrifugation of sample at 4000 RPM at 50°C.

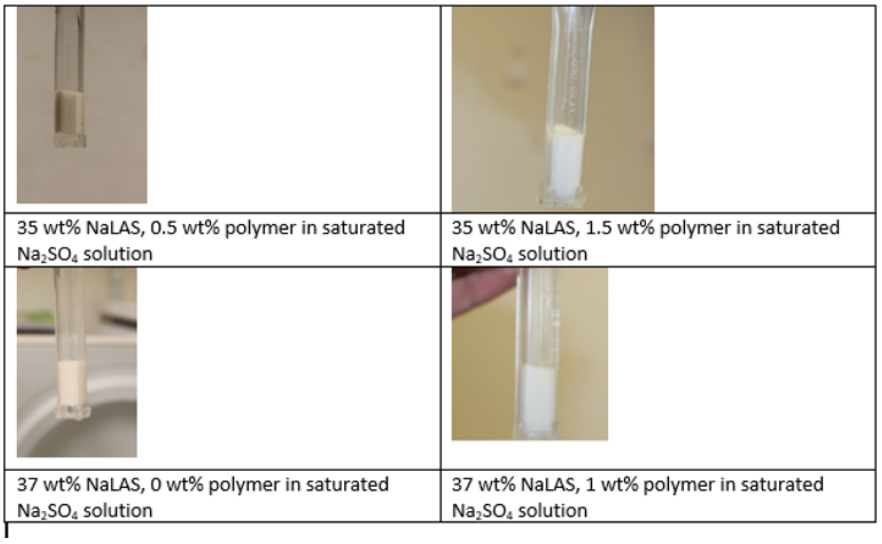

FIGURE C.17: Various concentrations of surfactant and polymer in saturated sodium sulphate solution to show the phase transitions in Figure 5.3. This is following 2 hour 17 minutes of centrifugation of sample at 4000 RPM at 50°C.

Bibliography

[1] T. Mori, J. P. Hill, Q. Ji, K. Ariga, L. K. Shrestha, and M. Ramanathan, "Amphiphile nanoarchitectonics: from basic physical chemistry to advanced applications," *Physical Chemistry Chemical Physics*, vol. 15, no. 26, p. 10580, 2013.

[2] C. Richards, G. J. T. Tiddy, and S. Casey, "Lateral Phase Separation Gives Multiple Lamellar Phases in a Binary Surfactant/Water System:˜ The Phase Behavior of Sodium Alkyl Benzene Sulfonate/Water Mixtures," *Langmuir*, vol. 23, pp. 467–474, jan 2007.

[3] A. Sein, J. B. F. N. Engberts, E. van der Linden, and J. C. van de Pas, "Lyotropic Phases of Dodecylbenzenesulfonates with Different Counterions in Water," *Langmuir*, vol. 12, no. 12, pp. 2913–2923, 1996.

[4] M. Rosen, *Surfactants and interfacial phenomena*. Hoboken, N.J: Wiley, 2012.

[5] J. A. Stewart, "Engineering the properties of spray-dried detergent granules," pp. 1–249, 2008.

[6] M. E. Smith and J. H. Strange, "NMR techniques in materials physics: a review," *Measurement Science and Technology*, vol. 7, pp. 449–475, Apr. 1996.

[7] T. R. Molugu, X. Xu, A. Leftin, S. Lope-Piedrafita, G. V. Martinez, H. I. Petrache, and M. F. Brown, "Solid-state deuterium NMR spectroscopy of membranes," in *Modern Magnetic Resonance*, pp. 1–23, Springer International Publishing, 2017.

[8] C. Calahorro, J. Muñoz, M. Berjano, A. Guerrero, and C. Gallegos, "Flow behavior of sucrose stearate/water systems," *Journal of the American Oil Chemists Society*, vol. 69, pp. 660–666, July 1992.

[9] A. B. Dhanikula, M. Lafleur, and J.-C. Leroux, "Characterization and in vitro evaluation of spherulites as sequestering vesicles with potential application in drug detoxification," *Biochimica et Biophysica Acta (BBA) - Biomembranes*, vol. 1758, pp. 1787–1796, Nov. 2006.

[10] I. Dierking, *Textures of Liquid Crystals*. Advances in Electrochemical Sciences and Engineering Series, Wiley-VCH, 2003.

[11] T. D. Le, U. Olsson, K. Mortensen, J. Zipfel, and W. Richtering, "Non-ionic amphiphilic bilayer structures under shear," *Langmuir*, vol. 17, no. 4, pp. 999–1008, 2001.

[12] H. Wennerström and D. M. Anderson, "Difference Versus Gaussian Curvature Energies; Monolayer Versus Bilayer Curvature Energies; Applications to Vesicle Stability," pp. 137–152, 1993.

[13] J. Stewart, A. Saiani, A. Bayly, and G. Tiddy, "The phase behaviour of lyotropic liquid crystals in linear alkylbenzene sulphonate (las) systems," *Colloids and Surfaces A: Physicochemical and Engineering Aspects*, vol. 338, no. 1-3, pp. 155–161, 2009.

[14] D. Myers, *Surfactant science and technology*. Hoboken, N.J: J. Wiley, 2006.

[15] J. N. Israelachvil, D. J. Mitchell, B. W. Ninham, J. N. Israelachvili, D. J. Mitchell, and B. W. Ninham, "Theory of Self-Assembly of Hydrocarbon Amphiphiles into Micelles and Bilayers View Online," *J. Chem. Soc., Faraday Trans. 2*, vol. 72, pp. 1525–1568, 1976.

[16] K. Mittal, *Surfactants in Solution : Volume 4*. Springer US, 1987.

[17] L. Maibaum, A. R. Dinner, and D. Chandler, "Micelle Formation and the Hydrophobic Effect," pp. 1–13, 2004.

[18] D. Stigter, "Micelle Formation by Ionic Surfactants .," *Journal of colloid and Interface Science*, vol. 47, no. 2, pp. 473–482, 1974.

[19] T. Tadros, *Applied Surfactants: Principles and Applications*. Wiley, 2006.

[20] A. M. F. Neto, *The Physics of Lyotropic Liquid Crystals: Phase Transitions and Structural Properties (Monographs on the Physics and Chemistry of Materials)*. Oxford University Press, apr 2005.

[21] G. J. Tiddy, "Surfactant-water liquid crystal phases," *Physics Reports*, vol. 57, no. 1, pp. 1–46, 1980.

[22] R. Aveyard, B. P. Binks, P. D. I. Fletcher, and J. R. Macnab, "The Effect of Temperature on the Adsorption of Dodecane onto Nonionic and Ionic Surfactant Monolayers at the Air-Water Surface," *Berichte der Bunsengesellschaft für physikalische Chemie*, vol. 100, no. 3, pp. 224–231, 2012.

[23] P. J. Collings, *Liquid Crystals*. Princeton University Press, dec 1990.

[24] K. Ogino and M. Abe, *Mixed Surfactant Systems*. Surfactant Science, Taylor & Francis, 1992.

[25] S. Singh and D. Dunmur, *Liquid Crystals: Fundamentals*. World Scientific, 2002.

[26] Q. Li, *Liquid Crystals Beyond Displays: Chemistry, Physics, and Applications*. Wiley, 2012.

[27] T. M. Ferreira, B. Medronho, R. W. Martin, and D. Topgaard, "Segmental order parameters in a nonionic surfactant lamellar phase studied with1H-13C solid-state NMR," *Physical Chemistry Chemical Physics*, vol. 10, no. 39, pp. 6033–6038, 2008.

[28] O. Edholm, "order parameters in hydrocarbon chains," *chemical physics*, vol. 65, pp. 259–270, 1982.

[29] T. J. Piggot, J. R. Allison, R. B. Sessions, and J. W. Essex, "On the calculation of acyl chain order parameters from lipid simulations," *Journal of Chemical Theory and Computation*, vol. 13, pp. 5683–5696, Oct. 2017.

[30] J. T. Tiddy, P. Sunlight, and Q. R. East, "Optical Microscopy and Nuclear Magnetic Resonance Studies of Mesophases Formed at Compositions between Hexagonal and Lamellar Phases in Sodium n-Alkanoate + Water Mixtures and Related Surfactant Systems," *J.Chem.Soc., Faraday Trans.*, 1983.

[31] P. Somasundaran, *Encyclopedia of Surface and Colloid Science, Second Edition - Eight-Volume Set (Print)*. Encyclopedia of Surface and Colloid Science, Taylor & Francis, 2006.

[32] A. Samad, Y. Sultana, and M. Aqil, "Liposomal Drug Delivery Systems: An Update Review," *Current Drug Delivery*, vol. 4, no. 4, pp. 297–305, 2007.

[33] L. Sercombe, T. Veerati, F. Moheimani, S. Y. Wu, A. K. Sood, and S. Hua, "Advances and challenges of liposome assisted drug delivery," *Frontiers in Pharmacology*, vol. 6, Dec. 2015.

[34] U. Pleyer, D. Groth, B. Hinz, O. Keil, E. Bertelmann, P. Rieck, and R. Reszka, "Efficiency and toxicity of liposome-mediated gene transfer to corneal endothelial cells," *Experimental Eye Research*, vol. 73, pp. 1–7, July 2001.

[35] S. Šegota and D. urd ica Težak, "Spontaneous formation of vesicles," *Advances in Colloid and Interface Science*, vol. 121, no. 1-3, pp. 51–75, 2006.

[36] H. Deuling and W. Helfrich, "The curvature elasticity of fluid membranes : A catalogue of vesicle shapes," *Journal de Physique*, vol. 37, no. 11, pp. 1335–1345, 2007.

[37] A. Iglic, *Advances in planar lipid bilayers and liposomes*. Waltham, Massachusetts: Academic Press, 2014.

[38] T. Tadros, *Self-Organized Surfactant Structures*. Weinheim: Wiley-VCH, 2011.

[39] R. Mortier, M. Fox, and S. Orszulik, *Chemistry and Technology of Lubricants*. SpringerLink: Springer e-Books, Springer Netherlands, 2011.

[40] J. A. Stewart, A. Saiani, A. Bayly, and G. J. Tiddy, "The phase behaviour of lyotropic liquid crystals in linear alkylbenzene sulphonate (LAS) systems," *Colloids and Surfaces A: Physicochemical and Engineering Aspects*, vol. 338, no. 1-3, pp. 155–161, 2009.

[41] J. Ockelford, B. A. Timimi, K. S. Narayan, and G. J. T. Tiddy, "An upper critical point in a lamellar liquid crystalline phase," *The Journal of Physical Chemistry*, vol. 97, no. 26, pp. 6767–6769, 1993.

[42] D. Carrière, M. Dubois, M. Schönhoff, T. Zemb, and H. Moehwald, "Counter-ion activity and microstructure in polyelectrolyte complexes as determined by osmotic pressure measurements," *Physical Chemistry Chemical Physics*, vol. 8, p. 3141, 06 2006.

[43] D. Evans, *The colloidal domain : where physics, chemistry, biology, and technology meet*. New York: Wiley-VCH, 1999.

[44] J. van de Pas, C. Buytenhek, and L. Brouwn, "The effects of salts and surfactants on the physical stability of lamellar liquid-crystalline systems," *Recueil des Travaux Chimiques des Pays-Bas*, vol. 113, pp. 231–236, Sept. 2010.

[45] J. Beunen and E. Ruckenstein, "The effect of salting out and micellization on interfacial tension," *Advances in Colloid and Interface Science*, vol. 16, pp. 201–231, July 1982.

[46] A. M. Hyde, S. L. Zultanski, J. H. Waldman, Y.-L. Zhong, M. Shevlin, and F. Peng, "General principles and strategies for salting-out informed by the hofmeister series," *Organic Process Research & Development*, vol. 21, pp. 1355–1370, Aug. 2017.

[47] J. N. Israelachvili and H. Wennerstroem, "Hydration or steric forces between amphiphilic surfaces?," *Langmuir*, vol. 6, pp. 873–876, Apr. 1990.

[48] A. Yavari, A. Inoue, D. Morris, and R. Schulz, *Journal of Metastable and Nanocrystalline Materials: Winter e-volume 2005*. Journal of Metastable and Nanocrystalline Materials, Trans Tech Publications Limited, 2005.

[49] H. Mollet, A. Grubenmann, and H. Payne, *Formulation Technology: Emulsions, Suspensions, Solid Forms*. Wiley, 2008.

[50] T. Tadros, "Surfactants," in *Encyclopedia of Colloid and Interface Science*, pp. 1242–1290, Springer Berlin Heidelberg, 2013.

[51] M. S. Bakshi, "Polymer-induced incompatibility in the mixed micelle formation of cationic surfactants with bulky polar head groups," *Journal of Surfactants and Detergents*, vol. 4, pp. 297–302, July 2001.

[52] E. F. Marques and B. F. B. Silva, "Surfactants, phase behavior," in *Encyclopedia of Colloid and Interface Science*, pp. 1290–1333, Springer Berlin Heidelberg, 2013.

[53] L. Brannon-Peppas, *Interactions of surfactants with polymers and proteins*, vol. 26. 1993.

[54] J. T. Brooks and M. E. Cates, "The role of added polymer in dilute lamellar surfactant phases," *The Journal of Chemical Physics*, vol. 99, pp. 5467–5480, Oct. 1993.

[55] P. Sierro and D. Roux, "Structure of a lyotropic lamellar phase under shear," *Physical Review Letters*, vol. 78, no. 8, pp. 1496–1499, 1997.

[56] J. Gustafsson, G. Oradd, M. Nyden, P. Hansson, and M. Almgren, "Defective Lamellar Phases and Micellar Polymorphism in Mixtures of Glycerol Monooleate and Cetyltrimethylammonium Bromide in Aqueous Solution," *Langmuir*, vol. 14, no. 18, pp. 4987–4996, 2002.

[57] A. Zilman and R. Granek, "Undulation instability of lamellar phases under shear: A mechanism for onion formation?," *The European Physical Journal B*, vol. 11, pp. 593–608, Oct. 1999.

[58] R. Laughlin, "Equilibrium vesicles: fact or fiction?," *Colloids and Surfaces A: Physicochemical and Engineering Aspects*, vol. 128, pp. 27–38, Aug. 1997.

[59] G. K. Auernhammer, H. R. Brand, and H. Pleiner, "The undulation instability in layered systems under shear flow - a simple model," *Rheologica Acta*, vol. 39, pp. 215–222, Aug. 2000.

[60] T. M. Ferreira, D. Bernin, and D. Topgaard, "NMR studies of nonionic surfactants," in *Annual Reports on NMR Spectroscopy*, pp. 73–127, Elsevier, 2013.

[61] S. A. Smith, W. E. Palke, and J. T. Gerig, "The hamiltonians of NMR. part i," *Concepts in Magnetic Resonance*, vol. 4, pp. 107–144, Apr. 1992.

[62] K. Schmidt-Rohr and H. W. Spiess, *Multidimensional Solid-State NMR and Polymers (Anthropology, Culture and Society (Hardcover))*. Academic Press, 2012.

[63] B. Blümich and M. S. Conradi, "NMR imaging of materials," *Review of Scientific Instruments*, vol. 73, pp. 232–232, jan 2002.

[64] J. Keeler, *Understanding NMR Spectroscopy*. Wiley, 2011.

[65] J. Keeler, *Understanding NMR spectroscopy*. Chichester, U.K: John Wiley and Sons, 2010.

[66] A. Abragam, *Principles of Nuclear Magnetism (International Series of Monographs on Physics)*. Clarendon Press, 1983.

[67] K. Jozef and M. Lena, *Nuclear Spin Relaxation in Liquids*. CRC Press, dec 2017.

[68] D. Doddrell, V. Glushko, and A. Allerhand, "Theory of nuclear overhauser enhancement and 13c–1h dipolar relaxation in proton-decoupled carbon-13 NMR spectra of macromolecules," *The Journal of Chemical Physics*, vol. 56, pp. 3683–3689, apr 1972.

[69] R. Kimmich, *NMR: Tomography, Diffusometry, Relaxometry*. Springer Berlin Heidelberg, 2012.

[70] M. Levitt, *Spin Dynamics: Basics of Nuclear Magnetic Resonance*. Wiley, 2013.

[71] R. Dong and W. Scientific, *Nuclear Magnetic Resonance Spectroscopy of Liquid Crystals*. World Scientific Publishing Company, 2010.

[72] A. Derome and J. Baldwin, *Modern NMR Techniques for Chemistry Research*. Tetrahedron Organic Chemistry, Elsevier Science, 2013.

[73] H. Mehrer, *Diffusion in Solids: Fundamentals, Methods, Materials, Diffusion-Controlled Processes*. Springer Series in Solid-State Sciences, Springer Berlin Heidelberg, 2007.

[74] R. Valiullin and I. Furó, "Phase separation of a binary liquid mixture in porous media studied by nuclear magnetic resonance cryoporometry," *The Journal of Chemical Physics*, vol. 116, pp. 1072–1076, Jan. 2002.

[75] R. Carlton, *Pharmaceutical Microscopy*. SpringerLink : Bücher, Springer New York, 2011.

[76] J. Mertz, *Introduction to Optical Microscopy*. Cambridge University Press, 2019.

[77] I. Scanning Electron Microscopy, *Scanning Electron Microscopy*. Scanning Electron Microscopy, Incorporated, 1986.

[78] J. Goldstein, D. Newbury, J. Michael, N. Ritchie, J. Scott, and D. Joy, *Scanning Electron Microscopy and X-Ray Microanalysis*. Springer New York, 2017.

[79] P. Echlin, *Handbook of Sample Preparation for Scanning Electron Microscopy and X-Ray Microanalysis*. Springer US, 2011.

[80] H. Schnablegger and Y. Singh, "SAXS analysis," in *The SAXS Guide*, pp. 1–99, Anton Paar GmbH, 2011.

[81] K. Aligizaki, *Pore Structure of Cement-Based Materials: Testing, Interpretation and Requirements*. Modern Concrete Technology, Taylor & Francis, 2005.

[82] K. Holmberg, D. Shah, and M. Schwuger, *Handbook of applied surface and colloid chemistry*. No. v. 1 in Handbook of Applied Surface and Colloid Chemistry, Wiley, 2002.

[83] H. Barnes, K. John Fletcher Hutton, J. Hutton, and K. Walters, *An Introduction to Rheology*. Annals of Discrete Mathematics, Elsevier Science, 1989.

[84] A. Malkin, A. Malkin, and A. Isayev, *Rheology: Concepts, Methods and Applications*. ChemTec, 2006.

[85] L. Gargallo, D. Dadić, and F. Martínez-Piña, "Phase separation behaviour of polymers in water. Temperature and surfactant effect," *European Polymer Journal*, vol. 33, no. 10-12, pp. 1767–1769, 1997.

[86] P. D. Patel and W. B. Russel, "An experimental study of aqueous suspensions containing dissolved polymer. A. Phase separation," *Journal of Colloid And Interface Science*, vol. 131, no. 1, pp. 192–200, 1989.

[87] S. M. Clegg, D. G. Hall, I. D. Robb, and P. A. Williams, "Phase separation of a polycarboxylate at high ionic strength," *Berichte der Bunsengesellschaft für physikalische Chemie*, vol. 100, no. 6, pp. 780–783, 1996.

[88] S. Safran, T. Kuhl, and J. Israelachvili, "Polymer-induced membrane contraction, phase separation, and fusion via marangoni flow," *Biophysical Journal*, vol. 81, pp. 659–666, Aug. 2001.

[89] B. Medronho, C. Schmidt, U. Olsson, and M. G. Miguel, "Size determination of shear-induced multilamellar vesicles by rheo-nmr spectroscopy," *Langmuir*, vol. 26, no. 3, pp. 1477–1481, 2010.

[90] A. B. Farimani and N. R. Aluru, "Spatial diffusion of water in carbon nanotubes: From fickian to ballistic motion," *The Journal of Physical Chemistry B*, vol. 115, pp. 12145–12149, Oct. 2011.

[91] J. van de Pas and C. Buytenhek, "The effects of free polymers on osmotic compression, depletion flocculation and fusion of lamellar liquid-crystalline droplets," *Colloids and Surfaces*, vol. 68, no. 1-2, pp. 127–139, 1992.

[92] D. M. Leneveu, R. P. Rand, and V. A. Pargesian, "Measurement of forces between lecithin bilayers," *Nature*, vol. 259, no. 5544, pp. 601–603, 1976.

[93] P. R. Cullis and M. J. Hope, "Effects of fusogenic agent on membrane structure of erythrocyte ghosts and the mechanism of membrane fusion," *Nature*, vol. 271, no. 5646, p. 672–674, 1978.

[94] J. A. Stewart, A. Saiani, A. Bayly, and G. J. Tiddy, "Phase behavior of lyotropic liquid crystals in linear alkylbenzene sulphonate (LAS) systems in the presence of dilute and concentrated electrolyte," *Journal of Dispersion Science and Technology*, vol. 32, no. 12, pp. 1700–1710, 2011.

[95] J. Stewart, *Engineering the properties of spray-dried detergent granules*. PhD thesis, University of Manchester, 2015.

[96] R.J.S.Brown and P, *Diffusion NMR of Confined Systems: Fluid Transport in Porous Solids and Heterogeneous Materials (New Developments in NMR)*. Royal Society of Chemistry, 2016.

[97] P. Kortunov, S. Vasenkov, J. Kärger, R. Valiullin, P. Gottschalk, M. F. Elía, M. Perez, M. Stöcker, B. Drescher, G. McElhiney, C. Berger, R. Gläser, and J. Weitkamp, "The role of mesopores in intracrystalline transport in USY zeolite: PFG NMR diffusion study on various length scales," *Journal of the American Chemical Society*, vol. 127, pp. 13055–13059, Sept. 2005.

[98] J. Griffith, A. Bayly, and M. Johns, "Evolving micro-structures in drying detergent pastes quantified using NMR," *Journal of Colloid and Interface Science*, vol. 315, pp. 223–229, Nov. 2007.

[99] A. N. Semenov and A. A. Shvets, "Theory of colloid depletion stabilization by unattached and adsorbed polymers," *Soft Matter*, vol. 11, no. 45, pp. 8863–8878, 2015.

[100] R. I. Feigin and D. H. Napper, "Depletion stabilization and depletion flocculation," *Journal of Colloid and Interface Science*, vol. 75, pp. 525–541, June 1980.

[101] P. Jenkins and M. Snowden, "Depletion flocculation in colloidal dispersions," *Advances in Colloid and Interface Science*, vol. 68, pp. 57–96, Nov. 1996.

[102] X. L. Chu, A. D. Nikolov, and D. T. Wasan, "Effects of particle size and polydispersity on the depletion and structural forces in colloidal dispersions," *Langmuir*, vol. 12, pp. 5004–5010, Jan. 1996.

[103] V. Vajihinejad, S. P. Gumfekar, B. Bazoubandi, Z. R. Najafabadi, and J. B. P. Soares, "Water soluble polymer flocculants: Synthesis, characterization, and performance assessment," *Macromolecular Materials and Engineering*, vol. 304, p. 1800526, Nov. 2018.

[104] R. J. Correia and J. Kestin, "Viscosity and density of aqueous sodium sulfate and potassium sulfate solutions in the temperature range 20-90 .degree.c and the pressure range 0-30 MPa," *Journal of Chemical & Engineering Data*, vol. 26, pp. 43–47, Jan. 1981.

[105] H. Falkenhagen, "Viscosity of electrolytes," *Nature*, vol. 127, pp. 439–440, Mar. 1931.

[106] D. E. Goldsack and R. Franchetto, "The viscosity of concentrated electrolyte solutions. i. concentration dependence at fixed temperature," *Canadian Journal of Chemistry*, vol. 55, pp. 1062–1072, Mar. 1977.

[107] R. House and J. L. Darragh, "Analysis of synthetic anionic detergent compositions," *Analytical Chemistry*, vol. 26, pp. 1492–1497, Sept. 1954.

[108] R. Pugh, *Bubble and foam chemistry*. Cambridge: Cambridge University Press, 2016.

[109] V. Kumaran and D. L. Koch, "The rate of coalescence in a suspension of high reynolds number, low weber number bubbles," *Physics of Fluids A: Fluid Dynamics*, vol. 5, pp. 1135–1140, May 1993.

[110] R. Maschmeyer and C. T. Hill, "The rheology of concentrated suspensions of fibers," in *Advances in Chemistry*, pp. 95–105, American Chemical Society, June 1974.